AN ABSTRACT OF THE DISSERTATION OF

Changqing Pan for the degree of Doctor of Philosophy in Chemical Engineering presented on April 3, 2017.

Title: Solution-based Chalcogenide Thin Film Deposition

Abstract approved:

_____

Chih-Hung Chang

As a group of promising semiconductor materials, metal chalcogenides in thin film form have been widely used in electronics and optoelectronics applications, such as solar cell devices and photon sensors. Unfortunately, the film size and product throughput are limited by the current vacuum-based thin film deposition techniques. Solution-based thin film deposition could archive a continuous large area thin film deposition of chalcogenides. Also by eliminating the vacuum requirement, the total process cost can be significantly reduced.

Here three different routes to deposit the chalcogenide thin film have been studied: from solution-based deposited metal oxide film, from electroplated metal thin film, and from bulk chalcogenide powder.

By a hydrogen-assisted selenization process, an oxide thin film of copper, indium, and gallium has been successfully transited to $CuIn_{1-x}Ga_xSe_2$ chalcopyrite thin film, and the solar devices have been fabricated based on this p-type chalcogenide material. In a

similar way, a metal stack of copper, zinc, and tin has been converted to Cu_2ZnSnS_4 kesterite thin film solar cell material. The last one, powder molybdenum disulfide is transformed into thin film through a dimensional reduction process with the help of microreactor design and simulation.

This research also includes the fabrication of photovoltaic devices, thin film transistors, and their characterizations in both structural and electronic properties.

There are advantages and disadvantages from each of these solution-based deposition techniques, and by selecting one of these methods, it could archive a generic process route for a large range of metal chalcogenide thin film deposition.

Solution-based Chalcogenide Thin Film Deposition

by
Changqing Pan

A DISSERTATION

submitted to

Oregon State University

in partial fulfillment of
the requirements for the
degree of

Doctor of Philosophy

Presented April 3, 2017
Commencement June 2017

Doctor of Philosophy dissertation of Changqing Pan presented on April 3, 2017

APPROVED:

Major Professor, representing Chemical Engineering

Head of the School of Chemical, Biological, and Environmental Engineering

Dean of the Graduate School

I understand that my dissertation will become part of the permanent collection of Oregon State University libraries. My signature below authorizes release of my dissertation to any reader upon request.

Changqing Pan, Author

ACKNOWLEDGEMENTS

Firstly, I would like to express my sincere gratitude and heartfelt appreciation to my long-term advisor Dr. Chih-Hung Chang for his enormous support and invaluable guidance for the past years. I would also like to extend my appreciation to my Ph.D. research committee members: Dr. Gregory S. Herman, Dr. Alexandre F. T. Yokochi, Dr. Jason H. Ideker, and Dr. Kaichang Li, for their time and commitment to my Ph.D. program. Dr. Herman and Dr. Yokochi have helped me during all the time of research in chemical engineering and material science. Dr. Ideker and Dr. Li provide a lot of guidance in process engineering and thermodynamics study and give me a broader view of the engineering besides chemical engineering.

Thanks to the support from DGIST R&D Programs of the Ministry of Science, ICT & Future Planning of Korea (16-BD-05) and from the National Science Foundation Scalable Nanomanufacturing program under Grant No. CBET-1449383. Thanks to the support from Dr. Jong-Jan Lee, Dr. Wei Pan, Dr. Sean A. Vail, and all colleagues during my internship at Sharp Laboratories of America. Thanks to the facility support from Advanced Technology and Manufacturing Institute. Part of the work was performed at the Oregon Process Innovation Center for Sustainable Solar Cell Manufacturing (OPIC), an OregonBEST signature research facility.

Thanks to every group member in Chang's group: Dr. Hyundae-Dae Jin, Dr. Seung-Yeol Han, Dr. Wei Wang, Dr. Yu-Wei Su, Dr. Katherine Han, Dr. Chang-Ho Choi, Dr. Paravee Vas-Umnuary, Dr. Dick Chiu, Dr. Ki-Joong Kim, Dr. Debra Gilbuena, Yong Jun Li, Wei-Liang Yen, Hsiang-Wei Tsai, Michael Knapp, Guoheng Ma, Zhen Fang,

Michele David, Qun Jing, Yujuan He, Zhongwei Gao, Yujing Zhang, Han Mei, Ziyan Liu, Cheng Zeng, Shujie Li, Yu Cao, Jiayi Du, Hao Sun, and Tianlei Li.

There are two persons I would like to give my special thanks to: Dr. Peter C. Rieke and Dr. Chung Kwai Lui. To me, it was a shock when the first time I met with Dr. Rieke at the parking lot in Pacific Northwest National Laboratory before I know he is the first paraplegic man who conquered Mt. Rainier by hand-cranked snow pod. As my short period supervisor in PNNL, his passion and professionalism always encourage me when facing any difficulty. Dr. C. K. Lui (Mrs. Wei) passed away on January 3, 2008, the same year I arrived at Oregon State University, and I know her through her longtime friends Janet and Edward Chen. Dr. Lui arrived in the States in 1936 as an exchange student, and after overcoming the cultural and finance challenges, she was the first woman to receive a Ph. D. in physic from Oregon State University (then OSC) in 1941. She worked for the "Manhattan Project" and was named "Woman of the Day" by President Roosevelt on May 30, 1949. She is a role model for me who also pursue the degree at Oregon State University 6000 miles away from my hometown.

Last, but not least, I would like to thank my parents, Qimin and Jianhua, my sister Changhong and her family for their longtime supporting. Thanks to my wife Dr. Jie Zhang for her unending support and encouragement.

TABLE OF CONTENTS

TABLE OF CONTENTS (Continued)

Page

TABLE OF CONTENTS (Continued)

Page

TABLE OF CONTENTS (Continued)

Page

TABLE OF CONTENTS (Continued)

Page

TABLE OF CONTENTS (Continued)

Page

LIST OF FIGURES

Figure Page

LIST OF FIGURES (Continued)

Figure Page

LIST OF FIGURES (Continued)

Figure Page

LIST OF FIGURES (Continued)

Figure Page

LIST OF TABLES

Table Page

CHAPTER 1 Introduction

1.1 Chalcogen and chalcogenide

1.1.1 Chalcogen

The chalcogens are the elements in Group 16 (Group VIA in CAS system) of the periodic table. This group consists of the elements oxygen (O), sulfur (S), selenium (Se), tellurium (Te), polonium (Po) and Livermorium (Lv), which are listed in Table 1-1.

Table 1-1 A list of Group 16 elements up to Period 7

Element	**Appearance**	**Abundance in Earth's Crust by Mass (ppm)[1, 2]**	**Electronegativity (Allen Scale)[3]**	**Common Oxidation States**
O	Non-metal, gas, colorless	495,000	3.610	-2, 0
S	Non-metal, solid, yellow	350	2.589	-2, 0, +2, +4, +6
Se	Non-metal, solid, red or metallic grey	~0.05	2.424	-2, 0, +2, +4, +6
Te	Metalloid, solid, silver	~0.005	2.158	-2, 0, +2, +4, +6
Po	Metal, radioactive, trace in nature	2×10^{-10}	-	-
Lv	Synthetic, radioactive, $t_{1/2} \leq 60$ ms	-	-	-

Oxygen is the most abundant element in the earth which constitutes about half of the earth's crust, 89% of the water and 23% of the air by mass. Although oxygen exists as a simple substance in the atmosphere, it was discovered as an element in the later 18th century. Oxygen has a unique chemical property because of its strong electronegativity, and in most

compounds of oxygen, its oxidation state is -2 with the exceptions in peroxides, superoxides, and oxygen fluorides.

Sulfur is within the ten most abundant elements in the earth by both mass and atoms, and it is also ranked 17th in the earth's crust by mass. It is one of the earliest known elements to humans, and since the pale-yellow pure sulfur exists near volcanoes and hot springs, it was connected with fire and known as brimstone in the Old Testament (*Genesis*19:24). As a non-metal, sulfur has a moderate-high electronegativity and forms acidic oxides as SO_2 and SO_3.

Selenium is a byproduct of the refining process of metal sulfide ores and has a similar atomic abundance as silver. The hexagonal crystal of selenium is silver gray and monoclinic crystal is deep red. Although solid selenium is a p-type semiconductor, it is considered as non-metal.

Tellurium was discovered earlier than selenium and named after the Latin word *tellus* for "earth". It is among the rarest elements in the earth and with a comparable abundance as gold and platinum. Considered as a metalloid, tellurium has chemistry properties similar to selenium's, that is the reason Jacob Berzelius named selenium after the Greek word *Σελήνη* (*selene*) for "moon".

Polonium and livermorium are the last two elements in the above list. Polonium was discovered from pitchblende by Marie and Pierre Curie in 1898 and named after Marie Curie's homeland of Poland. Livermorium (formerly Uuh) was synthesized by the collaboration between Joint Institute for Nuclear Research and Lawrence Livermore

National Laboratory in 2000.[4] Since both polonium and livermorium are highly radioactive elements with short half-life time, they are beyond the general scope of material science and engineering.

The electronegativity and common oxidation states make oxygen distinctive from the rest in the same group. In general, the chalcogens are specific to the elements of sulfur (S), selenium (Se), and tellurium (Te). In this dissertation, the narrow definition of chalcogen will be used.

1.1.2 Chalcogenide

When forming a chemical compound with halogens, oxygen, and nitrogen, the chalcogen is assigned a position oxidation state and forms chalcohalide, chalcogen oxide, and chalcogen nitride. SF_6 is a well-known high-density gas used as both gaseous electrical insulator and plasma dry etchant. SO_2 and SO_3 are significant air pollutants and the primary agents in acid rain. Polythiazyl ($(SN)_x$) is the first conductive inorganic polymer discovered.[5]

The chalcogenide is any chemical compound with the anion of S^{2-}, Se^{2-}, Te^{2-}, or the mixed system of these three kinds of anions as the major anion. Obviously, the cation elements in the chalcogenide should be more electropositive than the chalcogen.

All dihydrogen chalcogenides are toxic gases with extreme strong unpleasant smell and can form acidic aqueous solution as hydrochalcogenic acids. There are several non-metal element sulfides such as B_2S_3, CS_2, SiS_2, P_4S_{10}, As_2S_3, and As_4S_4. Most of these sulfides

can be hydrolyzed to H_2S when reacting with water (or CS_2 hydrolase in the case of CS_2, and ethanol in the case of SiS_2).

Due to the high electropositivity of alkali metal, most alkali metal chalcogenides are water-soluble solid salts. The solution of alkali metal chalcogenide is often used for the synthesis of other low solubility chalcogenides. Alkaline earth metal can also form chalcogenide salt with less solubility. As ionic crystals, most of the alkali metal chalcogenides and alkaline earth metal chalcogenides are insulators.

Group 14 metal tin and lead can react with chalcogen and form IV-VI chalcogenide. The oxidation state of metal elements in both tin and lead chalcogenides can be +2 and +4. These chalcogenides can be p-type or n-type semiconducting and used as materials for photoconductor, IR sensor, and thermoelectric device.[6]

The most interesting parts of the metal chalcogenides are transition metal chalcogenides. They can be crystalline or amorphous, and the structures of them can be linear chains, layers, three-dimensional frameworks.[7] Transition metal chalcogenides exhibit a great diversity of physical and chemical properties. In the electronic application, they can be semiconducting or metallic, and the band gap of the semiconductor varies in a large range.

II-VI chalcogenides are chalcogenides of the metal elements from Group 12 (Group IIB in CAS system): zinc (Zn), cadmium (Cd), and mercury (Hg). Most studied II-VI chalcogenides are ZnS, CdS, CdSe, and CdTe which crystallize in either cubic zincblende (Sphalerite) or hexagonal Wurtzite structure.[8] ZnS is a common n-type semiconductor with a wide bandgap of 3.5 eV (cubic) to 3.9 eV (hexagonal) and is widely used in optoelectronic

device applications. CdS with a band gap of 2.4 eV (bulk) to 3.2 eV (thin film) has been used in fabricating photovoltaic devices. CdSe thin film is also used for solar cell due to its band gap of 1.7 eV to 2.3 eV and n-type conductivity. CdTe is one of the most successfully commercialized thin film solar cell materials. Nanoparticles of ZnS, CdS, and CdSe have also been extensively studied as quantum dots for electronic and optoelectronic application.[9]

Copper sulfides (CuS_x) and copper selenides ($CuSe_x$) have several stable phases at room temperature with different stoichiometry where x is between 1 and 2. They are one of the potentially useful narrow band gap p-type semiconductor materials in solar cell, solar control coating, etc.[10, 11]

Known as fool's gold, iron pyrite (FeS_2) is another p-type semiconductor material with a narrow indirect band gap of 0.9 eV. Due to its high absorption coefficient for $h\nu > 1.3$ eV, it has attracted a lot of attention for photovoltaic applications.[12]

The layer-like transition metal dichalcogenides are another group of chalcogenides which have been studied and used for a long time. Their structures consist of a periodic of sandwiched anions (S, Se, or Te) – cations – anions tri-sheet layer. Between two sandwiches, the anions sheets are adhered by van der Waals force. Nb, Ta, Mo, W, Hf are among these transition metals. With a similar structure as graphite, MoS_2 and WS_2 have been used as dry lubricants. Following the discovery of the graphene, the hot spot of application has been transferred to the semiconductor electronics[13, 14]

1.2 Thin film and its fabrication

1.2.1 Thin film

Thin film is a two-dimensional layer of solid material which is significantly different from the bulk material in terms of both surface and interfacial effects. The range of the thickness is from less than one nanometer to several micrometers.

There is no clear dividing line between “thin” and “thick”, but generally the thickness of thin film should be in comparison with the characteristic length scale. For optical thin film, the thickness should be in hundred nanometers range which is comparable to the quarter of the wavelength of light. For magnetic thin film, the thickness should be just a few atomic layers due to the quantum mechanical exchange interaction length. Thus, the application decides if a film can be considered as “thin” or “thick”.

Besides the thickness, surface and interface are also playing an important role in thin film. Hard coating, friction enhancement layer or friction reduction layer are all relied on the very top layer of the thin film. Surface morphology also affects the optical properties and can be applied in anti-reflection coating and wavelength control.[15]

1.2.2 Thin film deposition

The process of applying a thin film onto a substrate surface is called “deposition”. Common thin film deposition methods listed in Table 1-2 can be divided into two categories: physical and chemical techniques.

Table 1.2 Common physical and chemical deposition techniques

Technique	Precursor	Temperature	Remark
Thermal evaporation	Pellets of pure metals, some low m.p. oxides (GeO_2)	100 °C ~ 1300 °C	Materials need have low m.p., high vapor pressure when heated up to 1300 °C
Sputtering	Target made with high purity metals, alloys, oxides, chalogenides, etc.	100 °C ~ 500 °C	High capital expenses, slow rate, easy degradation
Pulsed laser deposition (PLD)	Oxides, nitrides, chalcogenides, etc.	100 °C ~ 1300 °C	Small area deposition, very expensive setup
Molecular beam epitaxy (MBE)	Oxides, chalcogenides, hetrostructures, organic semiconductors	200 °C ~ 500 °C	Very expensive setup, ultra-high vacuum required
Chemical vapor deposition (CVD)	Gas phase high purity chemicals (mostly metal-organics)	100 °C ~ 500 °C	Possibility of contamination at high temperature, poisonous by-products
Atomic layer deposition (ALD)	Gas phase metal organics, metal halides, H_2O	Room temperature ~ 400 °C	Slow rate, substrate surface need to be pre-treated
Electroplating	Metal salt solution	Room temperature	High setup cost, low production cost
Electroless plating	Metal salt solution, reduction agent	Mostly room temperature	Relatively lower setup cost, potential low uniformity
Chemical bath deposition (CBD)	Metal salt solution, anion source	25 °C ~ 90 °C	Low cost, slow rate, low material utilization
Spray pyrolysis	Metal salt or metal organics	200 °C ~ 500 °C	Mostly for oxide film

Low-pressure vapor environment is required for most physical deposition methods using mechanical or thermodynamic method to produce the thin film. Thermal evaporation, e-beam evaporation, sputtering, pulsed laser deposition (PLD), molecular beam epitaxy (MBE), etc., are known examples of physical deposition methods, which can also be classified as physical vapor deposition (PVD).

When the deposition process is primarily chemical, the precursor can be vapor phase or liquid phase. Chemical vapor deposition (CVD), metalorganic chemical vapor deposition (MOCVD), plasma enhanced CVD (PECVD), atomic layer deposition (ALD), etc. mostly based on gas phase precursor. The precursors in electroplating, electroless plating, chemical bath deposition (CBD), spray pyrolysis, etc. are in liquid phase. Chemical process such as sol-gel is also involved in spin coating, dip coating, drop casting, and other liquid to thin film processes.

1.3 Chalcogenide thin film deposition

1.3.1 Chalcogenide thin film via PVD

Thermal evaporation is one of the simplest setups among all PVD techniques and mostly used for low melting point metal film deposition. The advantages of thermal evaporation include good stability, high reproducibility and high deposition rate. The hot source material evaporates, and the vapor flux directly condenses on the substrate. Vacuum at mPa level (10^{-5} mbar level) is required to prevent the contamination of deposition material and protect the heating elements. Since the melting point of most common metal chalcogenide is relatively high, when applying thermal evaporation, the source will directly sublime into vapor phase and deposition to the cooler substrate skipping the melting down step in most

metal deposition process. Wu et al. prepared the ZnS (m.p. > 1800 °C) optical thin film ranging from 310 to 1240 nm by this technique in which the heating element is applied with 130 A current and the quartz substrate is kept at room temperature.[16]

An alternative thermal evaporation technique is close space sublimation which has been widely used for CdTe (m.p. 1041 °C) deposition. The distance between source and substrate is 2 to 5 mm, and temperatures of source and substrate are set to 600 °C and 700 °C respectively. Under these condition, the deposition process is limited as a diffusion process, and a 3~5 μm CdTe thin film can be obtained within 5 minutes.[17]

Sputtering deposition is used extensively in the industry. The material is ejected from a solid target due to the bombardment of the target by plasma or other energetic particles. The ejected atom or ion clusters can ballistically fly from the target and impact energetically onto the substrate on the opposite side of the vacuum chamber. Argon is the most common gas used to generate the plasma while other noble gases are also used depending on the atomic weight of the target. As opposed to thermal evaporation, sputtering is commonly used for high melting point metals and compounds. Shi et al. used a single quaternary chalcogenide target of Cu-In-Ga-Se fabricated the Cu(In, Ga)Se_2 thin film.[18] Shao et al. prepared ZnS thin film as the buffer layer in $CuInS_2$ thin film solar cell via RF reactive sputtering.[19]

PLD and MBE both have very expensive setup require high-power pulsed laser and ultra-high vacuum respectively. They are used for small size sample preparation, and the successful examples include ZnS,[20] CdS,[21] CdSe,[22] Bi_2S_3.[23]

1.3.2 Chalcogenide thin film via CVD

CVD is another thin film deposition technique often used in the semiconductor industry. In a typical CVD, the substrate is exposed to the volatile precursor which react or decompose on the substrate surface to produce the desired thin film. The gas phase by-product is removed by gas flow from the reaction chamber.

Atmospheric pressure CVD (AP-CVD) is processed at atmospheric pressure. Berry et al. prepared FeS_2 thin films on both glass and molybdenum-coated glass substrates by AP-CVD. Iron (III) acetylacetonate and t-butyl disulfide were used as precursors reacting at 300 °C, followed by sulfur annealing at 500 ~ 550 °C to finally convert marcasite impurities to pyrite.[24]

Metalorganic CVD (MOCVD) takes place at low pressures and involves the organometallic precursors for cation source. The chalcogen anion source is usually hydrogen chalcogenide. Yamaga et al. prepared the ZnS thin film on GaAs substrate by using dimethyl zinc (DMZn) and H_2S as ZnS precursors, and trimethyl aluminum (TMAl) and HCl as dopant sources. The reactor pressure was maintained at 1 Torr, and substrate temperature was varied between 250 and 350 °C.[25]

1.3.3 Chalcogenide thin film via electrodeposition

Electrodeposition is a process that use electric current to reduce dissolved metal cations and other ions so they can form a coherent coating on a conductive cathode substrate. It has been used in industry to fabricate metal thin film coating for centuries. Metal source is common solvable salt, and chalcogen source can be $Na_2S_2O_3$ for S, SeO_2 for Se, and TeO_2

for Te. The as-deposited film mostly needs a post annealing process to eventually convert the metal and chalcogen into metal chalcogenide.

For Cu_2ZnSnS_4 thin film deposition, Pawar et al. reported a single-step co-electrodeposition of the metals, as well as the sulfur. The room temperature electrolytic bath contains $CuSO_4$, $ZnSO_4$, $SnSO_4$, and $Na_2S_2O_3$. After 1 hr 550 °C post annealing, the films were converted into Cu_2ZnSnS_4 thin film with band gap of 1.5 eV.[26]

1.3.4 Chemical bath deposition

Chemical bath deposition (CBD) is a simple, inexpensive solution-based thin film deposition technique. It operates at a moderate temperature and can be scale-up for large area deposition. The CBD is based on the formation of a solid phase from a solution.

As early as 1835, aldehydes reduce silver salts to metallic silver film in chemical bath was reported by Liebig.[27] In 1884, the preparation of PbS by CBD was reported by Emerson-Reynolds who used lead(II) tartrate ($C_4H_4O_6Pb$) and thiourea ($CS(NH_2)_2$) as precursors and 38~50 °C as reaction temperature.[28] Nowadays, the process for metallic film deposition is classified as electroless deposition, while CBD is more specifically to the oxides and chalcogenides deposition.

There are four main deposition mechanisms for the thin film formation in CBD process:[29]

1) *The simple ion-by-ion mechanism*:

$$mM^{n+} + nX^{m-} \rightarrow M_mX_n$$

When the ionic product $[M^{n+}]\cdot[X^{m-}]$ is larger than the solubility product of M_mX_n, the solid phase of M_mX_n forms.

2) *The simple cluster (hydroxide) mechanism*:

$$M^{n+} + nOH^- \rightarrow M(OH)_n$$

$$mM(OH)_n + nX^{m-} \rightarrow M_mX_n + nOH^-$$

The formation of M_mX_n has a metal hydroxide intermediate which can be either a colloid or an absorbed species on the substrate.

3) *The complex decomposition ion-by-ion mechanism* (CdS is used as a typical example for 3) & 4) mechanism):

$$Cd^{2+} + CS(NH_2)_2 \rightleftharpoons \quad \text{-C}(NH_2)_2\big]^{2+}$$

$$\big[Cd\text{-}S\text{-}C(NH_2)_2\big]^{2+} + 2OH^- \rightarrow CdS + CN_2H_2 + 2H_2O$$

Here the CdS chalcogenide formation relies on the breakage of the carbon-chalcogen bond of the complex.

4) *The complex decomposition cluster mechanism*:

$$nCd^{2+} + 2nOH^- \rightleftharpoons \quad \text{H})_2\big]_n$$

$$\big[Cd(OH)_2\big]_n + CS(NH_2)_2 \rightleftharpoons \quad \text{H})_2\big]_{n-1}(OH)_2\,Cd\text{-}S\text{-}C(NH_2)_2$$

$$\big[Cd(OH)_2\big]_{n-1}(OH)_2\,Cd\text{-}S\text{-}C(NH_2)_2 \rightarrow \big[Cd(OH)_2\big]_{n-1} CdS + CN_2H_2 + 2H_2O$$

The hydroxide adsorbed on the substrate involves the decomposition of thiourea, and provide the cation source for the final thin film.

1.3.5 Chalcogenide thin film via CBD

CBD is a simple and low-cost technique for CdS thin film deposition. Su et al. prepared the CdS thin film via a continuous microreactor-assisted solution deposition.[30] With the same precursors as in the conventional CBD, the continuous flow system achieves a high-quality nanocrystalline CdS thin film on fluorine-doped tin oxide (FTO) coated glass at a high deposition rate of 25.2 nm/min.

Vas-Umnuay reported the Cu_xS thin film deposition by photochemical deposition (PCD).[31] Instead of the thiourea in most Cu_xS CBD process, Na_2SO_3 is used as the chalcogen source, and the release of sulfur is photo-activated by the UV illumination to the substrate. This technique can control the deposition by turning on and off the UV light and generate specifically patterned thin film with a photo mask.

Chiu studied the growth kinetics of ZnS thin films in both conventional CBD and micro-reactor assisted solution deposition (MASD).[32] To demonstrate the utility of the ZnS thin film, both SnS and CuS thin films were deposited on top of the ZnS thin film to form a triple layered precursor film for $Cu_2ZnSn(S,Se)_4$ thin film solar cell fabrication.

1.4 Generic solution-based chalcogenide deposition

Although CBD is a simple and low-cost chalcogenide thin film deposition technique, it is limited by the solubility product of final chalcogenide material. CBD is also sensitive to the deposition conditions, to obtain a relative stable deposition rate, a well-controlled bath environment is necessary. The conditions include the temperature of the solution bath, chemical nature of the substrate, substrate surface topography, etc.

In this dissertation, another three solution-based deposition routes are investigated in the following chapters, and the author would like to explore several generic deposition techniques besides CBD for the large group of metal chalcogenide thin films.

CHAPTER 2 From Oxide to Chalcogenide:

Solution-based Chalcopyrite Thin Film Deposition

2.1 Solution-based oxide thin film deposition

2.1.1 Development of solution-based oxide thin film deposition

The solution-based sol-gel processing has been used to prepare solid oxide layer when Ebelmen discovered the silicon alkoxides (sol) slowly hydrolysis in air with humidity to yield silica gel (gel) in the mid of the nineteenth century.[33] After 100 years research, besides SiO_2, more metal oxide thin films chemical solution depositions (CSD) have been developed, such as Al_2O_3, TiO_2, etc., most are Group 3-8 metal oxides.[34]

With the study on the sol-gel process of lead zirconate titanate (PZT) thin film, the solution-based process becomes capable of handling complex electronic oxide thin film deposition.[35] Nowadays, the CSD technique has been successfully applied to deposit the thin film of lots functional oxides, including semiconductor oxide materials for transistor,[36] transparent conducting oxides for displayer,[37] ion-conducting oxides for solid fuel cell,[38] etc.

2.1.2 Alkoxide based precursor system

Metal alkoxides are the most common precursors in chemical solution deposition. The metal alkoxide is synthesized from metal chloride and anhydrous alcohol, HCl is the by-product and can be removed by adding ammonia followed by filtration. Usually the metal alkoxide is more expensive than metal nitrates, oxides, carbonates or carboxylates.

The gel formation mechanism of CSD with metal alkoxide precursor can be hydrolysis and condensation, thus the reaction is highly sensitive to the moisture:

$$\mathrm{M(OR)}_n + \frac{n}{2}\mathrm{H_2O} \rightarrow \mathrm{MO}_{n/2} + n\mathrm{ROH}$$

$$\text{-M-OR} + \text{RO-M} \rightarrow \text{-M-O-M} + \mathrm{ROR}$$

2.1.3 Carboxylate based precursor system

Metal carboxylates are the second most frequently used precursors in CSD for oxide thin film. They are synthesized from metal hydroxides and carboxylic acid. The price of metal carboxylate precursor is usually lower than metal alkoxide.

In the metal alkoxide system, the by-product is alcohol and can be simply removed by evaporation. While in the metal carboxylate system, the organic part needs to be removed by thermal decomposition. The study on metal acetate thermal decomposition shows there are three stages of the decomposition: 1) dehydration happened at around 100 °C, 2) intermediates formation largely between 100 and 200 °C, 3) converting of the intermediates to final product at 350 to 450 °C.[39]

For carboxylate system, the advantage over alkoxide system is it is lower sensitive to water and moisture. A disadvantage is the decomposition process at around 400 °C will reduce the film density and introduce micro-cracks in the film. The process is also called metallo-organic decomposition (MOD). In many cases the processing routes are based on a hybrid of sol-gel chemistry and MOD-chemistry, so here they are collectively called as “sol-gel” process.

2.2 Selenization of oxide thin film

2.2.1 Displacement reaction

The electronegativity and polarizability value of oxygen are significantly different from the values of chalcogens, which leads to the differences in crystal structure and electronic properties of oxides and chalcogenides with same metal cations. On the other hand, chalcogens are in the same group as oxygen and share the same -2 oxidation state in most metal chalcogenides as oxygen in the metal oxides. It provides the possibility of substituting the oxygen with chalcogen and forming metal chalcogenide thin film from the metal oxide.

The simple displacement reaction can be represented as $A + B\text{-}C \rightarrow A\text{-}C + B$, where A is more reactive than B, which will form a more stable product A-C than B-C. In the case of using chalcogen to substitute oxygen, the bonding between metal and chalcogen is often weaker than in oxide which prevents the reaction going through at room temperature.

For the reaction of $S + CuO \rightarrow CuS + \frac{1}{2}O_2$, the thermodynamics calculation results in Table 2-1 show the reaction is thermodynamics favorable until the temperature is higher than 1090 K (817 °C).

Table 2-1 Gibbs free energy in the simple replacement reaction of copper oxides to sulfide

T / K	**273**	**298**	**400**	**500**	**600**	**1090.32**
$\Delta_r G_T^0 / \mathrm{kJ \cdot mol^{-1}}$	77.18	74.82	65.19	55.74	46.30	0.00

To solve this challenge, Kapur et al. proposed an alternative route: First, the metal oxides are reduced into elemental metal or metal alloy film using a gas mixture of H_2 and N_2 at temperature between 500 and 550 °C, then the metal film is sulfurized or selenized using a gas mixture of H_2Se and N_2 gases between 420 and 450 °C to form the final chalcogenides.[40] It can be represented by CuO in the following reactions:

$$\left.\begin{array}{l} CuO + H_2 \rightarrow Cu + H_2O \\ Cu + H_2S \rightarrow CuS + H_2 \end{array}\right\} \rightarrow CuO + H_2S \rightarrow CuS + H_2O$$

The Gibbs free energy of this route is always negative when T > 0 K.

2.2.2 Hydrogen assisted replacement reaction

There are two parts can be improved in the previous process: 1) As it is mentioned in Chapter 1, dihydrogen chalcogenides are all extreme toxic gases. The maintenance of the H_2S or H_2Se cylinder need to be addressed, 2) The thermodynamics calculation shows the second step of the reaction only need S, H_2S is not necessary. So here is the new approaching:

$$CuO + H_2 + S \rightarrow CuS + H_2O$$

It is a one-pot reaction involving both gas mixture of H_2 and N_2 gases and solid sulfur powder. Regarding the mechanism, it can be considered as an in-situ generated H_2S gas reacting with metal chalcogenides. The thermodynamic data in Table 2-2 favors this reaction at any temperature.

Table 2-2 Gibbs free energy in the hydrogen assisted replacement reaction of copper oxides to sulfide

T/K	273	298	400	500	600	(2779.25)
$\Delta_r G_T^0 / \mathrm{kJ \cdot mol^{-1}}$	-152.48	-153.73	-158.82	-163.82	-168.81	0.00

By using in-situ generated H_2S, this process eliminates the requirement of the H_2S gas cylinder. Furthermore, the sample is only loaded into the furnace for one time which reduces the operation cost.

2.2.3 The study of CuO to CuSe transition

A CuO to CuSe transition process is studied to verify the feasibility of this proposed route:

1) Carboxylate based sol-gel deposition: 1 mmol copper(II) acetate ($CuAc \cdot H_2O$, Aldrich, 99.99%) in ethanol solution was used in the carboxylate sol-gel process to form the CuO amorphous thin film on molybdenum-coated glass substrate by spin coating. The wet film was first dried at 100 °C on hot plate to obtain the gel film; then the gel film was pyrolyzed at 400 °C in a box furnace for 5 minutes to form the "amorphous" oxide film. In order to obtain a higher thickness, the spin coating−drying−pyrolysis cycle was repeated for 6 times.

The thermal decomposition of $CuAc_2 \cdot H_2O$ was studied by thermal gravimetric analysis (TGA). The TGA result in Figure 2-1 shows three stages during the temperature ramping: I) *The dehydration of $CuAc_2 \cdot H_2O$*. The sample lost 9% mass corresponding to the water of crystallization in $CuAc_2 \cdot H_2O$. II) *The decomposition of $CuAc_2$*. The mass loss reaches the maximum value 63.14% at 267 °C, and all the carbon has been oxidized leaving copper

oxide as CuO with a small amount of Cu_2O. III) *The small amount of Cu_2O in the copper oxide is finally converted into CuO*. The mass loss stops at 60%, corresponding to the mass ratio of CuO : $CuAc_2 \cdot H_2O$.

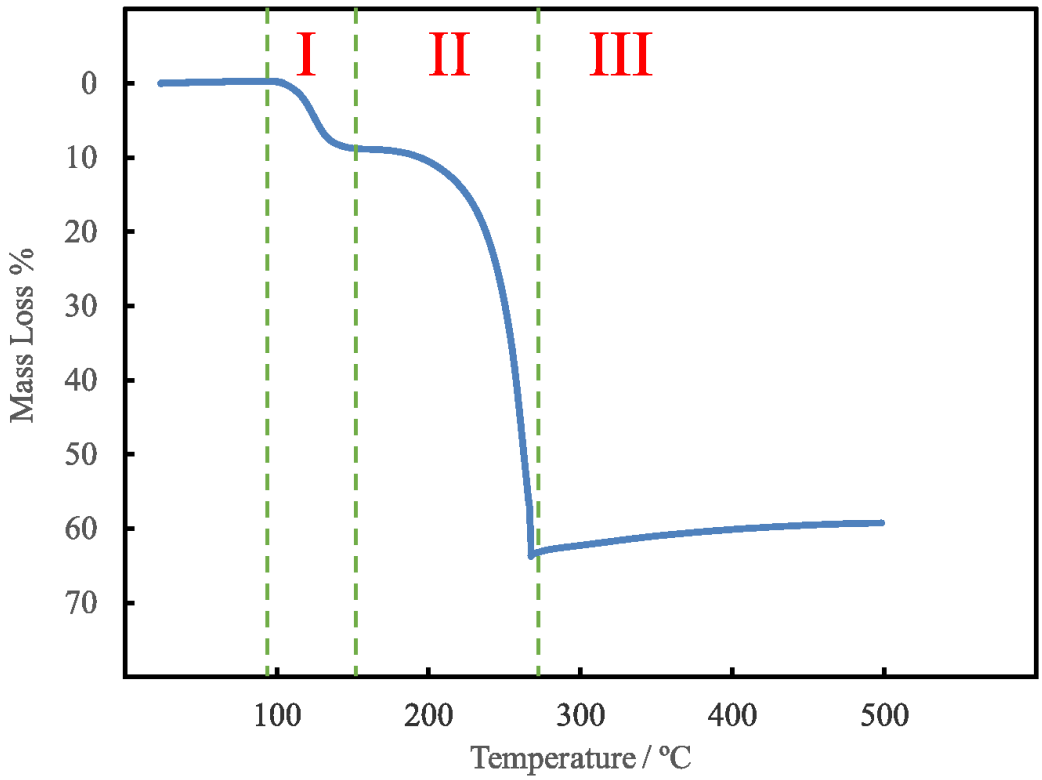

Figure 2-1 TGA result of $CuAc_2 \cdot H_2O$ heated in air from room temperature up to 600 °C

Scanning electron microscope (SEM) was used to check the morphology of sol-gel copper oxide thin film on Mo-coated glass substrate. The images in Figure 2-2 show the CuO forms nanoparticle in an amorphous matrix after 400 °C. Also micro-cracks can be observed in the top view images.

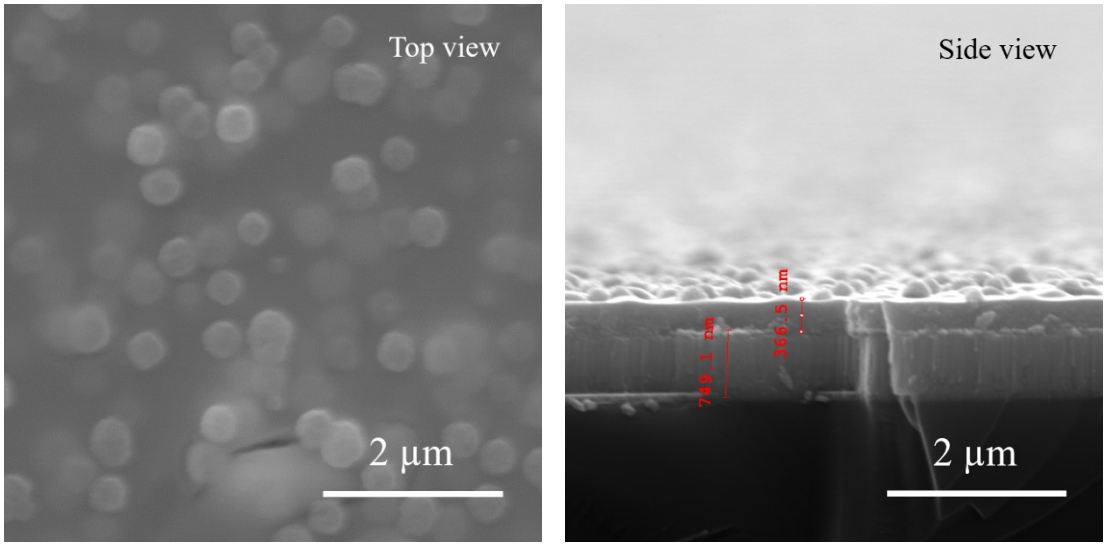

Figure 2-2 SEM images of the metal oxide film by sol-gel process

2) Hydrogen assisted chalcogen replacement: The setup of selenization is shown in Figure 2-3. The oxide film was facing down to a crucible with 0.3 g selenium powder and loaded into a tube furnace. The quartz tube was purged with pure N_2 before heating with 20 sccm 20% H_2 in N_2 forming gas. A scrubber with NaOH solution was used to absorb any H_2Se gas from the furnace.

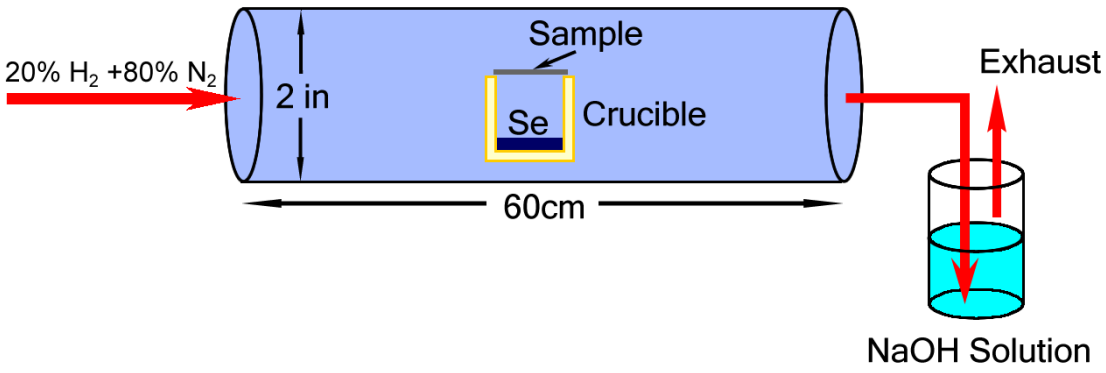

Figure 2-3 Schematic of selenization furnace setup

In order to prevent the delamination, the selenization temperature must be lower than the strain point of the glass substrate. In this study, Corning 1737 LCD glass was used, which has a strain point at 666 °C. There are five chemicals involved in the reaction $CuO + H_2 + Se \rightarrow CuSe + H_2O$. CuO is in solid state with a low vapor pressure in a moderate annealing temperature since its melting point is 1326 °C. Between 100 °C and 666 °C, both H_2 and H_2O are in gas phase. Se has a melting point of 220.8 °C, and CuSe decomposed at 550 °C. Three selenization temperatures were chosen to check the transition from oxide to selenide: 200 °C which is below the m.p. of Se; 230 °C which is just above the m.p. of Se; 530 °C which is just below the decomposition temperature of CuSe. The quartz tube was heated to and held at 200 °C, 230 °C, and 530 °C for 10 mins respectively with a ramping rate of 20 °C/min.

Figure 2-4 shows the SEM images of the thin films processed at different temperatures. At 200 °C, the morphology of the thin film is similar to the original oxide film shown in Figure 2.2. Since the reaction temperature is lower than the melting point of Se (221 °C), the low Se vapor pressure leads to a low H_2Se generation. Although the thermodynamics is favorable, the reaction is too slow to observe within 30 mins. At 230 °C, gigantic CuSe hexagonal plate crystals stick out from the surface of the thin film, which is due to a vapor-solid recrystallization of CuSe on the surface. When the temperature approaches 550 °C, the CuSe crystals soften and cover back to the substrate.

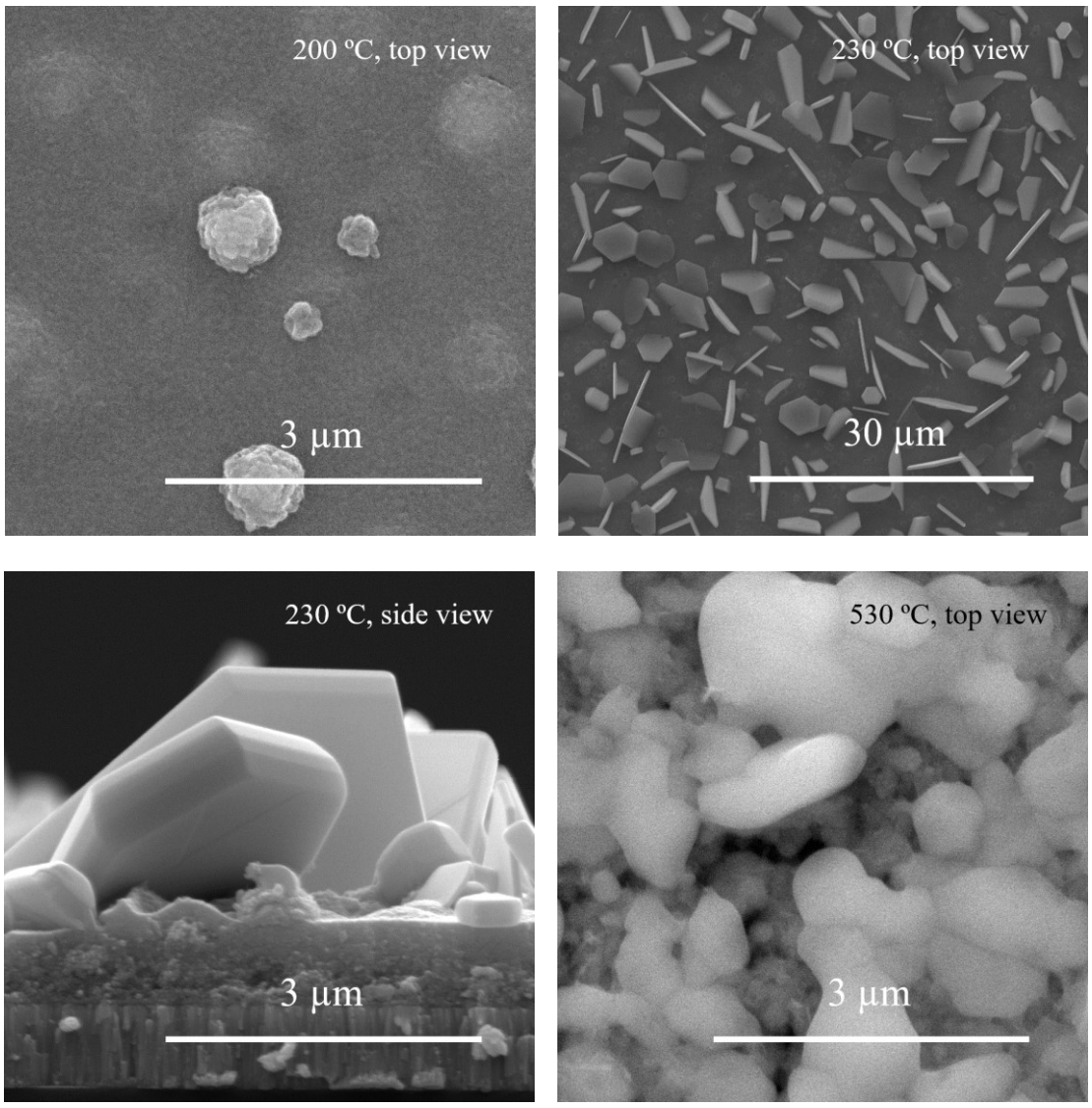

Figure 2-4 SEM images of the selenized thin film at different temperature

This study proved the feasibility of the chalcogenide formation from carboxylate metal salt. By carefully adjusting the annealing temperature and other condition, a chalcogenide thin film with different desired morphology can be obtained.

2.3 $CuIn_{1-x}Ga_xSe_2$ chalcopyrite thin film solar cell

2.3.1 Solar cell

Solar cells, or photovoltaic (PV) devices, are electrical devices that convert the energy of sunlight directly into electricity. The history of the solar cell can be traced back to 19th century when 19-year-old Edmond Becquerel created the world's first photovoltaic cell with silver chloride in acidic solution in 1839. The solar cell technologies have been slowly developing until the groundswell of public interest in seeking a more sustainable long-term energy solution other than fossil fuels due to the oil crisis in the 1970s. Ever since then, the solar cells research and development gets a significant boost and have been playing an important role in the current renewable energy system. Since 2014, the worldwide photovoltaic capacity has been sufficient to over 1% of the world's total electricity consumption.

The operation of a solar cell requires three attributes: 1) Photogeneration; 2) Charge separation; 3) Extraction of carriers to an external circuit. The core structure of a solid-state solar cell is a pn-diode or a Schottky diode, in which a semiconductor forms a rectifying junction either with another semiconductor or with a metal.

Crystalline silicon (c-Si) based solar cell dominates the PV devices marketing at 80% due to its maturity of the technology, and low direct production costs. The non-concentrated solar cell based on c-Si cell has reached the 26.3% efficiency in 2016.[41] The main disadvantage of silicon solar cell is the pollution associated with the solar-grade silicon production especially during both the carbothermic reduction of quartz sand and the chemical purification of metallurgical-grade silicon. In pure theoretical view, c-Si is also

not an ideal material for solar cell: 1) The band gap of c-Si at 1.12 eV is lower than the ideal band gap between 1.4 and 1.6 eV for the maximum single junction device efficiency.[42] 2) As an indirect band gap semiconductor, high temperature reduces its performance. 3) The low absorption coefficient leads to a low material utilization. It needs 100 μm of c-Si to absorb an equivalent light that absorbed by 1 μm of GaAs (a direct band gap semiconductor).

2.3.2 CIGS Thin film solar cell

Thin film solar is a second-generation solar cell which is made by depositing one or more layer thin film on glass, plastic, or metal substrate. It has been developed to overcome the disadvantages of c-Si solar cell by applied optimized band gap and high absorption coefficient semiconductor materials.

Three mainstream thin film solar cell technologies are cadmium telluride (CdTe), copper indium gallium diselenide (CIGS), and amorphous silicon (a-Si). According to the March 2017 version of solar cell efficiency chart from National Renewable Energy Laboratory (NREL) (https://www.nrel.gov/pv/assets/images/efficiency-chart.png), the current champion efficiencies of CdTe, CIGS, and a-Si are 22.1% (by First Solar Inc.), 22.6% (by ZSW), and 14.0% (by AIST) respectively. The efficiency of a-Si solar cell is still not at the same level as c-Si and other thin film solar cell technologies. CdTe accounts for more than half of the thin film market, but the toxicity of cadmium prevents its application on the household rooftop. Among these three technologies, CIGS has the highest efficiency and is more suitable for household installation to substitute the c-Si solar cells.

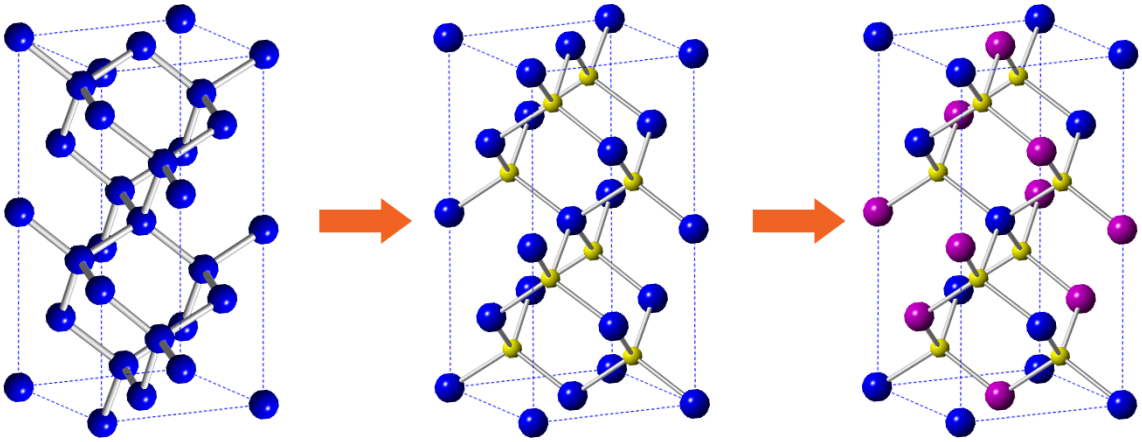

Figure 2-5 The crystal structure evolution from diamond (left), zincblende (middle) to chalcopyrite (right)

CIGS is derived from copper indium diselenide ($CuInS_2$, CIS). The I-III-VI_2 semiconductor CIS has a tetragonal chalcopyrite structure as in Figure 2-5 which is similar to cubic zincblende structure of II-VI materials like ZnS. The crystal structure evolution can be considered as diamond to zincblende to chalcopyrite. From the single crystal silicon has a fcc diamond structure, if half of the Si (oxidation state: 0) is substituted with Zn (+2), and the rest half with S (−2), the crystal structure becomes zincblende. If half of the Zn (+2) is substituted with Cu (+1), and reset with In or Ga (+3), the crystal structure becomes chalcopyrite. Since the direct band gap of CIS is 1.0 eV which is at a low position in the theroatical band gap to efficiency curve for solar cell material, other Group 13 elements have been used as dopants to reduce the lattice size of CIS as well as increase the band gap. Gallium is introduced into CIS to form a solid solution of copper gallium diselenide in CIS, and the band gap of CIGS is between 1.04 eV of CIS and 1.67 eV of copper gallium diselenide. The band gap value is 1.18 eV when Ga/(Ga+In) ratio x (x in $CuIn_{1-x}Ga_xSe_2$) is 0.3.[43, 44]

2.4 CIGS thin film deposition

2.4.1 CIGS thin film deposition via PVD

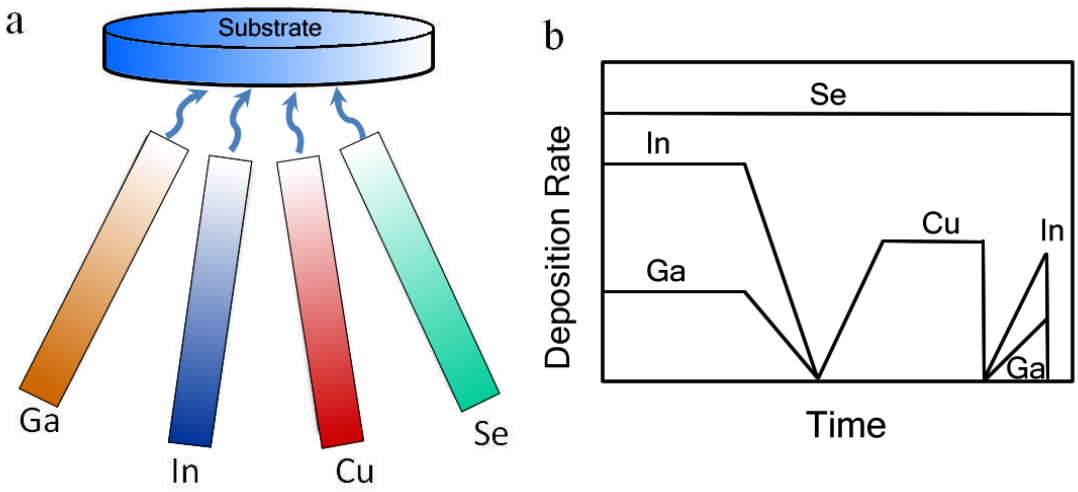

Figure 2-6 Schematic of a multi-stage co-evaporation system with elemental deposition rate

In the CIGS photovoltaic device efficiency competition, thermal co-evaporation from element sources is always the forerunner. In 1980, Boeing introduced a two-stage co-evaporation method to fabricate CIS thin film solar cell with 5.7% efficiency.[45] After that, several multi-stage co-evaporation methods have been used in CIGS thin film deposition, including the current champion cell made by Zentrum für Sonnenenergie- und Wasserstoff-Forschung Baden-Württemberg (ZSW).[46] Figure 2-6 shows an example of one multi-stage co-evaporation method.

Sputtering has also been used in CIGS thin film deposition. Li et al. reported a 9.4% CIGS PV devices made from sequentially sputtering the metals followed by a post-deposition selenization step.[47] The metallic precursors were deposited sequentially using Cu-Ga alloy and In targets by DC magnetic sputtering system. The precursors were then selenized with

solid Se pellets in a closed vacuum furnace. Frantz et al. deposited the CIGS film by RF magnetron sputtering from a single quaternary target without any additional selenization which yielded an 8.9% PV efficiency.[48]

MBE has also been used to deposit high-quality CIGS, but the product size limits this method only in research scale. Stanbery et al. employed migration-enhanced epitaxy (MEE) to grow epitaxial CIS film on (001) GaAs substrate.[49]

2.4.2 CIGS thin film via non-vacuum process

Nanoparticle-based technologies are popular in CIGS thin film non-vacuum deposition, together with the established selenization and/or annealing method; these technologies show the possibility for low-cost PV without expensive vacuum deposition systems. The precursors nanoparticles can be metals (Cu, In, Ga),[50] metal oxides (CuO, In_2O_3, Ga_2O_3),[40] binary chalcogenides (CuS, In_2S_3, Ga_2S_3),[51] ternary/quaternary nanoparticles (CIS, CIGS),[52] and hybrid ink from different category nanoparticles.[53] The nanoparticles in the precursors themselves can be synthesized through hot injection,[52] solvothermal,[54] or even physical machining from bulk materials.[50] One of the disadvantage is the organic ligands used during the nanoparticles synthesis need to be removed otherwise it will introduce a carbon layer which reduces the PV performance.[55]

Electrodeposition can obtain a large area thin film and is easy to scale up to industry production level. Layer-by-layer metals and selenium,[56] and single bath[57] methods have been used in electrodeposition of CIGS thin film.

Mitzi et al. used hydrazine as a solvent to dissolve Cu_2S, In_2Se_3, Ga+Se, and Se/S into a solution, which can be easily converted into pure CIGS film.[58] This dimensional reduction technique will be discussed in Chapter 4.

2.4.3 Oxide to chalcogenide route for CIGS thin film deposition

With the successful experience of the CuO to CuSe transition, CIGS could also be obtained from a sol-gel process oxides thin film. The thermodynamics data proves the paths for both In and Ga to selenides transition with the assistance of hydrogen are feasible. And the critical study is finding the suitable selenization condition to fully convert the amorphous oxides into CIGS quaternary chalcopyrite polycrystalline thin film.

1) Carboxylate sol-gel process: A propylene glycol ink containing 1 mmol $CuAc_2$ (Aldrich, 99.99%), 0.7 mmol indium acetate ($InAc_3$) (Aldrich, 99.99%), and 0.3 mmol gallium acetylacetonate ($Ga(acac)_3$) (Aldrich, 99.99%) was used for spin coating deposition at 1500 rpm. The as-deposited wet film was dried at 175 ºC for 1 min on the hot plate to form the gel film. The gel film was pyrolyzed in a box furnace at 400 ºC for 3 min to obtain the amorphous oxides film. The sol-gel process was repeated for 6 times to finally achieve a 600 nm oxide thin film on Mo-coated glass substrate.

2) Selenization process: The selenization setup in Figure 2-3 was used to selenize the oxide film at 530 ºC for 30 min with a ramping rate of 20 ºC/min. After the selenization, the tube was naturally cooling down and purged with N_2 at 0.1 Lpm overnight to remove the H_2Se gas residue inside the tube.

2.4.4 Characterization of CIGS thin film

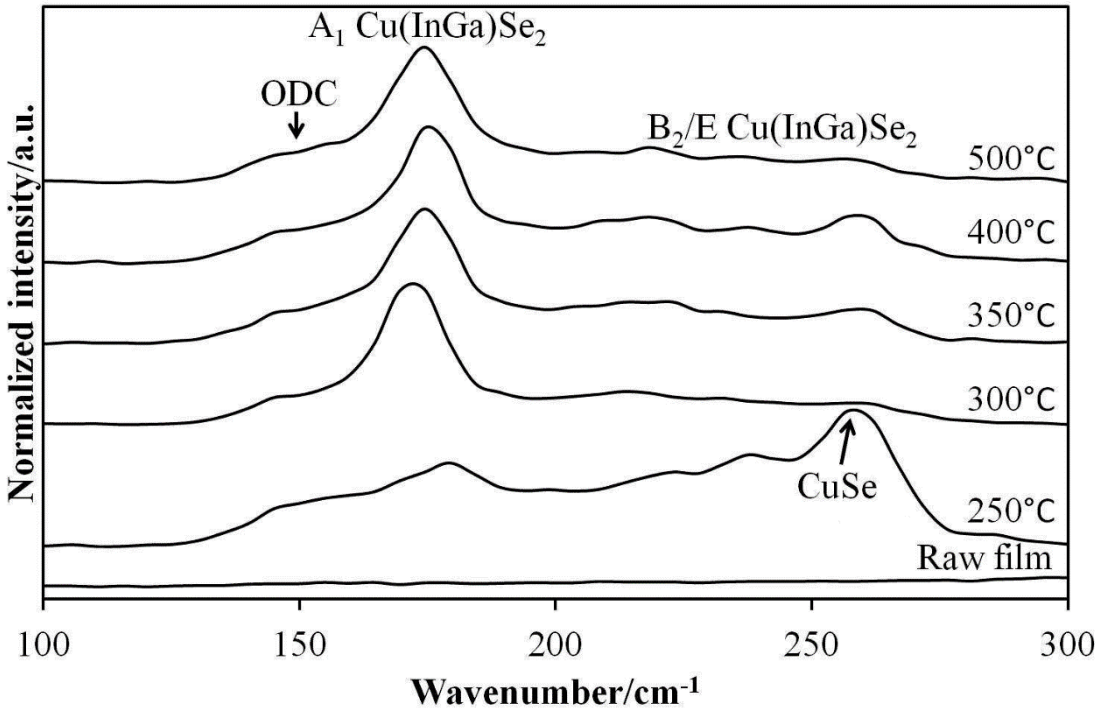

Figure 2-7 Raman spectra of CIGS sample under different selenization temperatures

Raman spectroscopy was used to verify the CIGS formation and identify the secondary phases in the thin film under different selenization temperatures. From Figure 2-7 it can be observed that the CIGS absorption shows up above 300 ºC and CuSe absorption disappears at 500 ºC.

X-ray diffraction (XRD) was used to identify the crystalline components in the film. Figure 2-8 shows the final product has a shift from the reference CIS data which is due to the smaller lattice size of CIGS.

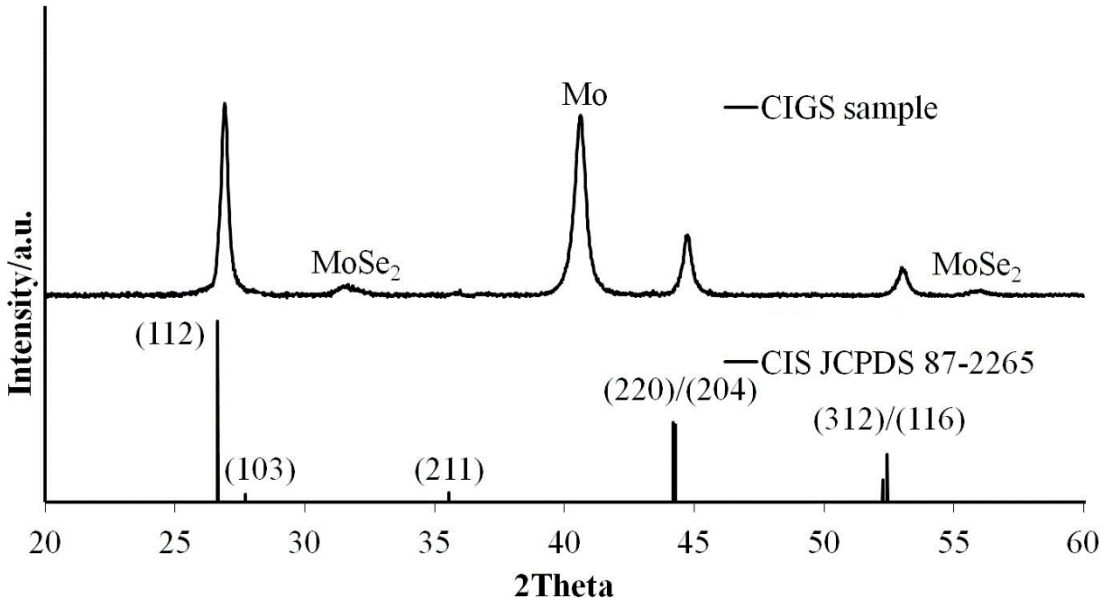

Figure 2-8 X-ray diffraction of CIGS sample

SEM was used to check the film coverage and grain growth of CIGS thin film. Figure 2-9 shows a large grain size and well covered CIGS film from 6-layer spin coated sample selenized at 530 ºC for 30 min.

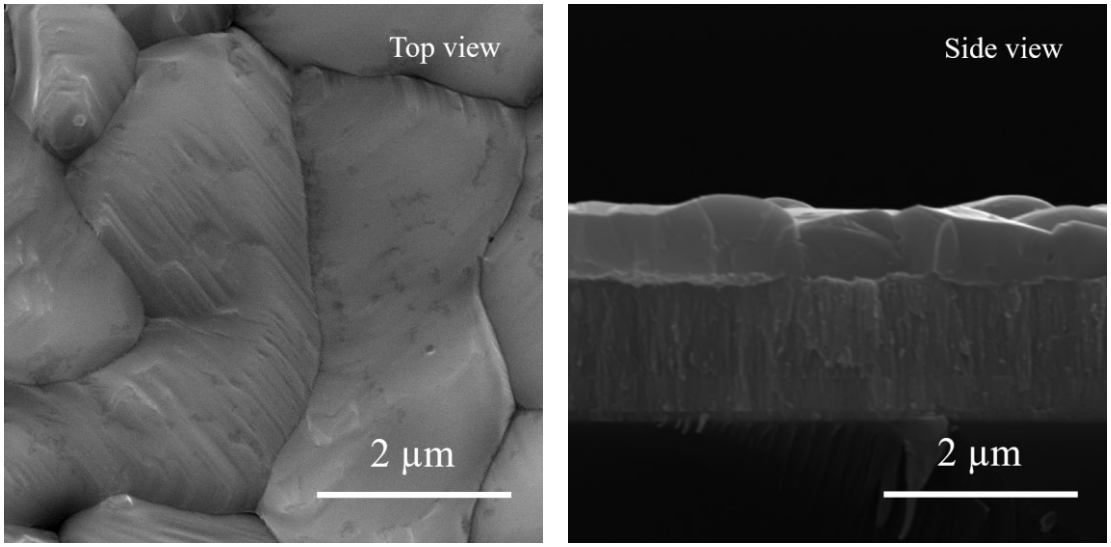

Figure 2-9 SEM images of the CIGS thin film

Electron probe microanalysis (EPMA) was used to quantitatively identify the elemental composition in CIGS. The EPMA result is shown in Table 2-3:

Table 2-3 Electron probe microanalysis result of CIGS thin film

Atomic%	Se	Ga	Cu	In	Mo	Si	Total
#1	55.40	6.68	20.40	16.91	0.00	0.62	100.01
#2	55.19	6.51	20.66	17.17	0.05	0.42	100.00
#3	55.19	6.50	20.69	17.11	0.08	0.43	100.00
#4	48.04	5.83	17.81	14.69	0.00	13.63	100.00
Average	53.46	6.38	19.89	16.47	0.03	3.78	100.00

The calculated Cu/(In+Ga) is 0.87, which is significantly lower than the 1:1 ratio in the precursors. During the selenization, when the CuSe forming, it has a relatively high vapor pressure near the sample surface which accounts the loss of Cu in the final product. The calculated Ga/(Ga+In) is 0.28, close to the expected Ga:In ratio at 0.3:0.7.

2.5 Fabrication of the CIGS thin film solar cell

2.5.1 CIGS thin film solar cell structure

The structures of typical thin film solar cells are shown in Figure 2-10. Substrate structure is more common in CIGS thin film solar cell, thus is called conventional structure, while superstrate structure is called inverted design.

Unlike the rest part of this study, to make a thin film photovoltaic device from scratch is more like a know-how study experience instead of explicit knowledge. The whole process

comes from the accumulation of trial and error. Although the process used here could be further improved, it can do its job and deliver the working PV devices.

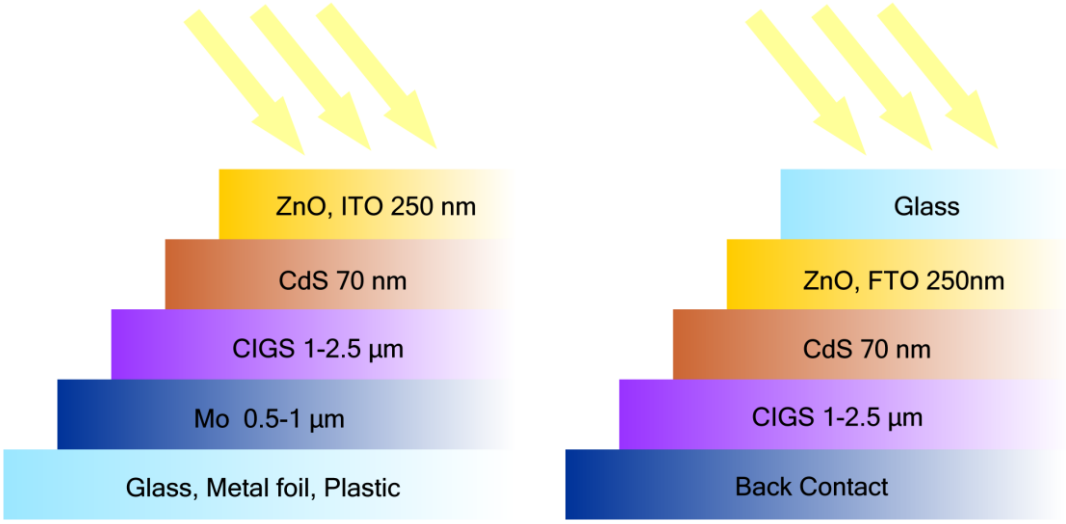

Figure 2-10 Schematic of the substrate structure (left) and superstrate structure (right) for CIGS thin film solar cell substrate

2.5.2 Molybdenum back contact deposition

A low-resistance and stable ohmic contact to CIGS p-type semiconductor material layer is critical for the solar cell performance. Choosing molybdenum (Mo) metal as the back contact is based on two main reasons: lower cost and lower diffusion into CIGS layer at the selenization processing temperature compared to other high work function metals, e.g. gold, platinum. Based on the research at NREL, high argon pressure sputtering deposition will yield a Mo layer adhering well to the glass but with high resistivity, while low argon pressure deposition will yield a Mo layer with low resistivity but poor adhesion to the glass.[59] A bi-layered Mo with different sputtering pressure can take the both advantages of these conditions.

Low thermal expansion and alkali-free borosilicate glass (Corning 1737 and EAGLE^{2000}) was chosen as the base substrate to obtain a crack-free absorber layer after selenization. Mo back contact was deposited on the glass by sputtering in a magnetron "sputter down" system with a base pressure of 2×10^{-5} mTorr. The Mo target (3" diameter, ¼" thickness, and 99.95% purity) was purchased from Kurt J. Lesker. The power on target was set to 40% of 1000 W DC. The flow rate of argon was 20 sccm for 20min and decreased to 5sccm for another 20 min. The corresponding pressures in the chamber were 6 mTorr and 1 mTorr respectively. The final sheet resistance of the bi-layer Mo was measured as 7 Ω/□.

2.5.3 Absorber layer deposition

The Mo-coated substrate was used to deposit CIGS thin film following the previously investigated procedure in Section 2.4.3. Each sol-gel coating layer contributed about 150 nm final CIGS thickness. Up to 11-layer coating had been attempted, but due to the propagation of cracks in the film, the coating was limited to 6 layers to obtain a crack-free final product with a thickness of 800~900 nm.

2.5.4 CdS buffer layer deposition

70 nm n-type CdS buffer layer is a prerequisite for the CIGS solar cell for its participating the heterojunction formation and protecting the p-type layer from the impact of ZnO layer deposition. Due to the toxicity of Cd, ZnS and other materials have been proposed to be used as a substitute for CdS.[60, 61] Here the CBD CdS was still used because of its high reproducibility and reliability.

Figure 2-11 shows the schematic of CBD CdS setup. 0.0288 g $CdSO_4\cdot8/3H_2O$ (Alfa Aesar, 99.996%) and 0.4281 g thiourea (Aldrich, 99%) were separately dissolved in 15 ml D.I.

water. Along with 9.8 ml ammonium hydroxide (J.T. Baker, 28.0-30.0%), the CIGS samples were immersed into the beaker with a chemical solution. The beaker was put into a water bath at 68-70 ºC for 6 min with modest stirring. After the deposition, the samples were rinsed with D.I. water and baked at 200 ºC for 2 min on the hot plate.

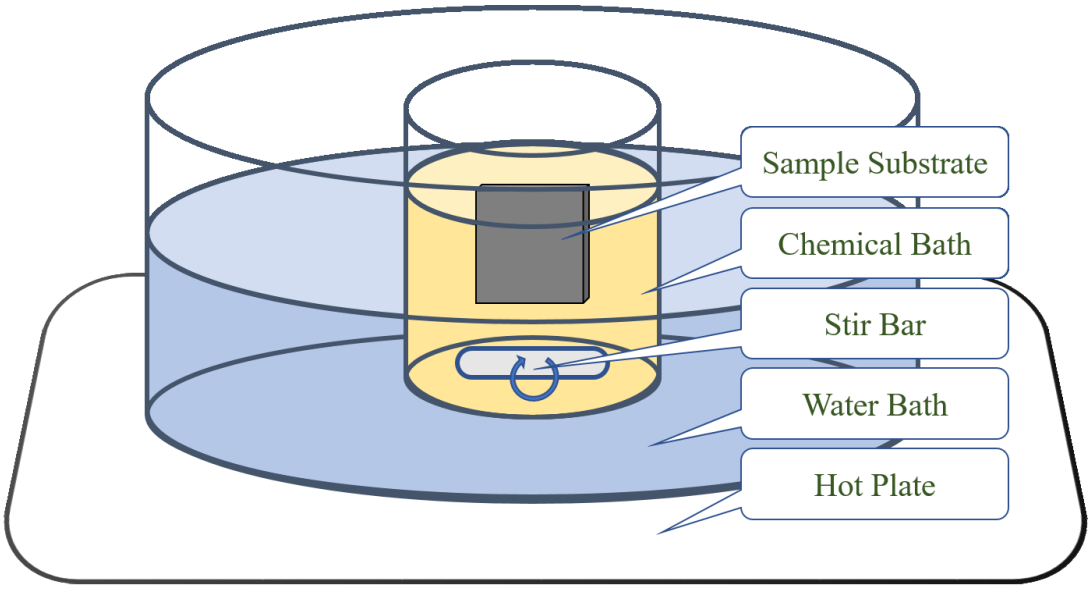

Figure 2-11 Schematic of CdS chemical bath deposition

2.5.5 Window layer deposition

Both intrinsic ZnO (i-ZnO) and 2% Al-doped ZnO (ZnO:Al, or AZO) in the window layer were deposited by RF magnetron sputtering. Both i-ZnO and AZO targets (3" diameter, ¼" thickness, no copper bonding and 99.99% purity) was purchased from Semiconductor Wafer Inc., Hsinchu, Taiwan. The sheet resistance of 300 nm AZO layer was measured as 50 Ω/□. The deposition condition is list below in Table 2-4:

Table 2-4 Sputtering conditions for window layer

Material	RF Power (W)	Time (second)	Gas flow (sccm)	Pressure (mTorr)	Thickness (nm)
Intrinsic ZnO	90	2400	O_2: 2 Ar:18	6	50
Al-doped ZnO	120	9600	Ar: 5	1	300

2.5.6 Top contact deposition

Silver paste (SPI, silver paste plus 05063) was initially used to verify if the devices were working. When preparing the devices for performance measurement, the thermal evaporated metallic Al was used as the top contact. The deposition current was set to 20 A, and deposition was 60 sec. A laser-cut shadow mask was used to pattern the Al grid and the dimension of individual device was defined by the mask as 3 mm × 3 mm.

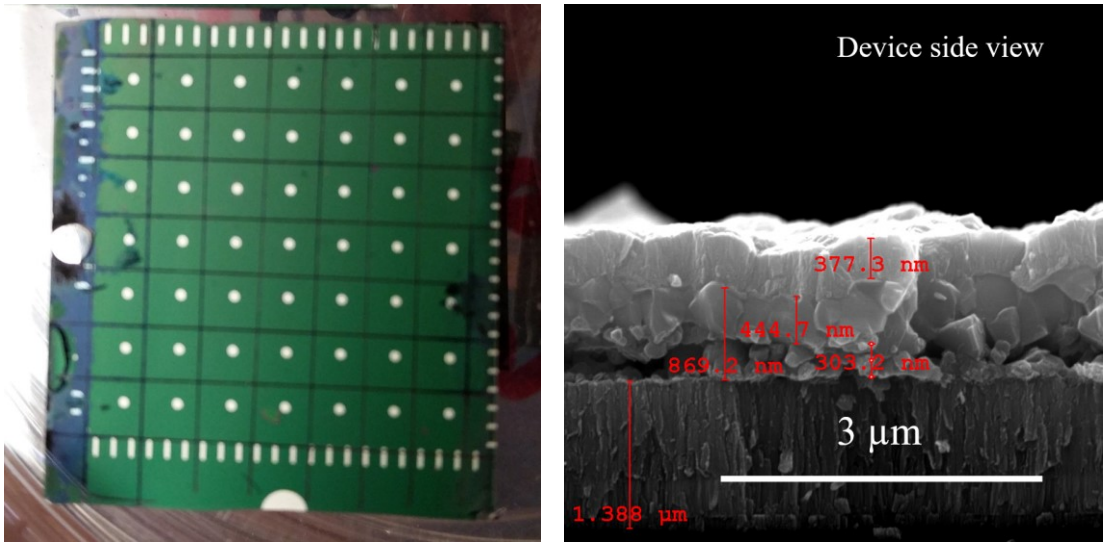

Figure 2-12 Finished CIGS PV devices sample and its SEM side view image

After the top contact was finished, the substrate was mechanical scraped into individual small devices for solar efficiency measurement. Figure 2-12 shows the final 1" × 1" samples and the SEM image in cross-sectional view.

2.6 Characterizations of the PV device

2.6.1 Current-voltage measurement

DC current-voltage (I-V, or unitized as current density-voltage J-V) measurement is one the most important characterization for solar cell devices. By sweeping the voltage applied to the device, short-circuit current (I_{sc}), open-circuit voltage (V_{oc}), maximum power (P_{max}), maximum current (I_{max}), maximum voltage (V_{max}), and fill-factor (FF) are measured and/or calculated.

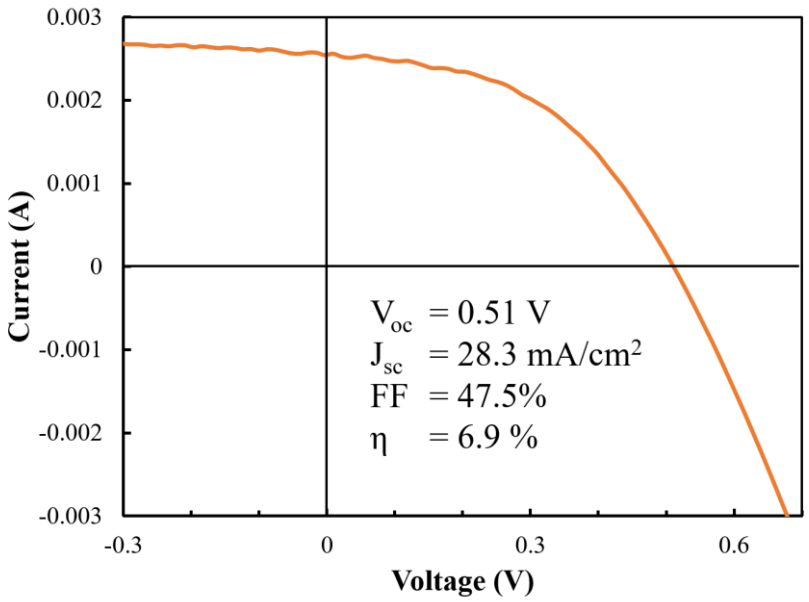

Figure 2-13 I-V measurement of the CIGS thin film solar cell under 100 mW/cm^2 AM 1.5 spectrum

Figure 2-13 is the I-V measure result of the CIGS thin film solar cell made by the oxides to selenides transition. The efficiency was measured by a sourcemeter under AM 1.5 solar simulator with 100 mW/cm^2 intensity.

2.6.2 Quantum efficiency measurement

Quantum efficiency (QE) indicates the ratio of the number of charge carriers collected by the solar cell to a particular wavelength photos from outside. There are two kinds of QE: 1) External Quantum Efficiency (EQE) is the ratio of generated charge carriers to all incident photons with a particular wavelength; and 2) Internal Quantum Efficiency (IQE) is the ratio of generated charge carriers to the absorbed photons with a particular wavelength.

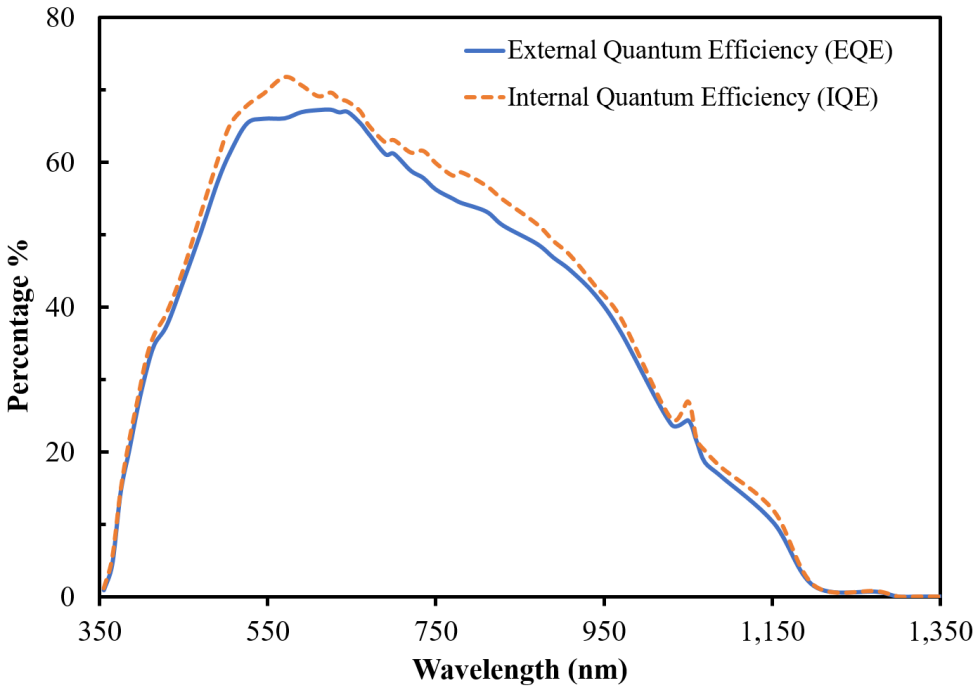

Figure 2-14 QE measurement of the CIGS thin film solar cell

Figure 2-14 shows the QE measured by a Flash QE system. It is a complex result of the QE loss compared to a theoretical QE of CIGS.[62] One of the main reason is the thickness of this device is only 850 nm which is lower than the optimized thickness of CIGS at 1~1.5 μm; other reasons include the defects introduced by thermal annealing during the selenization, relatively higher window layer resistance, etc.

2.7 Chapter summary

The route of chalcogenide thin film deposition from oxide thin film has been investigated. By a sol-gel process, alkoxide and carboxylate precursors can be deposited and converted into metal oxide thin films. Then the thin films are further transited into chalcogenide thin films by the chalcogen source with the assistance of hydrogen gas. Through this route, CIGS thin films were successfully deposited and the fully functional devices were made.

CHAPTER 3 From Metal to Chalcogenide:

Kesterite Thin Film Deposition from Electrodeposited Metal Thin Films

3.1 Cu_2ZnSnS_4 thin film solar cell

3.1.1 Manufacturing cost challenge of the solar cell

By directly converting the sunlight into electricity, the solar cell has the clean and convenient nature. To actually substitute the fossil fuels non-renewable energy, the price of solar power electricity should be comparable to the electricity generated from other mainstream non-renewable or renewable source. Thus, the competition for both the highest efficiency and the lowest cost is the fundamental driving force for the research and development of the PV materials and devices. The Swanson's law in PV industry is a similar prediction to the Moore's law in the semiconductor industry, which claims that the price of solar PV modules tends to drop 20% for every doubling of industry capacity. The c-Si solar module production cost was \$76.67/W in 1977,[63] while current PV module production cost of 6 members of Silicon Module Super League (SMSL) has dropped to less than 40 cents/W by the end of 2016.

With low material usage and easy fabrication process, the thin film solar cells are developed to reduce the cost of c-Si which is the dominant with more than 80% PV market share. The high absorption coefficient makes the thin film solar 100 times thinner than the c-Si PV device. While CIGS thin film PV is leading the efficiency competition, CdTe thin film PV is currently winning the half of the total thin film PV market due to its low cost per installation watt. First Solar Inc. is predicted to provide \$0.25/W CdTe module in 2019.[64]

Based on NREL's photovoltaic (PV) manufacturing cost analysis report, materials cost takes 70% of the CIGS thin film module cost.[65] The raw material cost is an important factor limiting the reduction of thin film PV cost. Table 3-1 lists the elements used in common thin film solar cell. Ga, In, and Te are among the low production and deficient elements which leads to a higher source price for the thin film PV. Thin film PV made from earth-abundant elements need to be developed to overcome the resource shortage for current CIGS and CdTe thin film PV.

Table 3-1 Abundance[2] and annual production[66] of elements used in thin film solar cells

Element	Cd	Cu	Ga	In	S	Se	Sn	Te	Zn
Abundance in the upper continental crust (ppm)	0.15	60	19	0.25	350	0.05	2.3	0.001	70
2016 worldwide production (ton)	23,000	19,400	375	655	69,300	2,200	280,000	400	11,900

3.1.2 CZTS earth abundant material for thin film PV

Copper zinc tin sulfide (Cu_2ZnSnS_4, CZTS) or copper zinc tin sulfide selenide ($Cu_2ZnSn(S,Se)_4$, CZTSSe) is a possible candidate for the earth abundant material thin film solar cell. When the In and Ga in CIGS crystal structure are replaced by zinc and tin, the I-III-VI chalcopyrite structure becomes I-II-IV-VI kesterite structure; Figure 3-1 shows CIGS chalcopyrite where In/Ga (III) in red is replaced by Zn (II) in purple and Sn (IV) in blue in the kesterite crystal of CZTS. CZTS has similar optical and electrical properties to CIGS: a large absorption coefficient over 10^4 cm^{-1}, a suitable band gap of 1.4~1.5 eV.[67] By introducing copper zinc tin selenide ($Cu_2ZnSnSe_4$, CZTSe) which has a band gap of 1.0

eV, the CZTSSe gets a tunable band gap between 1.0 and 1.5 eV due to the variation of the S:Se ratio.[68] Thus the thin film technologies developed for CIGS can be applied on the fabrication of CZTS solar cells.

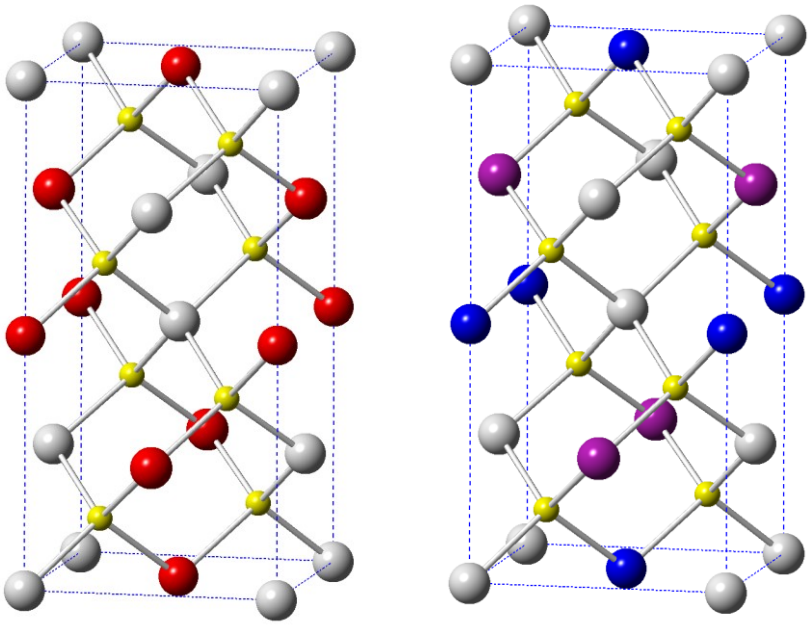

Figure 3-1 CZTS crystal structure (right) derived from CIGS chalcopyrite structure (left)

In 1977 Bell labs reported the early study on Cu_2CdSnS_4 (an analog to CZTS) PV and got 2% efficiency.[69] CZTSSe PV device efficiency reached 2.3% in 1997,[70] 2.63% in 1999,[71] and 5.45% in 2003.[71] The latest record is 12.6% reported by IBM and Solar Frontier by a hydrazine-based process in 2014.[72] Although the efficiency is just the half of CIGS PV, given the raw materials cost raising of In and Ga, CZTS will gain more competitiveness.

3.1.3 CZTS thin film deposition techniques

CZTS is born with the similar properties to the CIGS, therefore most CIGS thin film deposition techniques can be applied to CZTS. The vacuum-based techniques include

thermal co-evaporation,[71] layer-by-layer sputtering,[73] three-source co-sputtering,[71] and single quaternary sputtering.[74]

CZTS is also born to lower the manufacturing cost of the CIGS PV, so non-vacuum based techniques with lower setup and/or operation cost for CZTS have drawn more interest in the development of CZTS thin film deposition.

Nanoparticles ink methods have been applied to both CIGS and CZTS thin film deposition. The nanoparticles are dispersed in particular solvent and form an ink for either spin coating, ink-jet printing, spray pyrolysis, and dip coating on the substrate. After removing the solvent and further thermal annealing, the coating nanoparticles layer is converted into the desired PV material layer. Guo et al. reported the CZTS quaternary nanoparticles synthesized by hot injection, and the device PV efficiency reaches 7.2%.[75] Binary chalcogenides nanoparticles mixture has also been used to synthesize the CZTS thin film, which could significant improve the productivity compared to the hot-injection synthesis method for quaternary nanoparticles synthesis. Kim et al. reported a continuous process for CZTS thin film deposition by three binary sulfide nanoparticles streams and obtained a 9.08% efficiency device.[76]

Hydrazine-based dimensional reduction method is also playing an import role in the CZTS thin film deposition since it is the current highest efficiency record holder as 2017.[72] This method is mainly used by the researchers in IBM. After dissolving the copper chalcogenide, tin chalcogenide, zinc formate, and sulfur in hydrazine, a spin coating step in the controlled sulfur atmosphere at over 500 ºC, a 1.5~2.2 μm CZTSSe film was formed. The detailed of the dimensional reduction method will be discussed in Chapter 4.

Electrodeposition has also been used to prepare the precursor metals for CZTS thin film. Despite the initial setup cost is relatively high which includes the study and building of the plating bath, the advantages of electrodeposition include low operation cost, high material utilization, and easy scalability. Electroplating CIGS encounter the Ga deposition challenge due to the very negative reduction potential of Ga, while in CZTS, all three metals have a moderate reduction condition. Scragg et al. reported CZTS thin film deposition from elemental metal layers by electrodeposition, and obtained 0.8% efficiency from CZTS PV device.[77] A single step co-electrodeposition method was used by Schurr et al. to fabricate a 3.4% CZTS PV device.[78]

3.2 Electroplating metal thin film deposition

3.2.1 Basic of electrodeposition

In Section 1.3.3 the electrodeposition has been briefly introduced. Electrodeposition is a process using electrical current to reduce cations of a desired material from a solution bath and form a thin film coating onto a conductive substrate surface. Figure 3-2 shows a schematic of copper electrodeposition system. Italian chemist Luigi Brugnatelli is considered as the first person to facilitate the electrodeposition. In his experiment in 1805, a fine layer of gold on silver substrate was obtained. After then, electrodeposition has been used to deposit copper, gold, silver, and chromium from small primitive workshop to large industrial scale.

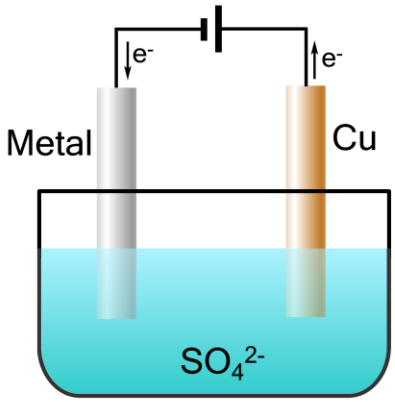

Figure 3-2 Schematic of copper electrodeposition process

The chemistry behind the process is relatively simple. Here the copper metal film deposition is used as an example:

The electrolytic bath contains copper cations and sulfate anions. When applied an external electric field, the cations migrate to the cathode where they are reduced into metallic copper and deposit on the cathode: $Cu^{2+} + 2e \rightarrow Cu$. On the other side, the copper metal from the anode dissolves into the solution to maintain the electrical neutrality of the whole bath: $Cu \rightarrow Cu^{2+} + 2e$. The overall process is a migration of Cu metal from the anode (usually metal chunk) to the cathode (turning into a uniform thin film coating in most applications).

3.2.2 Layered electrodeposition vs co-electrodeposition

Applying the mature electrodeposition technique and fabricate large area CZTS thin film is an ideal route for low-cost industrial manufacturing. Both elemental metal layers electrodeposition[77] and co-electrodeposition[78] have been successfully used for CZTS thin film in research scale. The co-electrodeposition is more complex than the metal electrodeposition because the co-electrodeposition involves the four elements including

chalcogen precursors such like SeO_2. Electrodeposition of elemental metal layers followed by chalcogenization is an economical choice since the co-electrodeposition film still need post-deposition annealing treatment.

Here in this research, the sequential elemental layer electrodeposition is used to deposit a metal stack containing Cu, Zn, and Sn. The thermodynamic data favors the conversion from metal precursors to chalcogenides when the metals are reacting with chalcogen.

3.3 Cu, Zn, Sn electrodeposition

3.3.1 Cu plating

Three basic types of the bath are available for Cu electrodeposition: alkaline (cyanide and non-cyanide), acid (sulfate and fluoborate), and mildly alkaline (pyrophosphate) complex baths. Alkaline cyanide bath can obtain a better thickness uniformity than the acid bath. However, one of the important thing about the cyanide bath is its toxicity and needing well handling and special treatment for the waste.

Table 3-2 Copper plating bath

Chemical	$CuSO_4 \cdot 5H_2O$	H_2SO_4 (96%)	HCl (35%)	PEG (carrier)	SPS (brightener)
Concentration	75 g/L	106 ml/L	70 ppm	70 ppm	20 ppm

Acid sulfate bath is chosen because it is one of the simplest electroplating setups for copper and other metals. The experience on Cu plating can be applied to another two metals. The main constituents are copper salt and sulfuric acid, but additives are important in the plating process which help obtain the desired morphology of the coating. Chlorides are mild

plating inhibitors, which stabilized the Cu^{+} cations that serve as an intermediate during the reduction of Cu^{2+}. HCl is one of the common chlorides used in electrodeposition. The carriers are plating suppressors which create a diffusion layer at the anode to control the Cu^{2+} releasing from the anode to the plating bath. Polyethylene glycol (PEG) and other longer polyalkylene glycol (PAG) are common carriers. Brightener are used to promote the grain refinement, by packing at the higher electropotential area of the cathode and forcing the copper to deposit elsewhere. The first choice of brightener in Cu electrodeposition systems is bis-(sodium sulfopropyl)-disulfide (SPS). The recipe of the bath for copper plating is listed in Table 3-2.

Since the ultimate purpose of the CZTS thin film is to fabricate PV device, bi-layer Mo-coated glass was used as the substrate. It is conductive which could be directly used as the cathode. But unfortunately, the Mo is more reactive than Cu in the metal reactivity series, make it is easy to dissolve into the Cu bath. To protect the Mo layer, a thin layer of Cu of 90~95 nm was used to cover the Mo layer by DC magnetron sputtering.

Figure 3-3 shows the metallic Cu deposited by electrodeposition and its SEM image. The surface was shining and had an average grain size of 282 nm.

The Cu plating conditions were then optimized to an effective current of 0.3 A with a forward bias on/off ratio of 60/20. Figure 3-4 shows that the Cu thickness and electric charge (Amp-time) have a linear relationship, and the deviation is within the size of data point marker. The average thickness of Cu layer using 0.3 An effective current and 0.4 Am condition was measured at 281.3 nm.

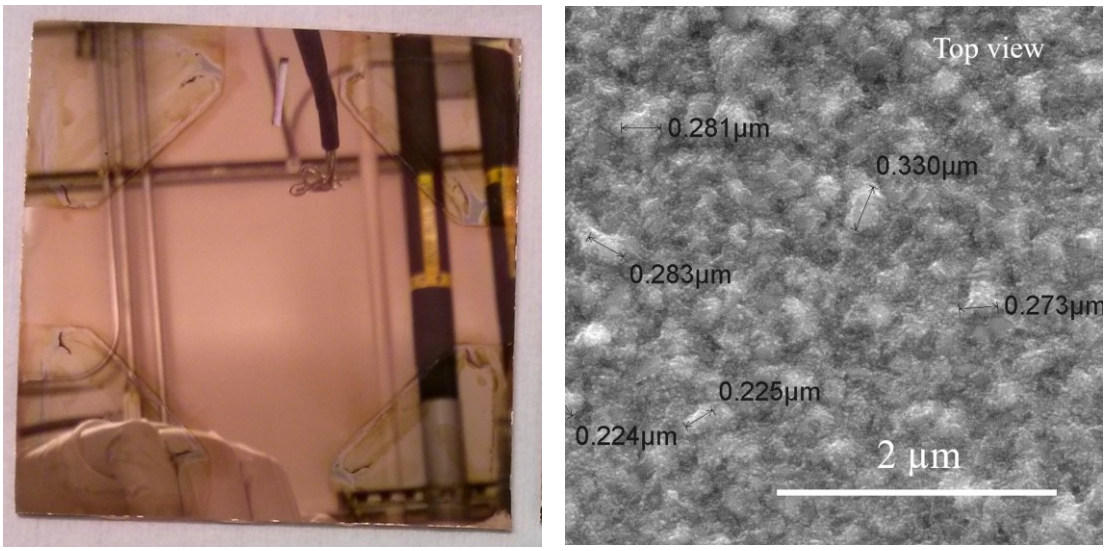

Figure 3-3 Digital photograph (left) and SEM image (right) of electrodeposited Cu thin film

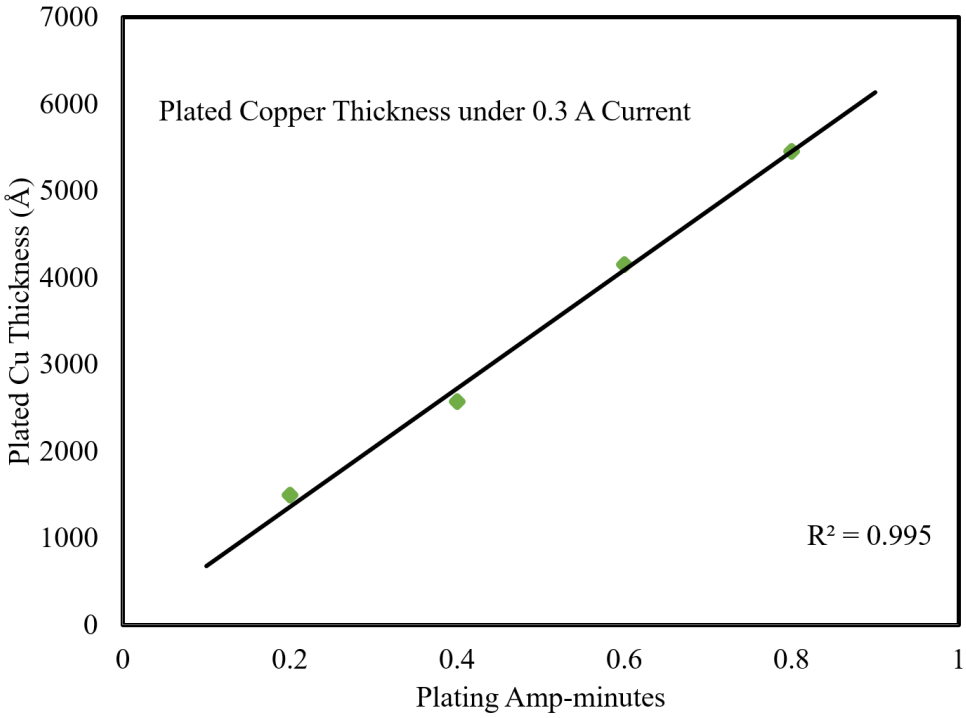

Figure 3-4 Cu thickness vs. plating charge (Amp-minutes)

3.3.2 Zn and Sn plating

Similar to the Cu plating study, Zn and Sn plating conditions were investigated.

Zn plating with higher effective current (0.6 A) resulted in a shining and smooth film. Due to the short duration of the plating process, the thickness control was in ±30 nm range. In order to have better thickness control, the effective current had been reduced to 0.3 A. In this case, the film thickness is constant at 202.3 ±5 nm, but the surface is not as shining or smooth. To compromise it, the effective current was set to 0.4 A by adjusting the pulsed forward current on/off ratio to 1:1, while keeping the forward current as 0.8 A. This condition results in better thickness control in less than 10 nm range. Figure 3-5 shows a comparison of Zn surface at 0.6 A and 0.4 A, and the grain sizes are 285 nm and 230 nm respectively.

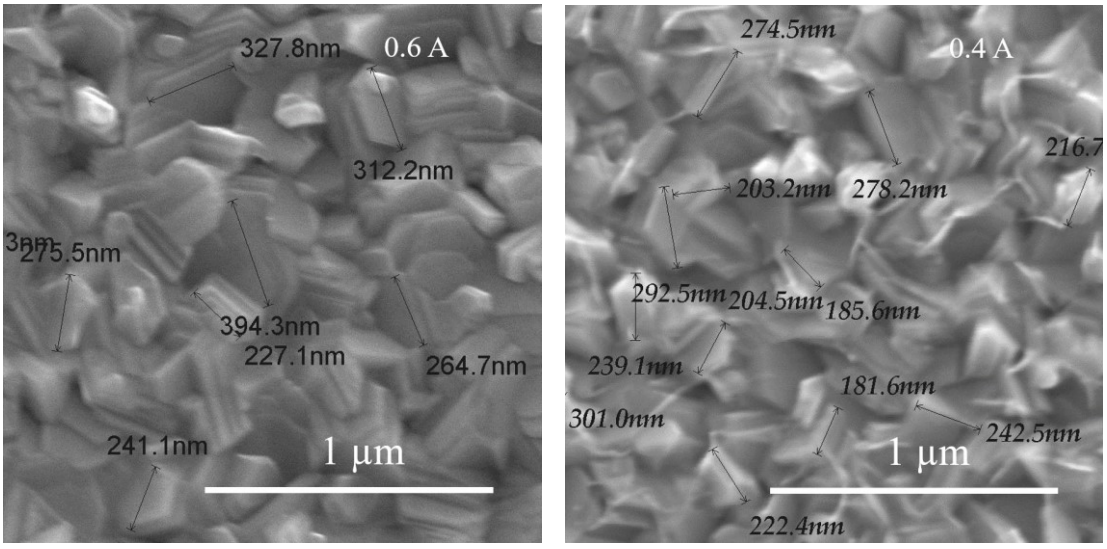

Figure 3-5 SEM images of Zn film with 0.6 A effective current and 0.4 A effective current

The Zn thickness was controlled by plating time. Figure 3-6 shows the relationship between Zn thickness and electric charge (Amp-time). From 200 nm to 600 nm, it showed a good linear relationship.

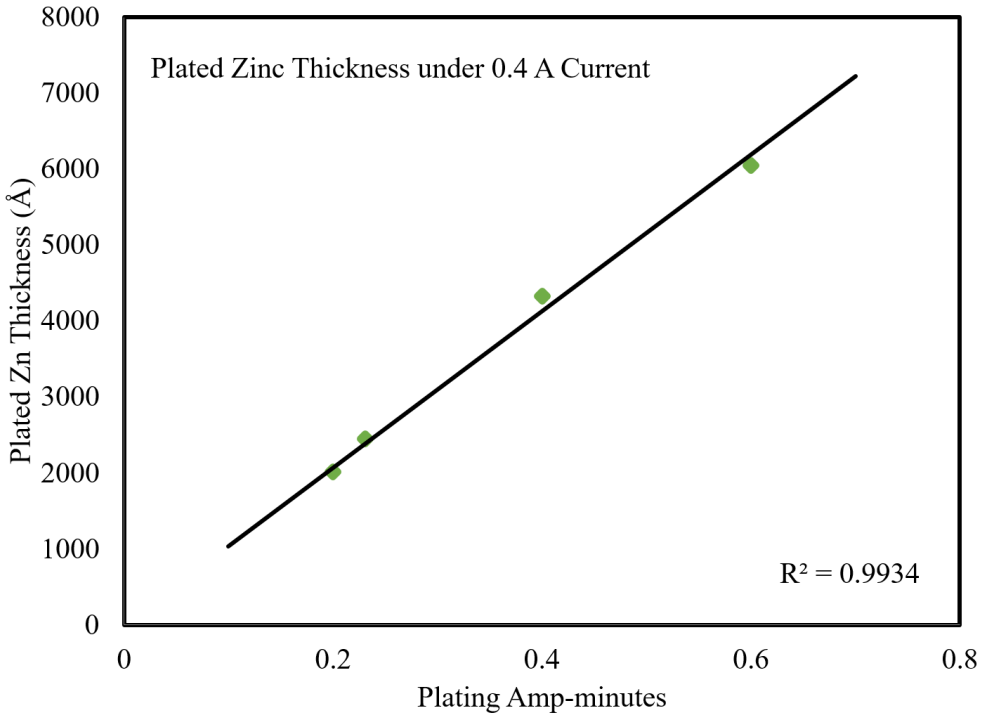

Figure 3-6 Zn thickness vs. plating Amp-min

Sn was then plated onto the Zn/Cu films. The plated Sn showed good coverage and good adhesion to the underlying Zn layer, however, the grain size was excessively large measuring up to 2.5 μm for all conditions. Figure 3-7 shows there was a very slight grain size change along with the effective current, the lower current resulted in the smaller grain size. Also, the surface of the Sn layer was very rough. The profilometer reported the roughness R_a = 47.1 nm within a range of R_t = 124.1 nm with 0.4 A and 0.1 Amp-min condition.

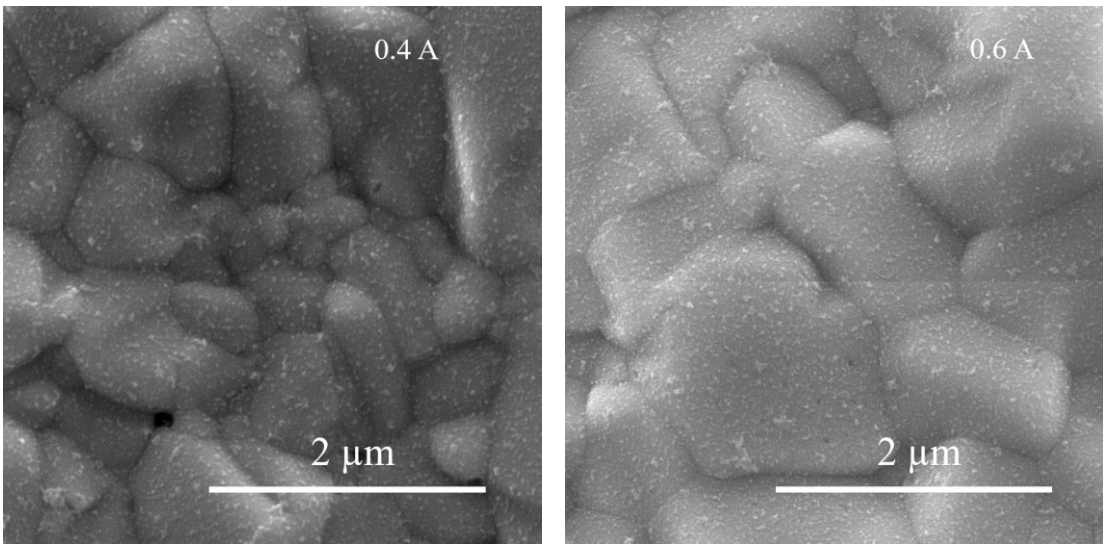

Figure 3-7 SEM images of Sn film with 0.4 A effective current and 0.6 A effective current

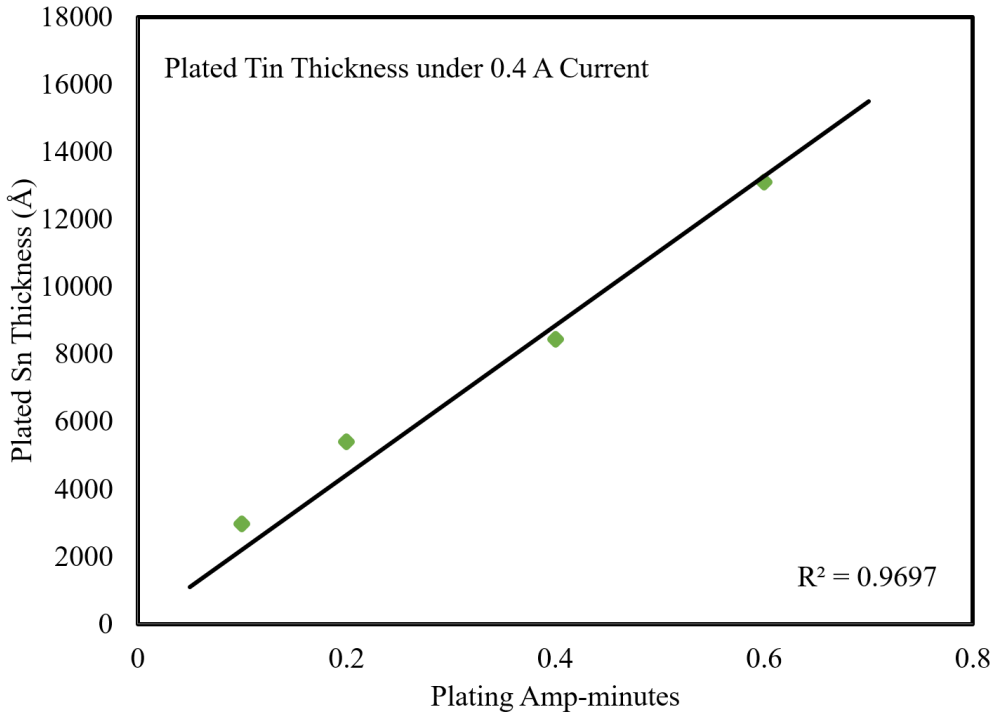

Figure 3-8 Sn thickness vs. plating Amp-min

It was suspected that during the Sn plating, the Zn layer was dissolving into the Sn sulfate solution. Inductively coupled plasma optical emission spectrometry (ICP-OES) was

performed on the Sn bath to look for foreign contaminants, specifically Zn. After one month of using the Sn bath, the Zn concentration in the Sn bath increased to 232 ppm which was 640 times higher than the original bath. Table 3-3 shows the ICP-OES result for Zn concentrations.

Table 3-3 ICP-OES result for the Zn concentration in Sn bath

Zn conc. (ppb)	**#1**	**#2**	**#3**	**Avg.**	**Std Dev**	**%RSD**
1:10 diluted Tin Bath	23250	22910	23040	23070	171	0.7419
Background	362.0	356.0	352.0	356.7	5.0	1.411

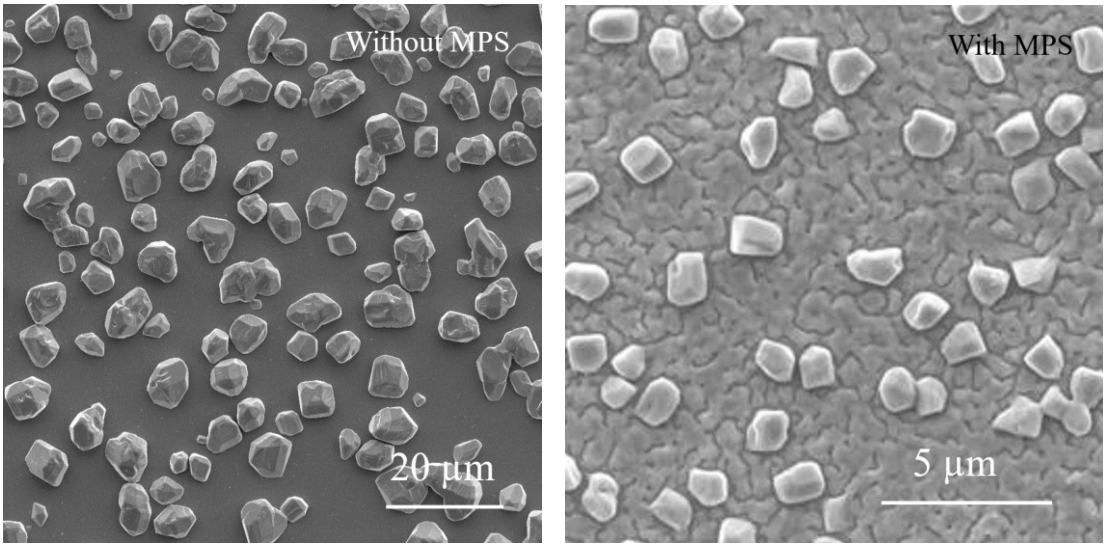

Figure 3-9 SEM images of Sn film without MPS additive and with MPS

This issue led to a reorder of the sequence of the Cu/Zn/Sn stack. A new order of Cu/Sn/Zn was used to prepare the metal precursors thin film. The additives in the Sn bath were studied to accomplish the Sn plating over Cu layer. The additives are listed in Table 3-4. Figure 3-9 shows the brightener sodium 3-mercapto-1-propanesulfonate (MPS) improve

the coverage of the Sn on the Cu substrate. Without MPS, the Sn will grow as giant nodule island (note the different scale bars in these two images).

Table 3-4 Additives in Sn bath

	Conc.	**#1**	**#2**	**#3**	**#4**	**#5**	**#6**
MPS	5% in water	0	40 µL	80 µL	200 µL	1 mL	3 mL
PEG	1.0 mg/mL	0	0 µL	80 µL	200 µL	200 µL	200 µL
Gelatin	5% in water	0	40 µL	80 µL	200 µL	1 mL	1 mL

To remove the islands on the Sn surface, another non-ionic surfactant Tween 20 was introduced as a wetting agent with a concentration of 5 ml/L. Figure 3-10 shows the morphology improvement was significant.

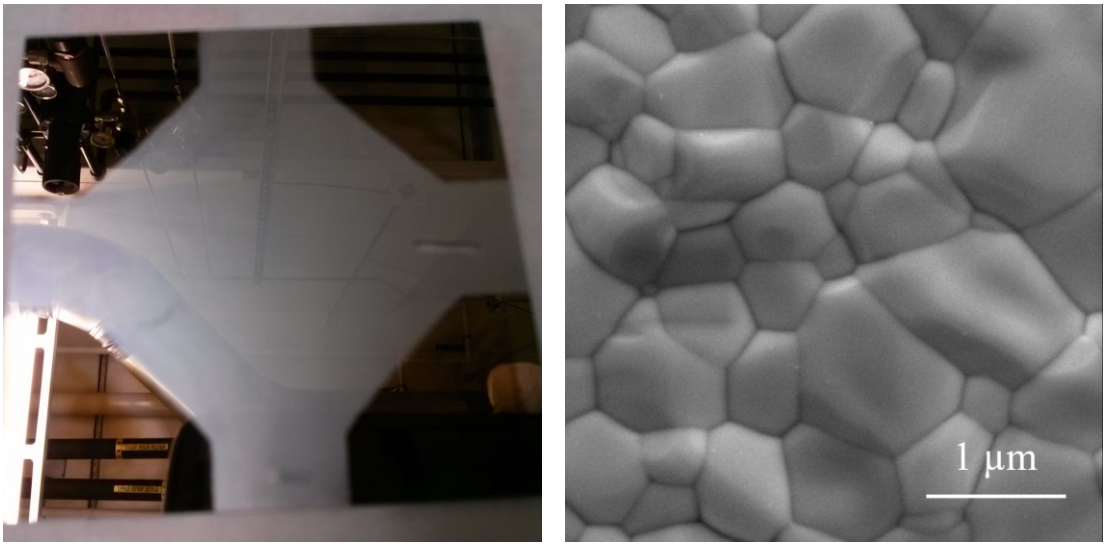

Figure 3-10 Digital photograph and SEM images of Sn film with Tween 20 wetting agent

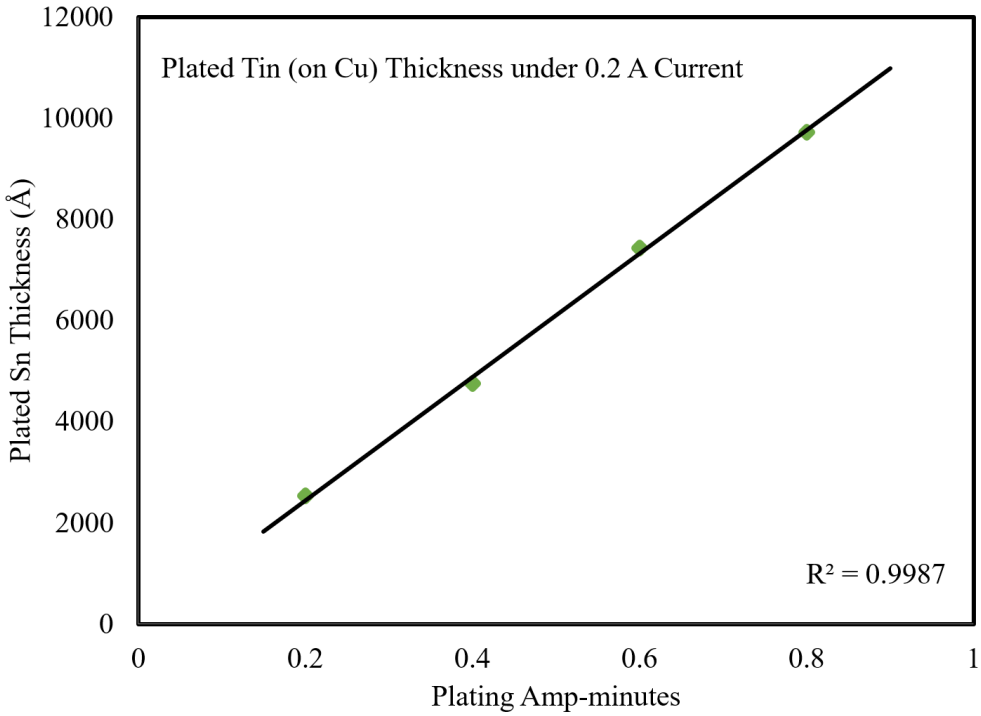

Figure 3-11 Sn (on Cu) thickness vs. plating Amp-min

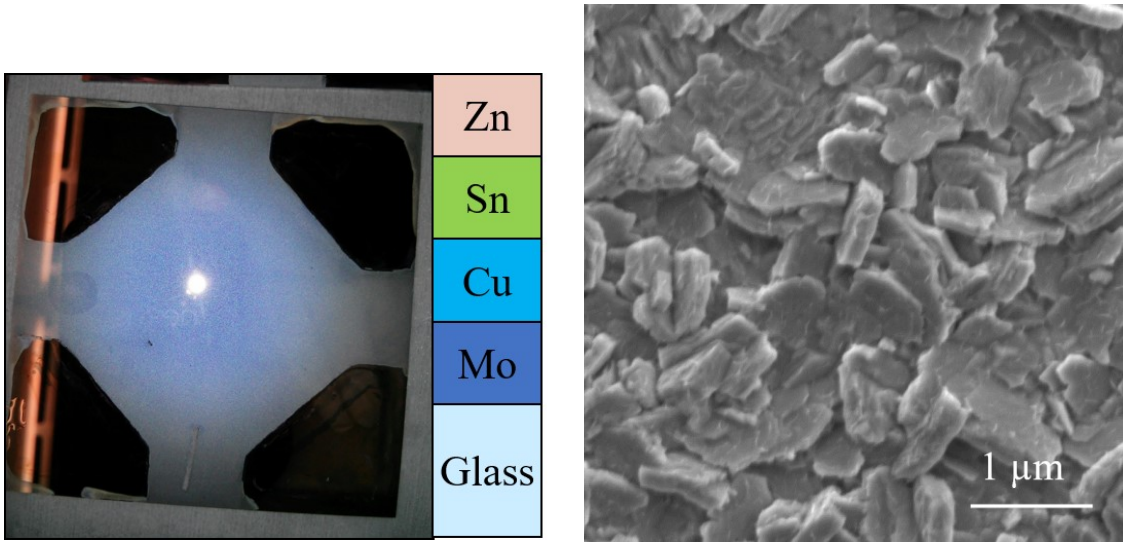

Figure 3-12 Digital photograph and SEM image of finished Cu/Sn/Zn stack

The plating condition and rate of Sn plating on the Cu film were studied with new bath recipe. Figure 3-11 shows the new relationship between thickness and amp-minutes.

Combined with the previous studied Cu and Zn plating condition, all three metal precursors were ready for the further sulfurization process, the SEM image is shown in Figure 3-12.

3.4 Pre-annealing of metal thin film stack

3.4.1 Pre-annealing process

Low-temperature annealing of the Cu/Sn/Zn stack prior to sulfurization was used to produce the better mixing of Cu, Sn, and Zn. This process is also called soft annealing. During the pre-annealing, alloys of these three kinds of metal were formed. XRD was used to check the alloy formation, and energy-dispersive X-ray spectroscopy (EDS) was used to track the elemental ratio changing. Figure 3-13 shows the flow chart of this procedure.

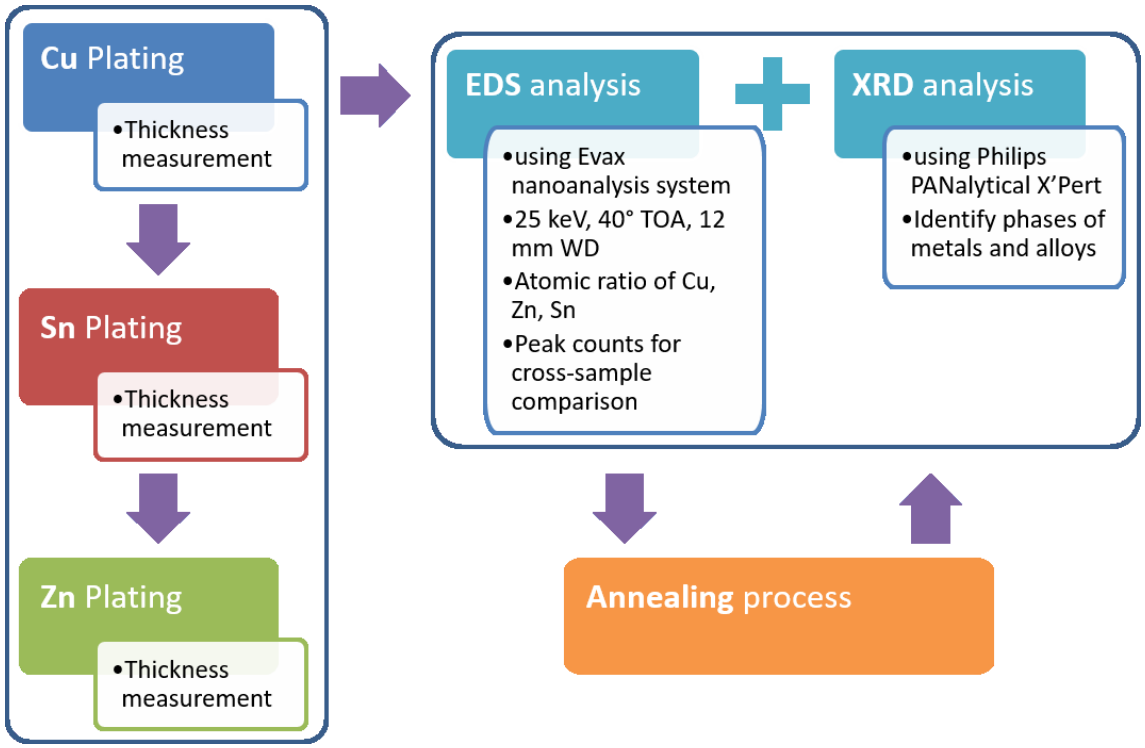

Figure 3-13 The procedure of pre-annealing study

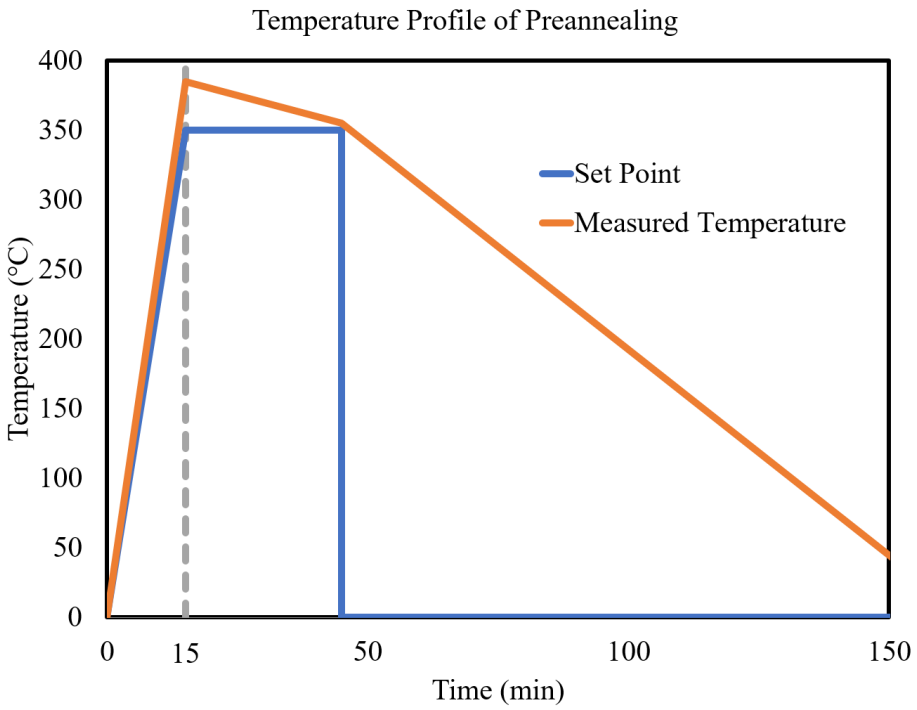

Figure 3-14 Temperature profile of a 350ºC pre-annealing

Figure 3-14 shows a pre-annealing temperature profile. The sample with Cu/Sn/Zn metal on Mo-coated glass was loaded into a tube furnace. The tube was purged with Ar, and the whole pre-annealing process was at atmospheric pressure.

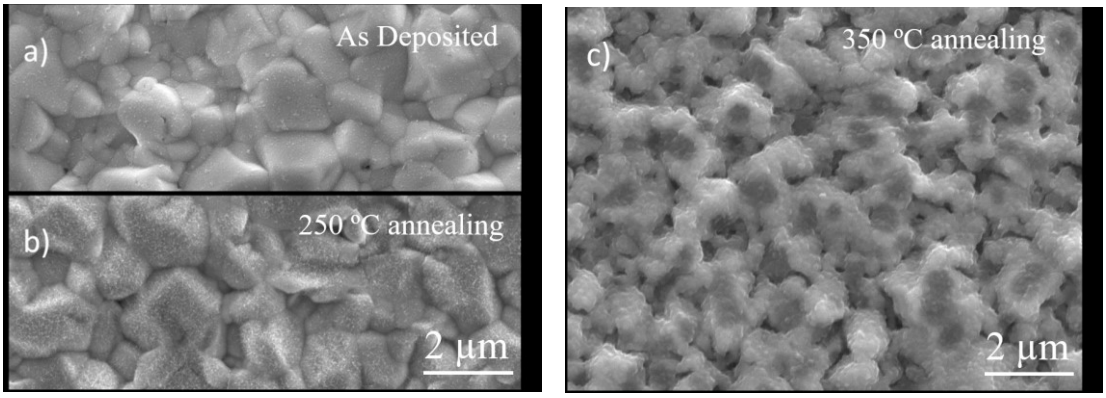

Figure 3-15 SEM images of Cu/Sn/Zn stack at different pre-annealing temperature

Figure 3-15 shows the SEM images of the resulting morphology produced after pre-

annealing of the Cu/Sn/Zn metal stack. The morphology of Cu/Sn/Zn metal stack shows little change before and after 250 ºC annealing. The resulting morphology using an annealing temperature of 350 º C shows finer grains which could indicate the successful phase transition.

3.4.2 XRD characterization

In order to check the alloy formation, XRD was used to study the sample before and after the pre-annealing process.

Figure 3-16 shows only metal peaks are observed after electrodeposition, while Figure 3-17 shows after pre-annealing, the intensity of metal peaks significantly reduced along with the copper-tin alloy formation.

3.4.3 EDS study of metal loss during pre-annealing

Since both the metal Sn and Zn have low metal points, 232 ºC and 420 ºC respectively. The vapor pressure of metal during the pre-annealing might need to be considered. Sn layer is covered by Zn which can prevent the Sn loss, while Zn is directly exposed to the gas phase. At 350 ºC, the Zn solid vapor pressure is calculated as 858 Pa (0.008 bar).

The sample was prepared by controlling the thickness to achieve an element ratio for Cu/Sn/Zn to 0.5:0.25:0.25 based on the CZTS stoichiometry. The Sn underneath the Zn showed slightly lower EDS counts and the elemental ratio was calculated as 0.5:0.23:0.25 based on the assumption that Cu is constant 0.5. After 350 ºC annealing, the ratio turned to 0.5:0.31:0.12. The Zn loss was not ignorable, and due to the thinner Zn layer, EDS counts for Sn increased.

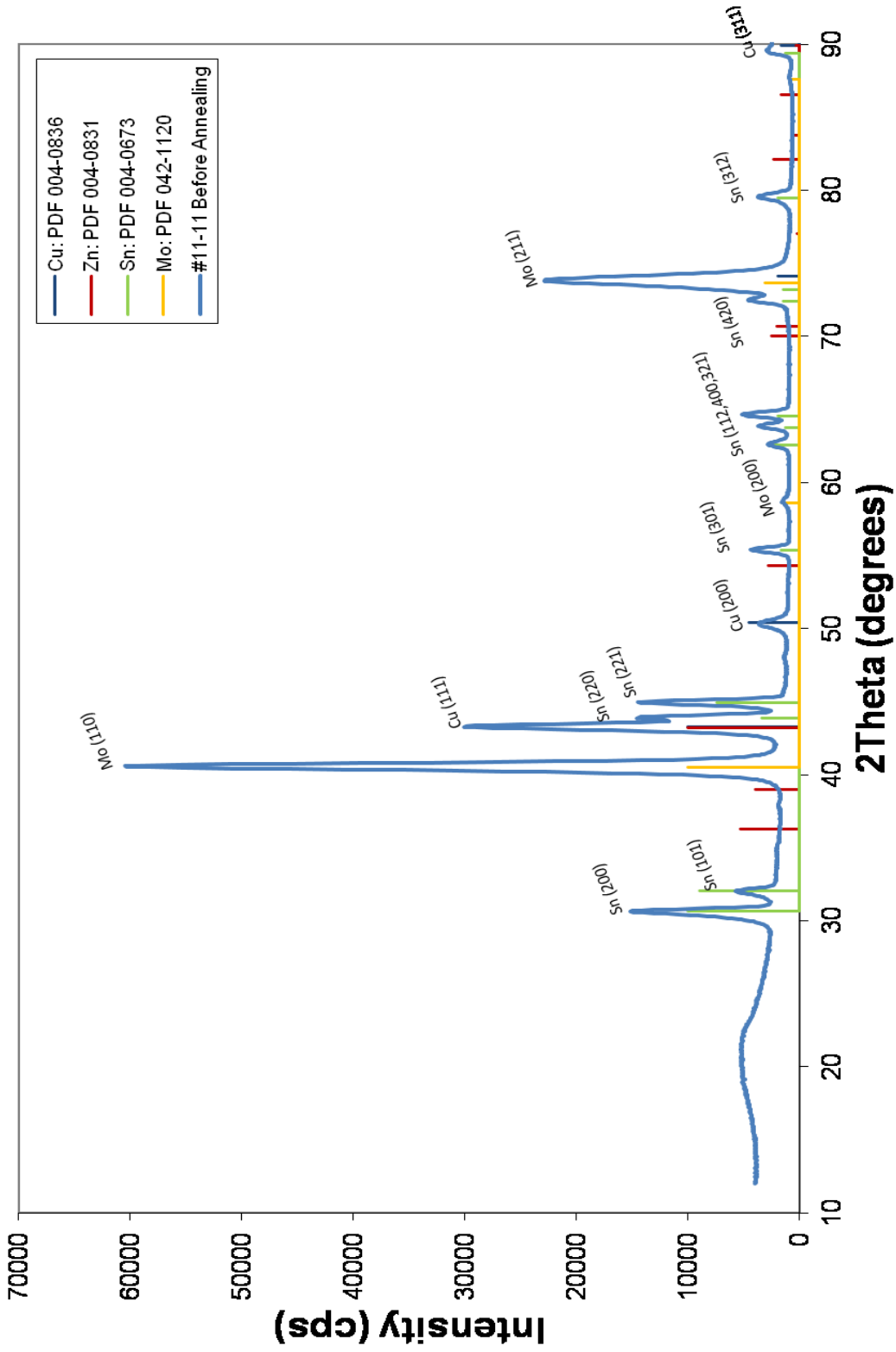

Figure 3-16 XRD of as deposited metal stack before pre-annealing

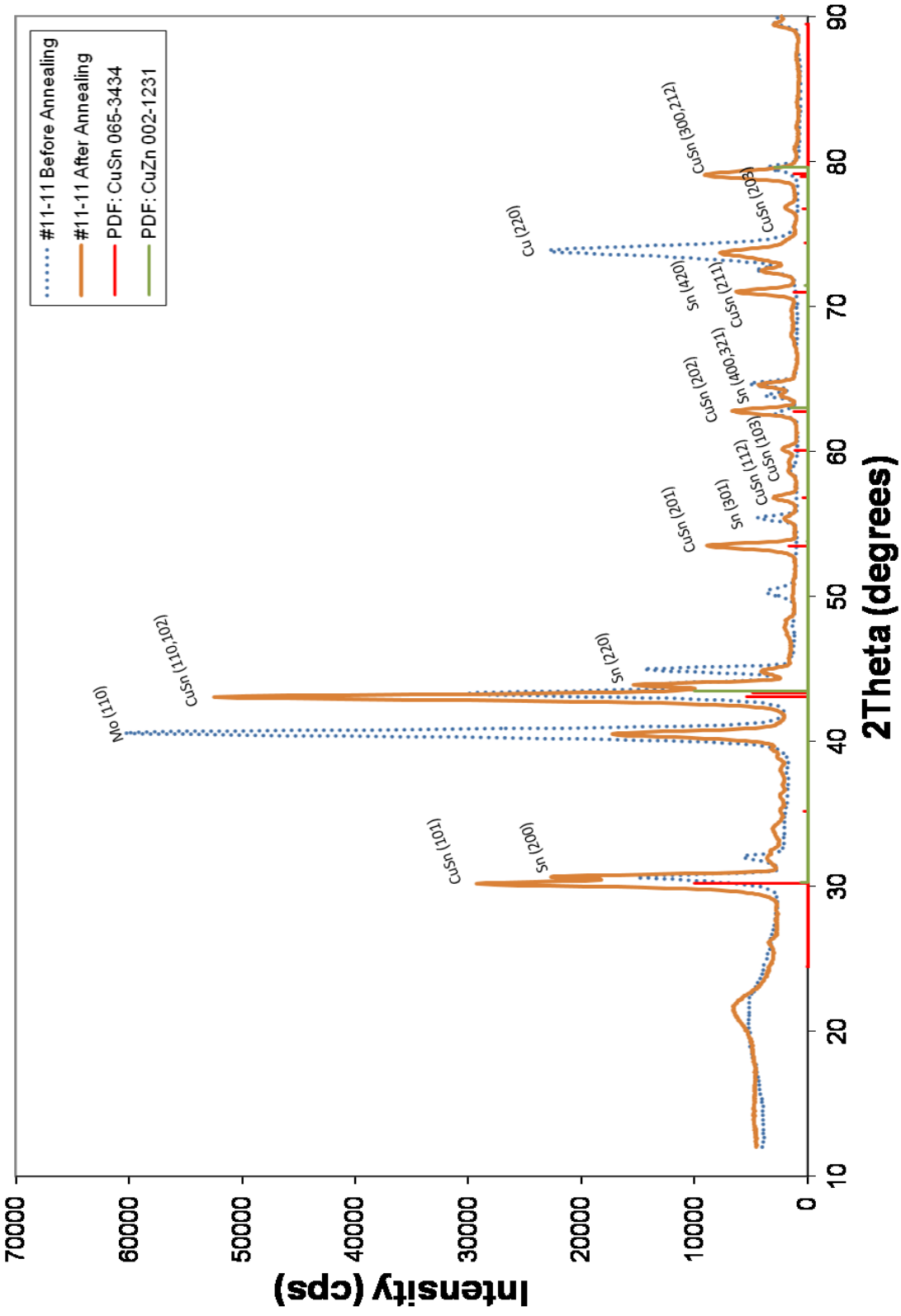

Figure 3-17 XRD of the metal stack after 350 ºC pre-annealing

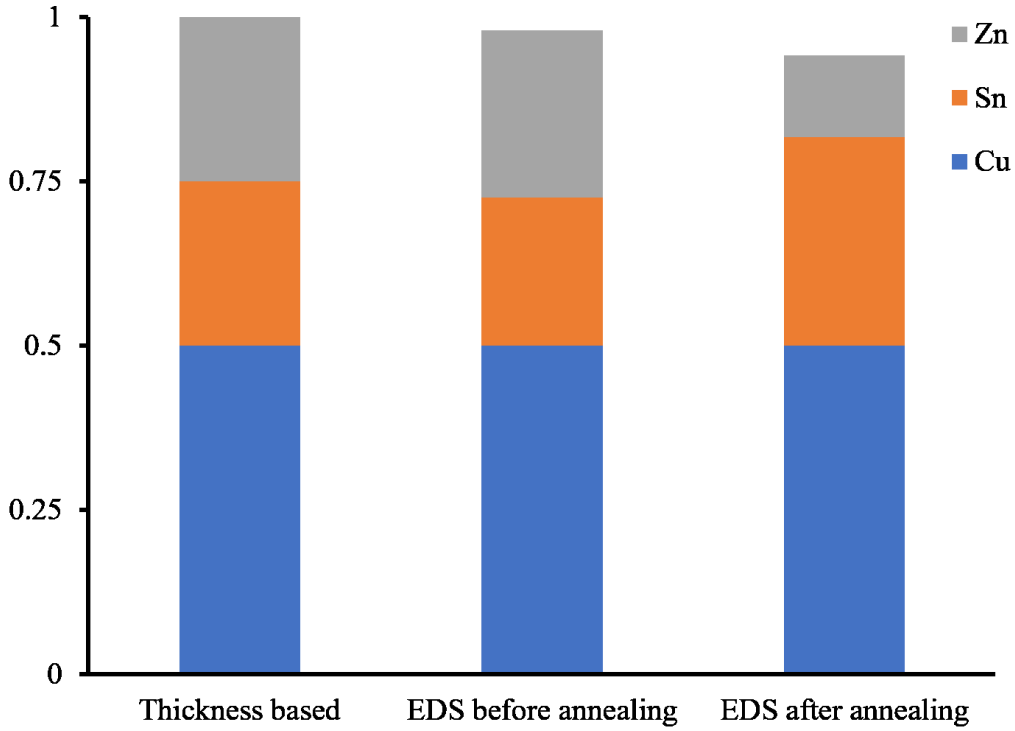

Figure 3-18 Elemental ratio of the metal stack before and after 350 ºC pre-annealing

Figure 3-18 shows the Cu/Sn/Zn elemental ratio unified based on the Cu before and after pre-annealing.

To compensate the Zn loss during the pre-annealing, the simplest solution is increasing the electrodeposition thickness of Zn. By the trial and error procedure shown in Figure 3-13, the as-deposited stack with Cu/Sn/Zn = 2:1:1.5 will yield a 2:1:1 final elemental ratio after the 350 ºC pre-annealing.

3.5 Sulfurization for the CZTS thin film

3.5.1 Sulfurization condition study

With the metal precursors at the correct elemental ratio, the sulfurization can be carried out. The setup shown in Figure 3-18 is used for sulfurization which uses the same furnace shown in Figure 2-3.

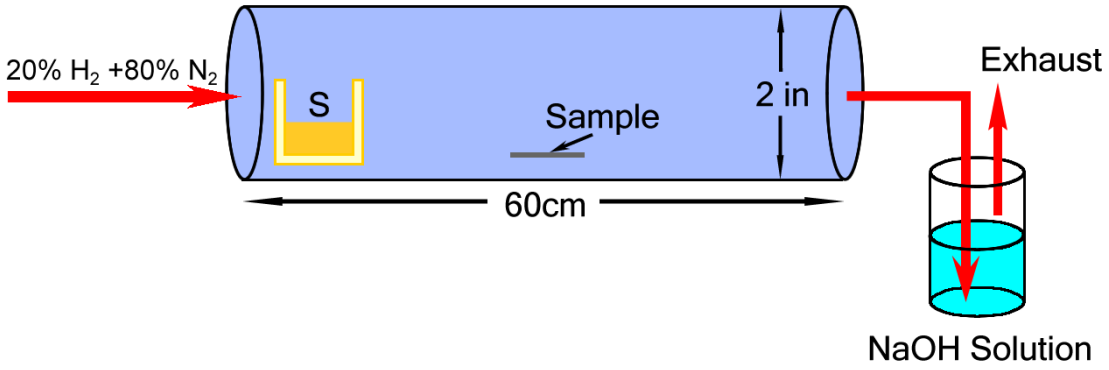

Figure 3-19 Schematic of CZTS sulfurization annealing furnace setup

There are several differences between the two setups for selenization and sulfurization:

1) Sulfur powder source is loaded into a crucible which is placed at the edge of the furnace. The reason is the melting point and boiling point of sulfur are 115.2 ºC and 444.6 ºC respectively. When the system is heated to 550 ºC, if the sulfur is loaded in the center of the furnace, the sulfur will be quickly vaporized and can not keep enough sulfur vapor pressure during the whole sulfurization process.

2) Since the sulfur source has been moved to the cooler area, the sample is directly placed in the center of quartz tube facing up, where the temperature should be close to the thermal couple reading.

3) H_2 is not a requisite in the metal sulfurization process. Both pure N_2 and 20% H_2 in N_2 forming gas are used to make the comparison, and 20% forming gas is chosen because it yielded a better conversion. It could be due to two reasons: a) H_2 forms the H_2S gas with sulfur and works as a carrier of sulfur and also is more reactive to react with the metal precursor. b) the top surface layer of metal could have been oxidation to a certain extent, which prevents the elemental sulfur to substitute the oxygen in the film without H_2 directly.

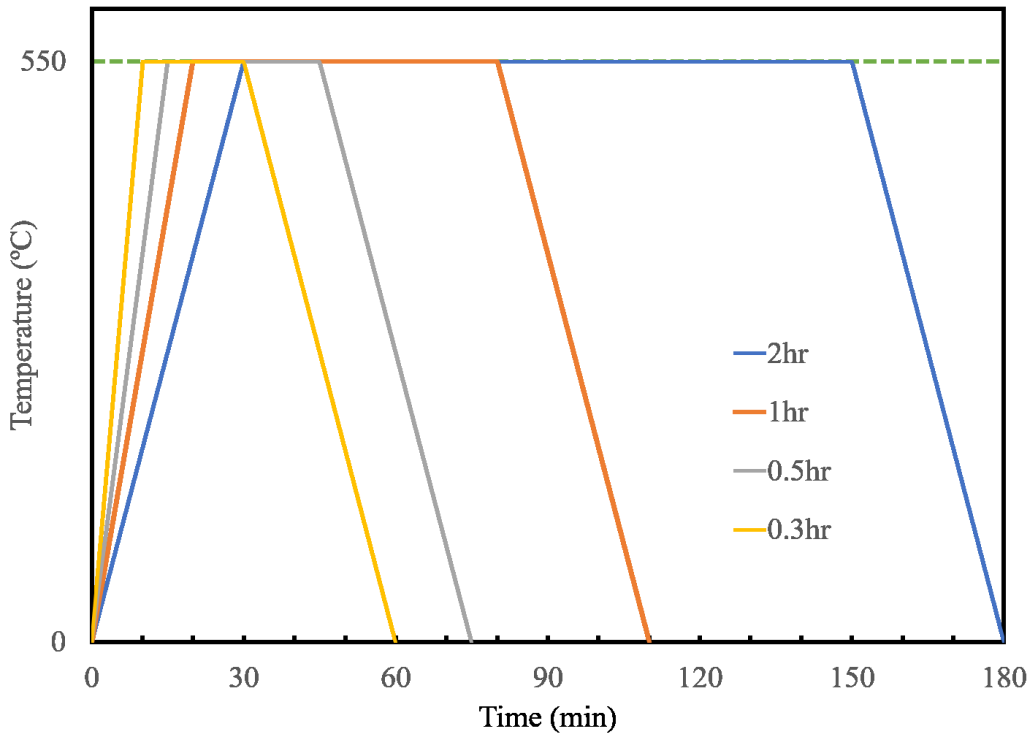

Figure 3-20 Temperature profile of the CZTS sulfurization study

There are two stages in the sulfurization process: the first stage is the sulfurization period with the effective S/H_2S diffusing into the metal film and forming the sulfides. The second stage is the crystallization and crystal growth period of the CZTS.

Figure 3-20 shows the sulfurization profile study for the Cu/Sn/Zn metal stack. The tube was heated to 550 ºC then kept for different lengths of time to study how the annealing time length affects the final CZTS film quality.

3.5.2 Characterization of the CZTS thin film

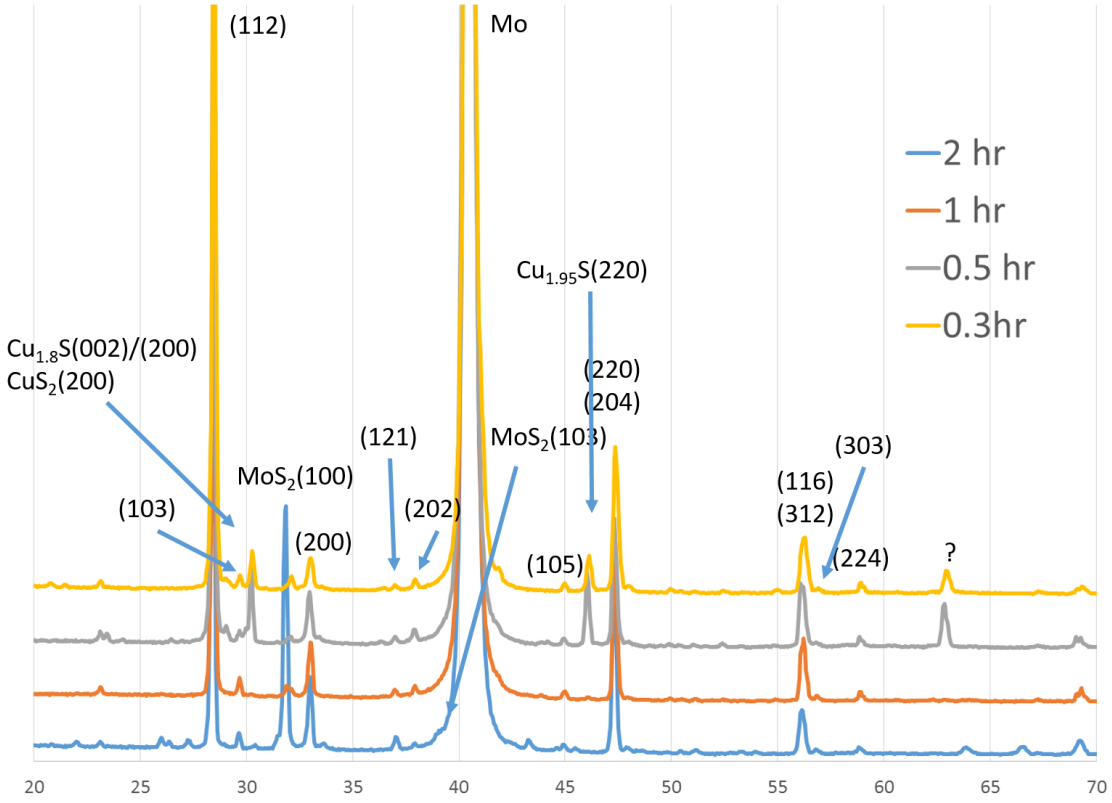

Figure 3-21 XRD result after sulfurization with different lengths of sulfurization time

XRD result in Figure 3-21 shows the formation of CZTS after the sulfurization. CZTS characteristic peaks (112), (200), and (312) are all shown in the results. In both results of 0.3 hr and 0.5 hr sulfurization, the Cu_2S byproduct phase exists in the XRD result. When the sulfurization process is extended to 2 hr, the Mo underneath the CZTS is sulfurized into MoS_2. Thus 1 hr sulfurization is a compromised condition to get pure CZTS phase without damage the Mo back contact.

Figure 3-22 shows the SEM image of CZTS thin film. The coverage and crystallization are good for the 550 ºC 1 hour sulfurization result.

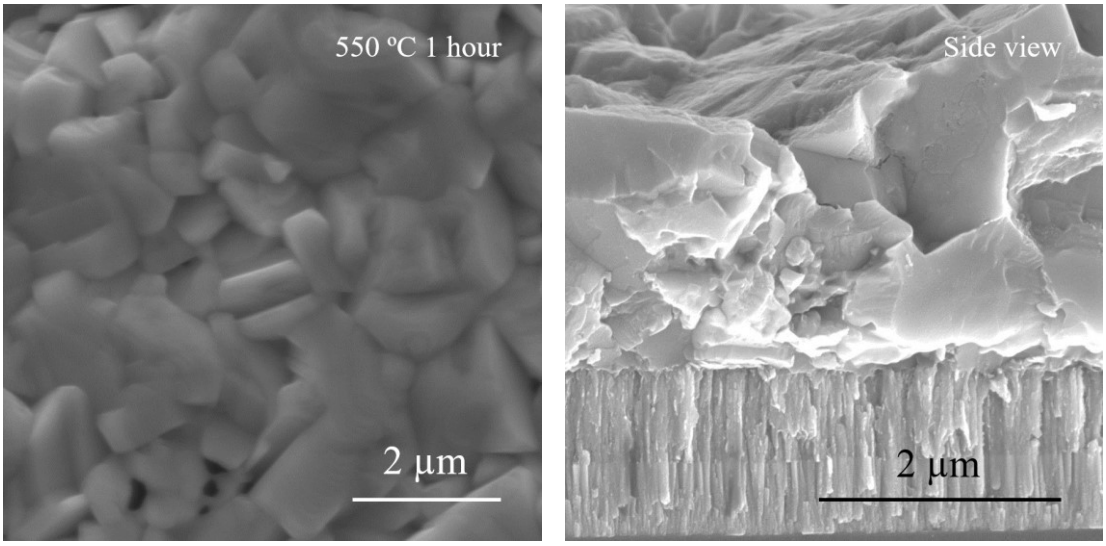

Figure 3-22 SEM images of sulfurized CZTS thin film at 550 ºC for 1 hour

3.5.3 PV device I-V measurement

The sulfurized sample was used to fabricate CZTS thin film PV devices. The device uses the same substrate structure used in Chapter 2 for CIGS thin film PV device. Figure 3-23 shows the measured I-V curve of one of best devices from the sample. The efficiency is 4.5% under the AM 1.5 100 mW/cm^2 solar simulator condition. Fill factor is as low as 41%

which due to the low shunt resistant of the PV device. Also, this device has a high series resistant which could be due to the high resistance of the window layer ZnO:Al.

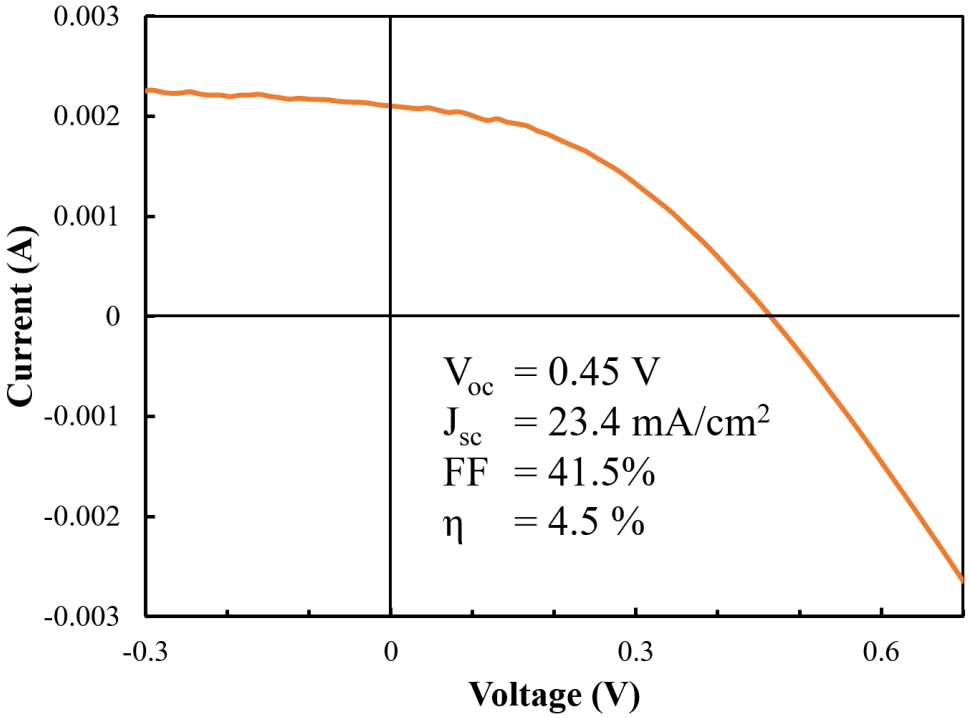

Figure 3-23 I-V measurement result of a CZTS thin film PV device

3.6 Chapter summary

CZTS is an alternative choice for thin film solar cell due to its low raw materials cost. To further reduce the production cost, layer-by-layer electrodeposition is chosen as a mature process technique in industry. The thin films have been deposited on the Mo-coated glass substrate by the electrodeposition process followed by sulfurization annealing. Both the pre-annealing condition and sulfurization condition are studied. Fully functional PV devices were successfully fabricated based on this technique. Although 4.5% efficiency is

still way behind the 12.6% champion CZTS PV device record, it proves the feasibility of this route.

CHAPTER 4 From Bulk Material to Thin Film Chalcogenide: MoS_2 Thin Film Deposition by Dimensional Reduction

4.1 Introduction to the dimensional reduction

4.1.1 Propose of the dimensional reduction

Both chemical bath deposition, and chalcogenization for oxides and metal film are chemical reaction turning the precursors which are different to the final products into the chalcogenides. While the electrodeposition of metal thin film is in a different way: Although the electrochemical reaction happened at both cathode and anode, the overall process is a migration of the metal copper from anode to cathode, or based on the final appearance we can say it transforms the chunk metal, e.g. Cu, on anode into a metal thin film on cathode.

Since the bulk metal chalcogenides exist in ore naturally and even the refined metal chalcogenides are cheaper than metal and other salts in most case. It makes us wonder if the metal chalcogenide can be processed in a similar way like electrodeposition: If the bulk chalcogenides in chunk or powder form can be dissolved into a solution, forming a wet film, then after evaporating the solvent, the chalcogenides thin film will be achieved. Unfortunately, most metal chalcogenides have extremely low solubility in water. An alternative solvent system is required for the dissolution process of metal chalcogenide bulk materials.

4.1.2 Fundamental mechanism of dimensional reduction

Dimensional reduction is proposed by Tulsky and Long to address the dissolve and reform process of inorganic materials, especially metal chalcogenide.[79] The term “dimensional

reduction" is borrowed from an analytical geometry concept: to use a lower dimensional space to describe a higher dimensional space. Figure 4-1 shows a general meaning dimensional reduction. Here in material science, it refers to the process of dismantling the extended metal-anion (M-X) framework of a parent compound MX_a upon reaction with an ionic reagent A_bX, to form a new compound $A_{nb}MX_{a+n}$. In the solid phase, the more electropositive cations A (Li^+, Na^+, K^+, NH_4^+, etc.) form the ionic bonds with the X anions, while exist as dissociated cations in solution. The introduced anions X (for chalcogenides, X = S, Se, or Te) terminate connections between metal centers in the structure, yielding a less tightly connected or lower dimensional framework, which may locally retain aspects of the characteristic metal coordination and polyhedron connectivity of the original parent structure. For each additional A_bX unit added to the parent structure, additional M-X-M metal bond linkages are broken, and the effective dimensionality of the MX_{a+n} framework is progressively reduced. Figure 4-2 shows the generic reaction formula of the dimensional reduction.

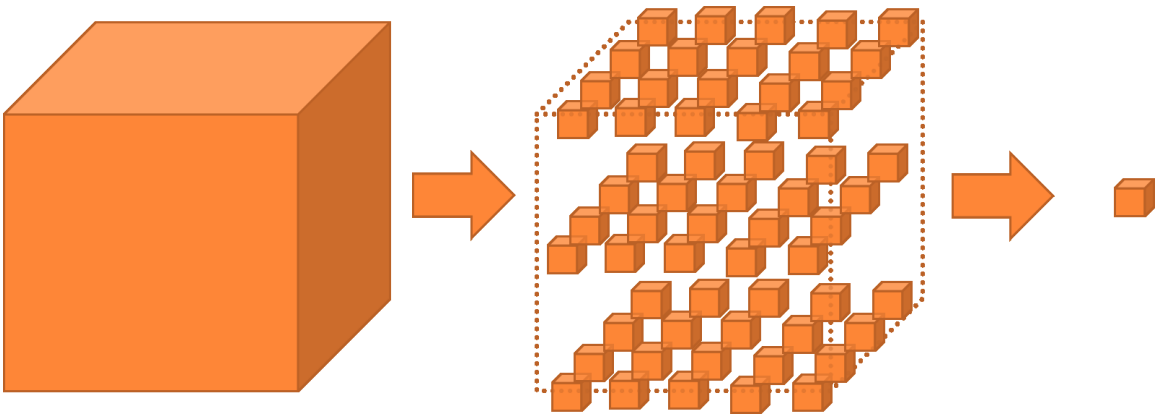

Figure 4-1 A general meaning of dimensional reduction

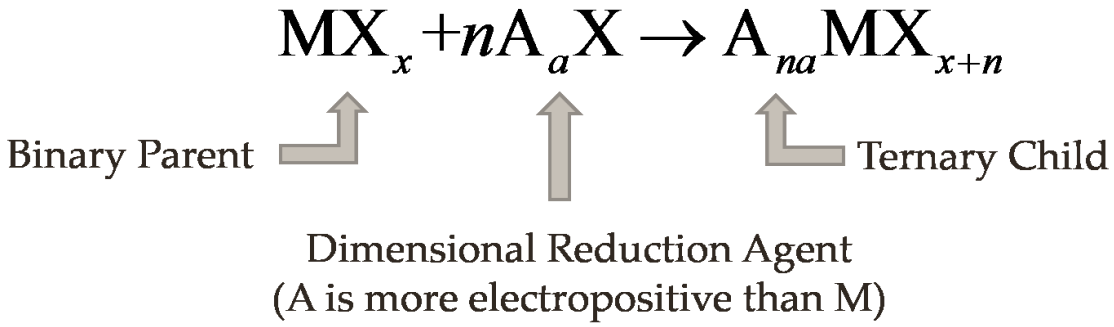

Figure 4-2 The terms definitions in the dimensional reduction

To demonstrate this process, a series of compounds are developed from the interaction between $SnSe_2$ and K_2Se, including $K_4Sn_3Se_8$ (n = 2/3),[80] K_2SnSe_3 (n = 1), $K_6Sn_2Se_7$ (n = 1.5),[80] and K_4SnSe_4 (n = 2),[81] which exhibit varying degrees of condensation among $SnSe_4$ tetrahedral. As a result of reducing the extended 3- dimensional MX_a structure into more isolated MX_{a+n} ionic parts, often the solubility increases with increasing n, thereby enabling the preparation of reasonably concentrated $A_{nb}MX_{a+n}$ solutions by a relatively higher concentration A_aX.

4.1.3 From solution back to the thin film

Once the homogeneous solution of $A_{nb}MX_{a+n}$ is obtained, the next step is to transfer the ions in the solution back to solid phase MX_x. Chalcogen-based MX_{a+n} often has a poor thermal stability and will thermal decompose or hydrolyze at high temperature and release gas phase X or H_2X gas. On the other hand, the high electropositive cations A can be NH_4^+ or $N_2H_5^+$ which also will release gaseous decomposition product at high temperature.

In the $SnSe_2$ and K_2Se example mentioned above, when the K_2SnSe_3 solution is thermal hydrolyzed at a relatively high temperature, the homogeneous solution phase becomes

three phases: H_2Se is released as gas phase, along the solid phase $SnSe_2$ is deposited on the substrate, leaving K^+ and rest Se^{2-} ions in the solution.

In thin film deposition process, the solution can be coated on the substrate by spin coating, spray pyrolysis, dip coating, ink-jet printing, etc. Two-stage thermal treatment is required to evaporate the residue solvent and to convert the ions back to metal chalcogenides.

4.2 MoS_2 layered metal chalcogenide

4.2.1 Transition metal dichalcogenide

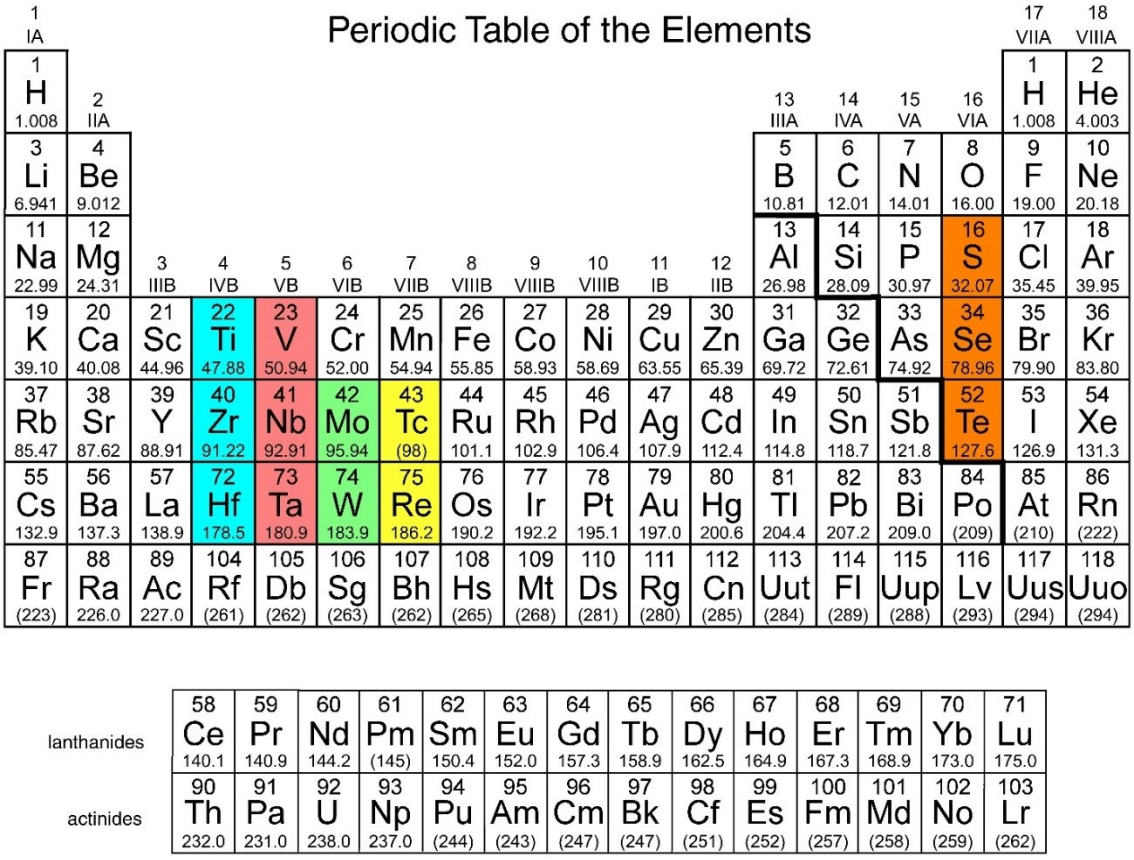

Figure 4-3 Locations for elements forming layer-structured TMDC in the periodic table.

In Chapter 1, the transition metal chalcogenides have been briefly introduced, while here a gourp of more specific dichalcogenides are discussed. Transition metal dichalcogenides (TMDCs or TMDs) share a generalized formula MX_2, where M is a transition metal of Group 4 – 10 (IVB – VIIIB) and X is a chalcogen (S, Se, or Te). When M is located in Group 4 – 7, the MX_2 tends to crystallize in a graphite-like layered structure which leads to strong anisotropy in mechanical, electrical, and thermal properties. Each layer of TMDC is formed by a hexagonally packed layer of metal atoms sandwiched between two layers of chalcogen atoms, in analogy to the hexagonal carbon atoms layer in graphite. Figure 4-3 marks the metal elements which can form this kind layered chalcogenides.

4.2.2 MoS_2 thin film

MoS_2 is one of the most studied layered TMDCs which occurs as the mineral molybdenite in nature. The bulk material is an indirect bandgap semiconductor with a band gap of 1.23 eV, and each layer has a thickness of 6.15Å. Traditionally MoS_2 is used as a dry lubricant film in the range of 0.2~2 μm at up to 350 °C due to its high lubricity from the layered structure and relatively unreactive in oxidizing environments.[82]

Recent research has shown two-dimensional nanomaterials such as graphene can exhibit attractive properties such as extreme high carrier mobility and other remarkable electronic properties connected to the structure.[83] As the graphene analogs, mono-layer or few-layer TMDCs, especially MoS_2, also gain the new attentions after decades research on the bulk materials. MoS_2 has been one of the most promising candidates for microelectronics applications due to its high field-effect mobility and high on/off ratio. Figure 4-3 shows

that there is an explosive increasing after the 2010 Nobel Prize in physics was awarded to the discovery of graphene. The figure data is queried from Thomas Reuters Web of Science.

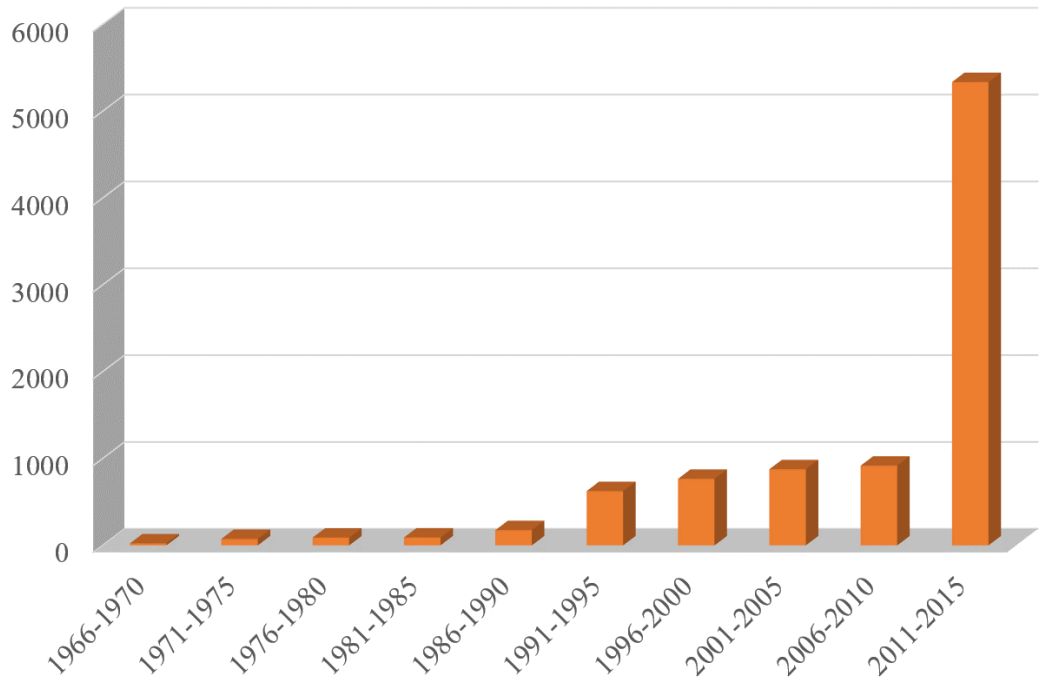

Figure 4-4 The counts of literature with MoS_2 in topic through five decades (1966-2015)

4.2.3 MoS_2 thin film deposition

In order to actually integrate the MoS_2 thin films in field effect thin film transistor, the reliable production of larger area uniform MoS_2 thin films becomes a critical issue. Current methods to prepare the MoS_2 thin layers include Scotch tape assisted micromechanical exfoliation[83, 84], chemical exfoliation[85-87], physical vapor deposition (PVD)[88, 89], chemical vapor deposition (CVD)[90-93], and thiomolybdate-based chemical solution deposition[94-96].

Figure 4-5 shows a MoS_2 flake prepared by mechanical exfoliation. Micromechanical exfoliation is also called Scotch tape method, and it is the first technique to obtain the

graphene samples. It is limited in research only application due to the low throughput and high labor cost. Chemical exfoliation is a quick way to obtain various MoS_2 nanoflakes or nanosheets from bulk molybdenite crystals, but the size of these flakes varies, and there is also a challenge to align these flakes to the desired position for devices fabrication.[97]

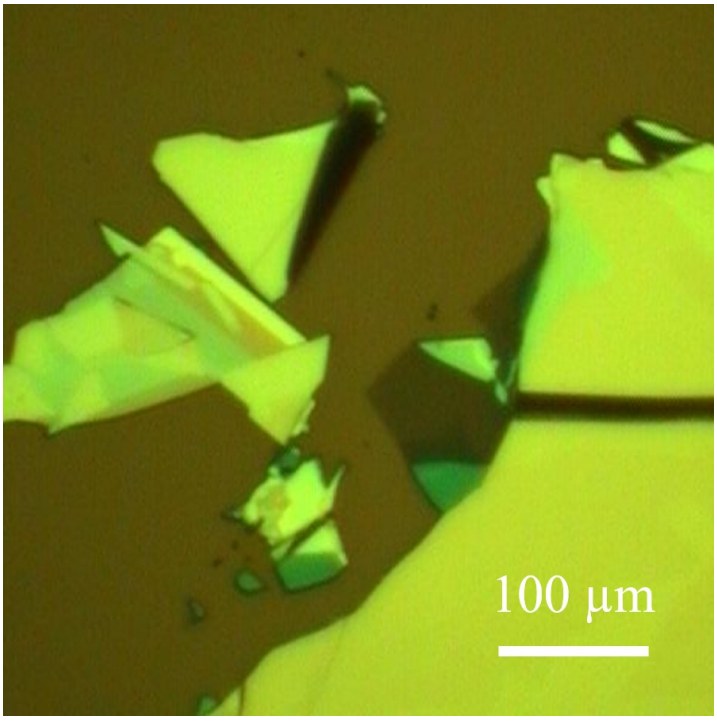

Figure 4-5 MoS_2 flake prepared by Scotch tape method

CVD has been used to synthesize MoS_2 thin-film on reduced graphene oxide (rGO) treated substrate from MoO_3 and elemental sulfur precursors, with a relatively low material utilization.[92] Chemical solution based deposition shows a high material utilization ratio and could achieve a large area uniform MoS_2 thin film, but currently the chemicals are limited in ammonium thiomolybdate or alkyldiammonium thiomolybdate.

4.2.4 MoS_2 thin film deposition via dimensional reduction

Dimensional reduction is an alternative approach for metal chalcogenide thin film deposition.[98] By using hydrazine (N_2H_4) as the dimensional reduction agent, a ultra-thin SnS_2 film with high mobility was deposited for thin film transistor (TFT) device fabrication.[99] Wang et al. also applied the dimensional reduction in the synthesis of the so far champion efficiency $Cu_2ZnSnS_4Se_{4-x}$ solar cell absorber layer.[72]

MoS_2 as a metal dichalcogenide can also be dissolved in N_2H_4 with sulfur presented, which opens a door for the transformation of MoS_2 bulk powder material into the few-layer thin film structure. Figure 4-6 shows the reactions along the whole process of dimensional reduction. The dissolution reaction occurs primarily through this overall reaction:

$$5N_2H_4 + 4S + 2MoS_2 \rightarrow N_2 + 4N_2H_5^+ + 2MoS_4^{2-}$$

After obtaining the solution with MoS_4^{2-} ions, it can be coated on the substrate by any conventional liquid coating method to obtain a wet film. The wet film is dried to evaporate the residue N_2H_4. The following annealing first turns the MoS_4^{2-} into MoS_3 at 200 ºC, then further annealing at 800 ºC will transit MoS_3 into MoS_2. By the assistance of H_2, the MoS_3 to MoS_2 transition can be achieved at 400 ºC which is below the strain point of most common glass and suitable for TFT and other electronics application.

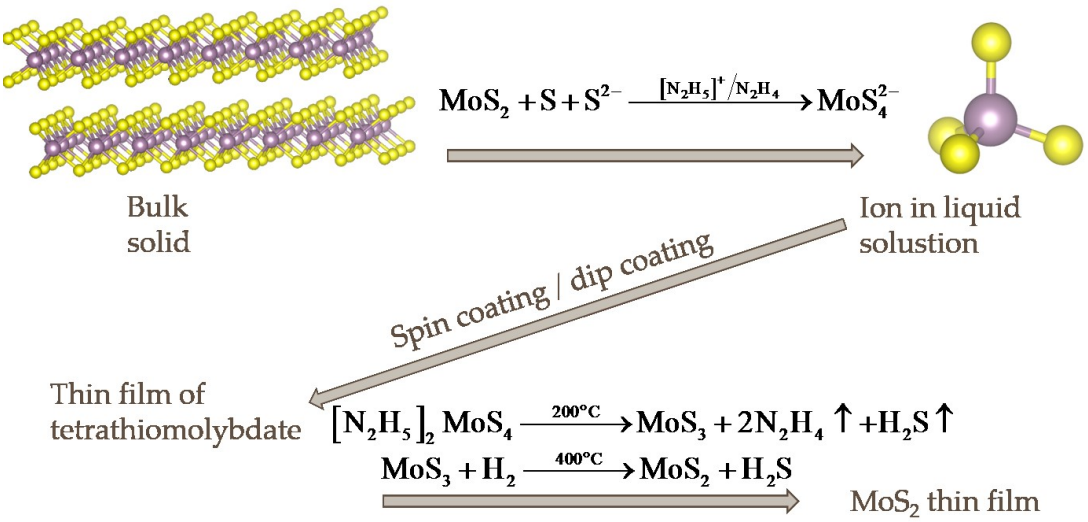

Figure 4-6 The reactions associated with the MoS2 dimensional reduction and thin film deposition

4.3 Microreactor design and analysis

4.3.1 Microreactor

A microreactor is a device with micro-structured features, usually a sub-millimeter dimension, in which chemical reactions are performed.[100] The most common microreactor is microchannel reactor working in a continuous manner. The advantages of microreactors are associated to the small dimensions and internal volumes: High heat transfer rate make microreactors can be heated up or cooled down quickly and handle more extreme exothermal reaction; High mass transfer rate leads to a high product yields than conventional reactor; Very high surface-to-volume ratio increases the reaction rate and provides high catalyst loading rate; The small internal volume also makes the reaction more safer and easy to handle the leakage and other failure.

In a batch reaction of the MoS_2 dimensional reduction, a large amount of heat generated when dissolving the mixture of MoS_2 and sulfur powder into N_2H_4. By applying the

microreactor, it could quickly take away the heat and keep the reaction in a relatively moderate condition. And the dissolution process could be accelerated due to the small diffusion distance inside the microreactor.

Another very important concern is the safety issues brought by the N_2H_4 solvent. N_2H_4 is a very dangerous chemical, highly toxic and easy to explode. Microreactor can keep N_2H_4 in confinement preventing the N_2H_4 exposure to the operating environment.

4.3.2 Microreactor design and fabrication

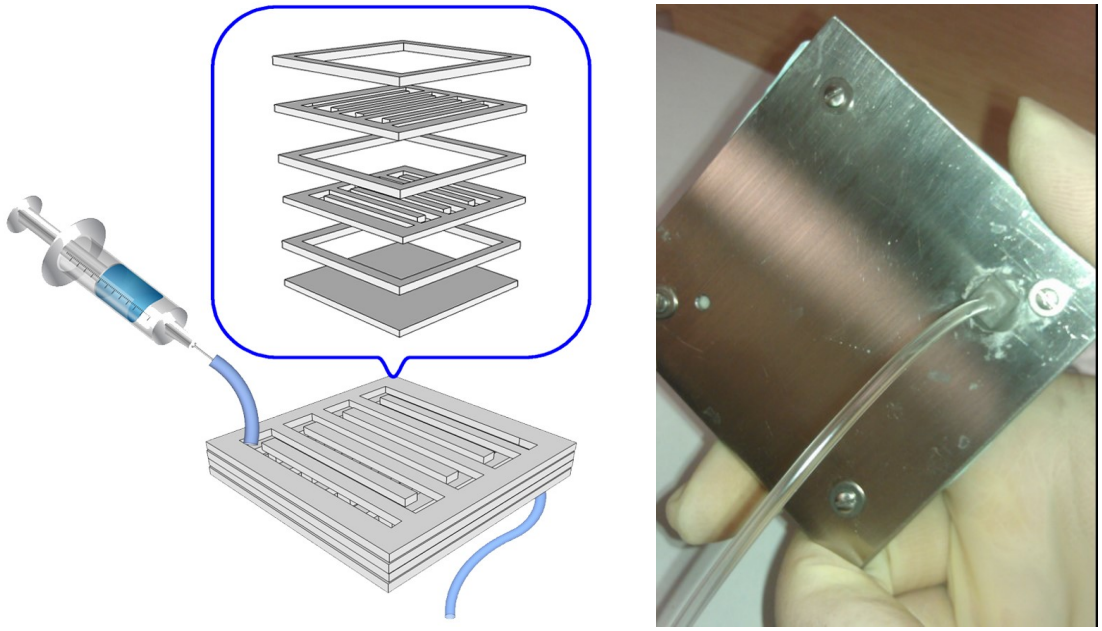

Figure 4-7 Design drawing (left) and the digital photograph (right) of microreactor for MoS_2 dimensional reduction

Figure 4-7 shows the design of microreactor for MoS_2 dimensional reduction. A semi-continuous microreactor was made from 316 stainless steel and polytetrafluoroethylene (PTFE). Two SS316 shells with inlet and outlet drilled clamp the insert PTFE insert plates. There are two kinds laser-cut insert plates stacking alternately to form the internal structure of the microreactor: the square shape O plate is used to load the solid reactants (MoS_2

powder and sulfur powder), and staggered fins plate provides the N_2H_4 solution flowing channel, and works as heat sink. 0.1 μm PTFE filter membrane are used to separate the insert plates.

4.3.2 Thermodynamics estimation for the reaction

As previously mentioned in Section 4.3.1, the MoS_2 dimensional reduction is an exothermal reaction. In order to well understand the microreactor behavior, the heat coming from the overall reaction $5N_2H_4 + 4S + 2MoS_2 \rightarrow N_2 + 4N_2H_5^+ + 2MoS_4^{2-}$ is a required thermodynamics data. Unfortunately, there is no enough thermodynamics reference data for this N_2H_4 involved reaction. But since N_2H_4 is an analogue to NH_3, here a series of estimating calculation is done to get a basic idea of the enthalpy changing during the dimensional reduction process.

Table 4-1 The calculated formation enthalpy data

Ion	**Basic set**	**Calculated formation enthalpy (kJ·mol^{-1})**	**Literature Reference (kJ·mol^{-1})**
NH_4^+	DFT/6-31G	142.7	132.8[101]
$N_2H_5^+$	DFT/6-31G	190.2	182.7[102]
MoS_4^{2-}	DFT/LANL2DZ	45.03	

Table 4-1 shows the formation enthalpy data from both references and Gaussian 03w calculation.

$$\Delta H_f\left(\left(\mathrm{NH_4}\right)_2\mathrm{MoS_4}\right)=-\Delta H_f\left(\mathrm{NH_4^+}\right)-\Delta H_f\left(\mathrm{MoS_4^{2-}}\right)-\Delta H_L\left(\left(\mathrm{NH_4}\right)_2\mathrm{MoS_4}\right)$$

$$\Delta H_f\left(\left(\mathrm{N_2H_5}\right)_2\mathrm{MoS_4}\right)=-\Delta H_f\left(\mathrm{N_2H_5^+}\right)-\Delta H_f\left(\mathrm{MoS_4^{2-}}\right)-\Delta H_L\left(\left(\mathrm{N_2H_5}\right)_2\mathrm{MoS_4}\right)$$

Based on calculated results: $\Delta H_L\left(\left(\mathrm{NH_4}\right)_2\mathrm{MoS_4}\right)=-774\ \mathrm{kJ\cdot mol^{-1}}$

Lattice energy can be roughly estimated as:

$$V=-\frac{e^2}{4\pi\varepsilon_0}\cdot\frac{q_1q_2}{r}\cdot N_\mathrm{A}$$

$V\left(\left(\mathrm{NH_4}\right)_2\mathrm{MoS_4}\right)$ = - $(1.6\times10^{-19})^2\times 8.99\times10^9\times 2 / 372\times10^{-12}\times 6.02\times10^{23}$ = 729 $\mathrm{kJ\cdot mol^{-1}}$

$r_{(\mathrm{NH_4})_2\mathrm{MoS_4}}\approx 372$ pm, $r_{(\mathrm{N_2H_5})_2\mathrm{MoS_4}}\approx 384$ pm

$V\left(\left(\mathrm{N_2H_5}\right)_2\mathrm{MoS_4}\right)$= -774 $\mathrm{kJ\cdot mol^{-1}}\times$ 372/384 = -722 $\mathrm{kJ\cdot mol^{-1}}$

$\therefore \Delta H_f\left(\left(\mathrm{N_2H_5}\right)_2\mathrm{MoS_4}\right)=-190.2-45.03-\left(-722\right)=487\ \mathrm{kJ\cdot mol^{-1}}$

The overall reaction enthalpy is $\Delta_\mathrm{r}H_\mathrm{m}^\theta=-675\,\mathrm{kJ/mol}$

4.3.3 COMSOL simulation of the heat transfer in the microreactor

With the thermal data of the dimensional reduction process, we can do the simulation for the microreactor design verification and optimization.

COMSOL Multiphysics is used to do the heat transfer and reaction finite element analysis. As long as the precursors loaded in the microreactor are not depleted, the dimensional reduction reaction is considered as a constant heat source. To optimize the fins on the insert

plate, different designs are imported into COMSOL. Figure 4-8 shows the design with 1, 8, and 16 fins. And Figure 4-9 shows the cross-sectional temperature profile of 1,8, and 16 fins design.

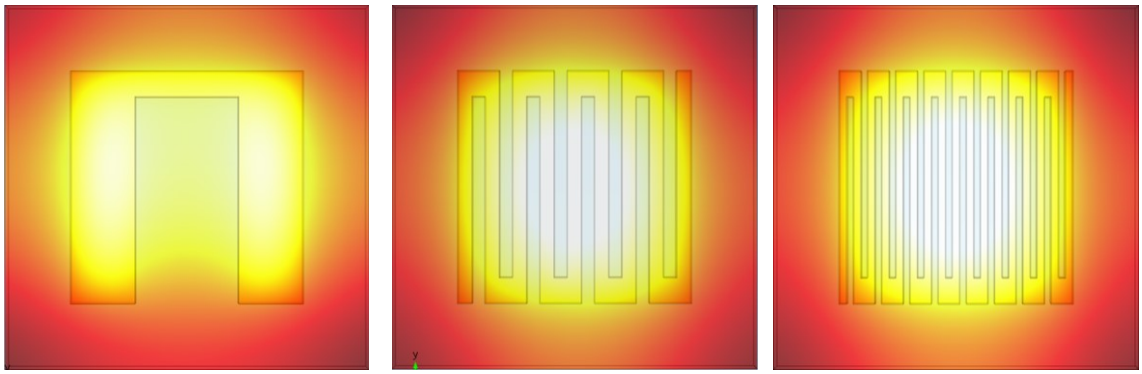

Figure 4-8 Temperature profile of the microreactor insert plate

The simulation results prove that the more heat sink fins in the microreactor, the lower surface temperature can be achieved. But on the other hand, the fabrication cost of the microreactor will also increase along with the number of fins. In our actual microreactor, 8 fins design is used.

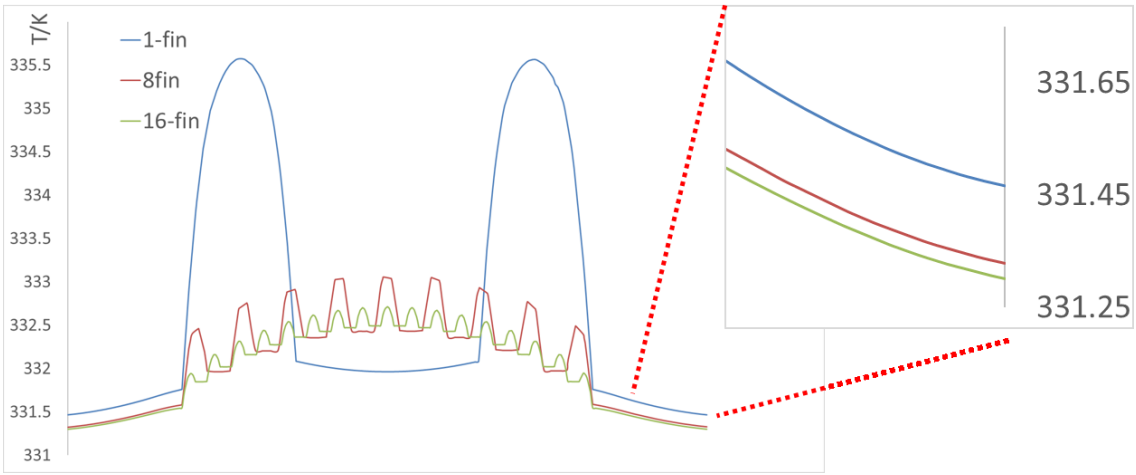

Figure 4-9 Temperature profile of the microreactor insert plate

4.4 MoS_2 thin film deposition and characterization

4.4.1 MoS_2 thin film deposition

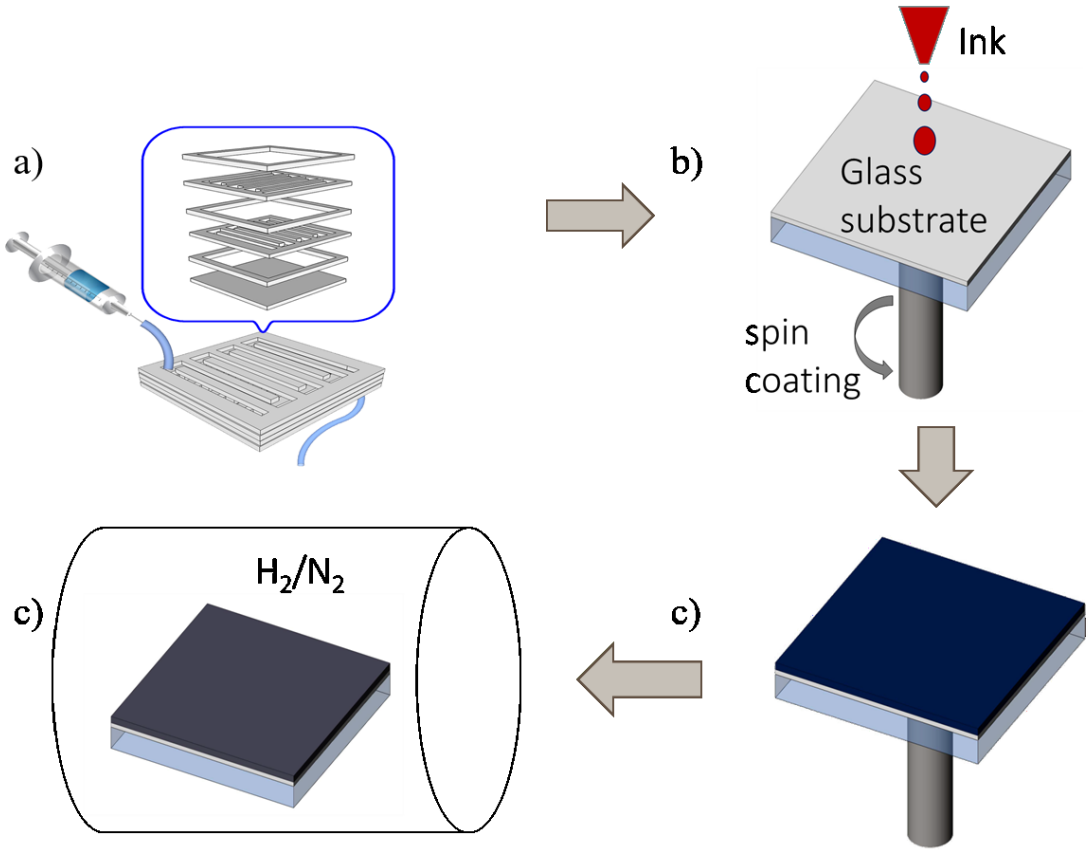

Figure 4-10 Schematic of MoS_2 deposition steps

Figure 4-10 shows the steps of the MoS2 dimensional reduction and thin film deposition. 0.320 g MoS_2 bulk powder and 0.160 g sulfur powder were mixed and loaded into a microreactor chamber, N_2H_4 was injected into the microreactor by a syringe pump (Figure 4-10a). The product solution from the outlet of the micro-reactor was collected and used for spin-coating on both glass and silicon substrates (Figure 4-10b) for 1, 5, and 20 layers. The film was then heated at 200 °C to remove the exceed N_2H_4 solvent and transform to a solid thin film (Figure 4-10c). After the second annealing at 400 °C with 10% H_2 in N_2 (1

atm) for 40 minutes (with extra ramping time at 20 °C/min), the film was converted into final product: MoS_2 (Figure 4-10d).

4.4.2 XPS analysis for chemistry

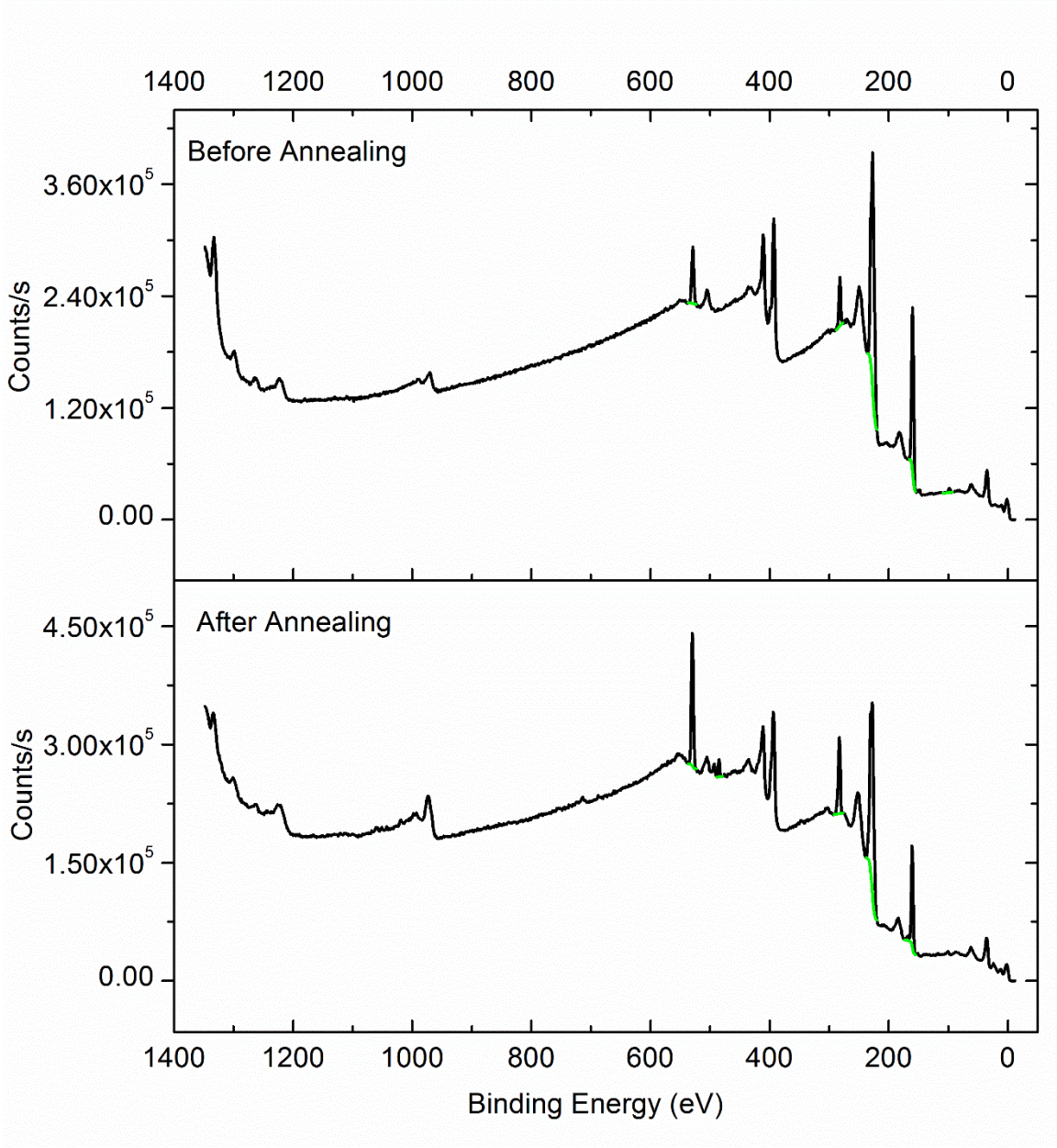

Figure 4-11 XPS survey scan of MoS_2 sample before and after annealing

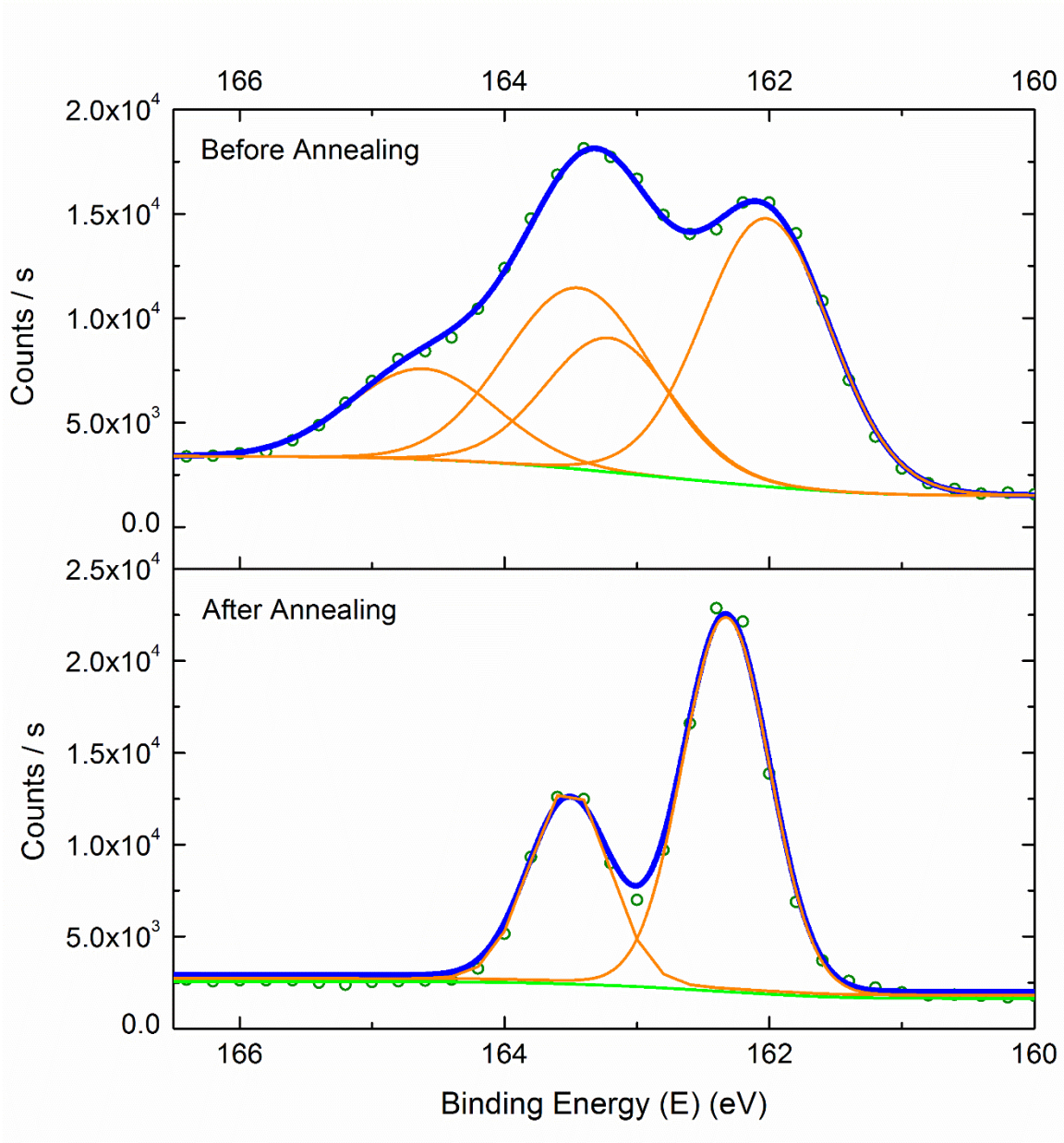

Figure 4-12. XPS core level spectra of S 2p

To study the chemistry behind the process, Xay photoelectron spectroscopy (XPS) is used to study the ink film on the silicon wafer before and after annealing. The survey scan is shown in Figure 4-11, and the adventitious C1s is used as charge reference . In Figure 4-12, before annealing, the S2p peaks show there are two components with the $2p_{1/2}$-$2p_{3/2}$

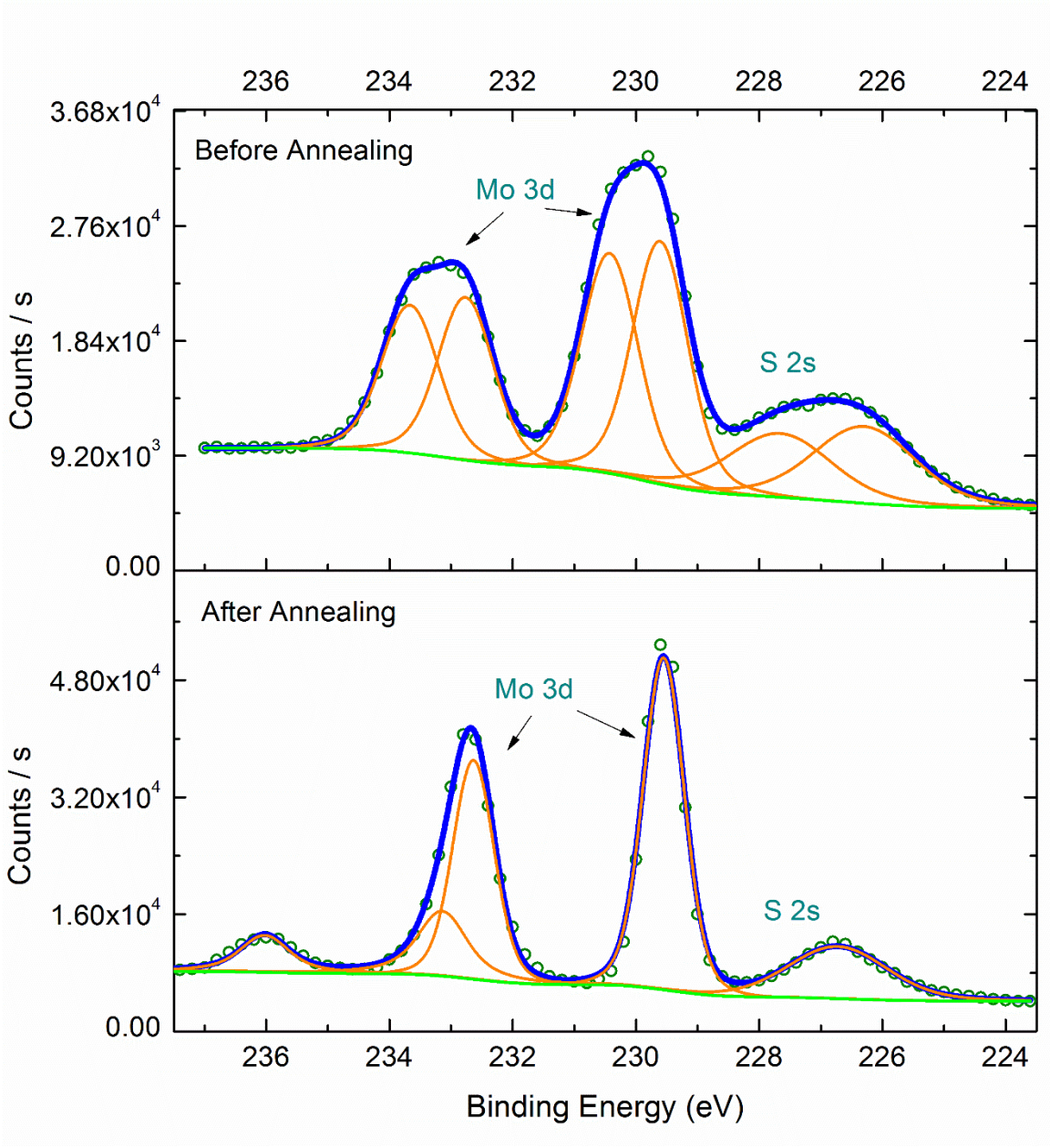

Figure 4-13 XPS core level spectra of Mo 3d

pairs located at 164.6-163.4 eV and 163.2-162.0 eV respectively, which indicates there are both 0 state sulfur from the precursor and -2 sulfur from thiomolybdate. After annealing, all the S has been converted into MoS_2, with $S2p_{1/2}$-$2p_{3/2}$ at 163.6-162.2 eV. Figure 4-13 shows the Mo 3d peaks before and after annealing. Before annealing the Mo $3d_{3/2}$ and $3d_{5/2}$

can be fit to two groups of curves: 233.5-230.5 eV presenting Mo (VI) in MoS_3/MoS_4^{2-} and 232.7-229.2 eV presenting Mo (IV) in MoS_2, and only Mo (IV) in MoS_2 exists after annealing. As a surface sensitive analysis technique, XPS also observes the surface oxidation of the MoS_2 thin film, which shows the 236.0 eV Mo $3d_{3/2}$ peak for Mo (VI) in MoO_3.[103, 104]

4.4.3 Annealing temperature study

Raman spectroscopy is used to compare the films under different annealing temperatures as Figure 4-14. When the annealing temperature reaches 400 °C, the MoS_2 characteristic peaks E_{2g}^1 and A_{1g} show up. Annealing with further higher temperature does not show different from 400 °C annealing.

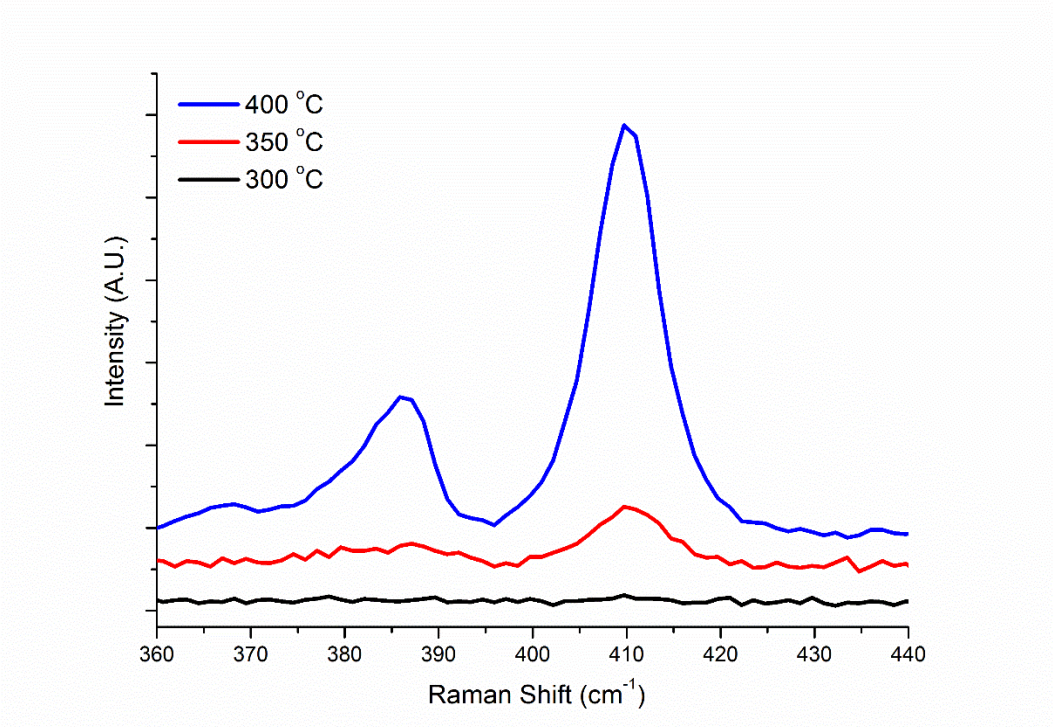

Figure 4-14 Raman spectra of samples with 300 °C, 350 °C, and 400°C annealing respectively

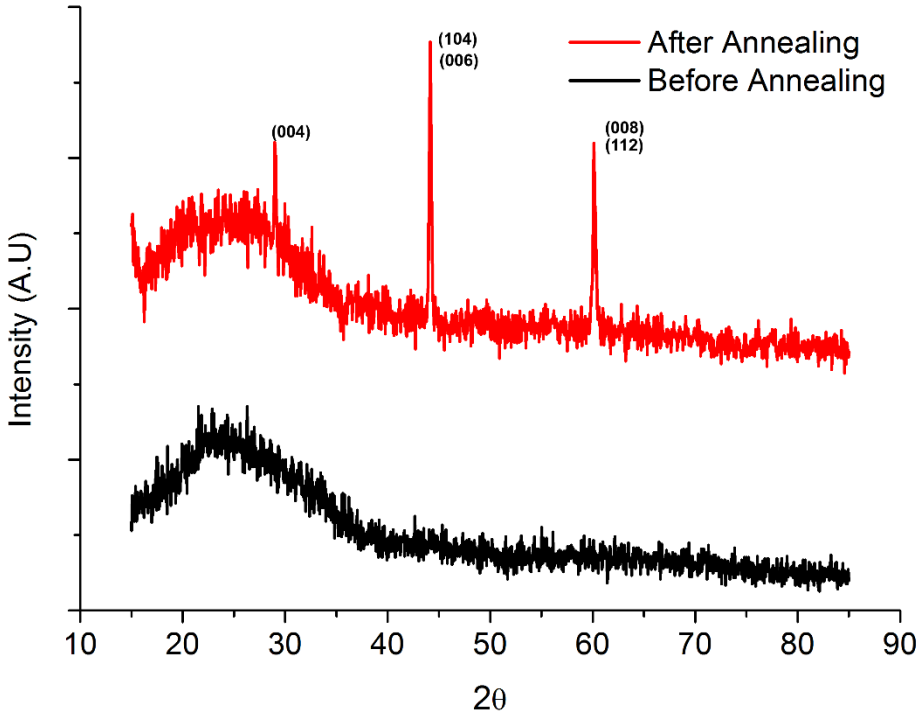

Figure 4-15 XRD pattern of the single spincoating thin film before and after H_2 annealing

X-ray diffraction pattern of the thin film on the glass substrate before and after annealing is shown in Figure 4-15. Before annealing, there are no diffraction peaks other than glass substrate background. After annealing, low intense but sharp peaks of MoS_2 are observed.

4.4.4 Study on the thickness of MoS_2

The thickness of the thin film is controlled by the times of spin coating. The thickness is checked by ZeScope optical profilometer and SEM cross sectional image. The challenge for ZeScope is besides preparing the valley-peak structure on the studied material film, the substrate with a surface fully covered with the same material as the height reference is preferred. The substrate can be pre-coated with MoS_2 by the same MoS_2 in N_2H_4 solution ink, here another method based on the $(NH_4)_2MoS_4$ ink is used to cover the substrate with

MoS_2. Then the MoS_2 on MoS_2 structure is measured by optical profilometer. Figure 4-16 left shows the CG-rebuilt surface of MoS_2 line. The thickness for single time spin coating is estimated as 20.2±4.1 nm. With more layers coated, it is possible to check the thickness by SEM images. The cross-sectional view in Figure 4-16 right shows the thickness is ~300 nm for a 20-layer spin-coated film.

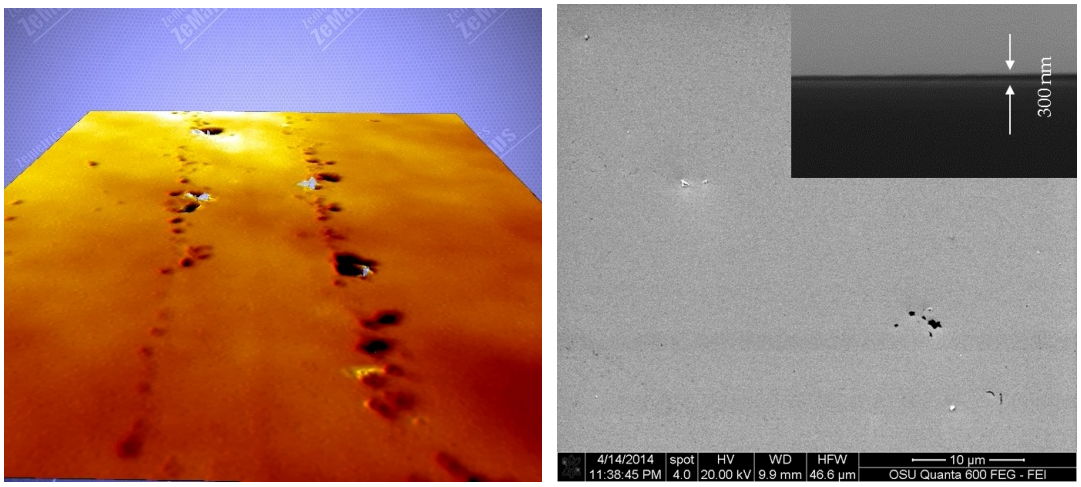

Figure 4-16 Optical profilometer image of 1-layer spin coated MoS_2 (left) and SEM images of both top view and side view of a 20-layer coated MoS_2 (right).

The non-linear relationship between the thickness and spin coating layers is due to the partial dissolution of the previously coated layer during the spin coating. The annealed films with 1-, 5- and 20- times coating are characterized by both XRD and Raman spectroscopy.

XRD results in Figure 4-17 shows the XRD pattern associated with different thickness. The thinner MoS_2 film has a layered orientation parallel to the (002) face, with the thickness increasing, more peaks come out, and eventually the thick film has the same pattern as bulk material. It is due to the orientation of small MoS_2 flakes are confined by the thickness of

the whole film. With the increasing of the thickness, the possible orientations increase, as shown in Figure 4-18.

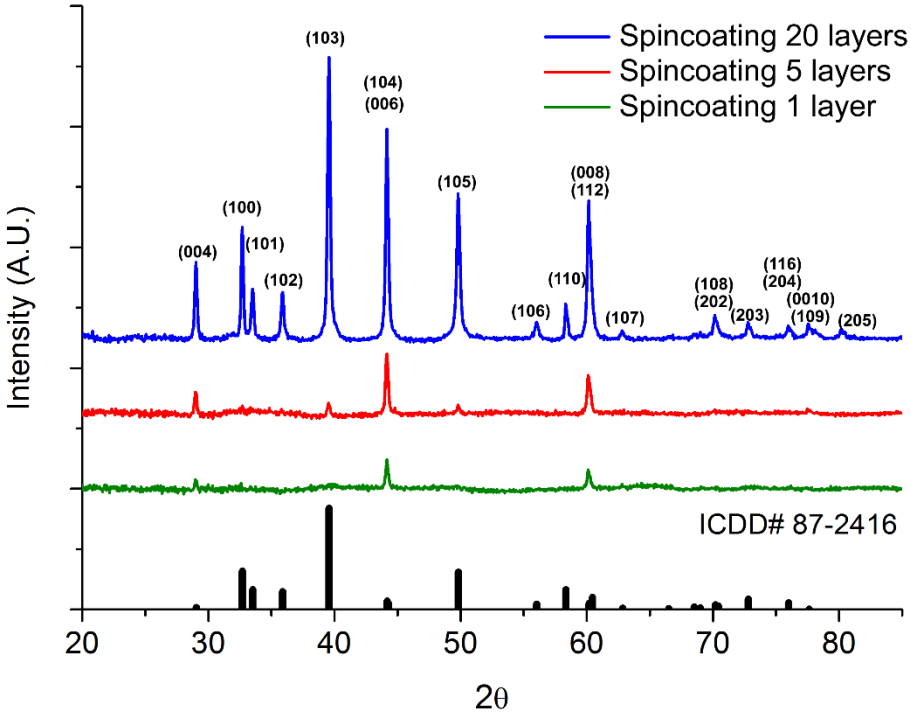

Figure 4-17 XRD pattern of different annealed thin films of 1, 5, and 20 times spincoating

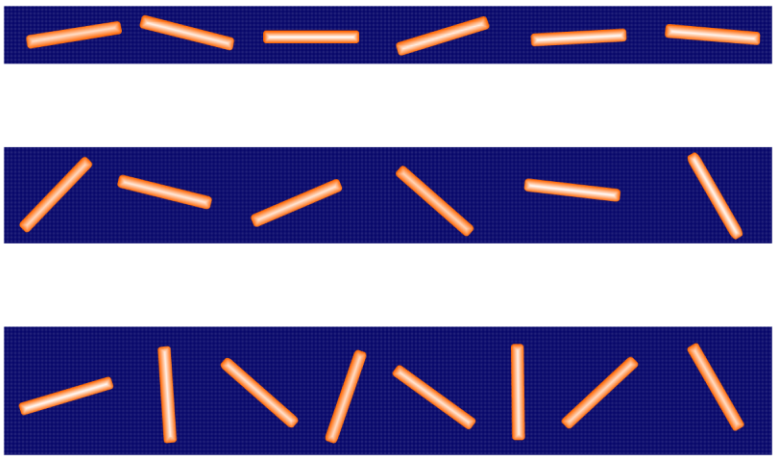

Figure 4-18 Polycrystalline MoS_2 orientations change with the thickness

Raman spectra shown in Figure 4-19 indicate along the thickness increasing, the Raman shift between E_{2g}^1 and A_{1g} peaks increases.

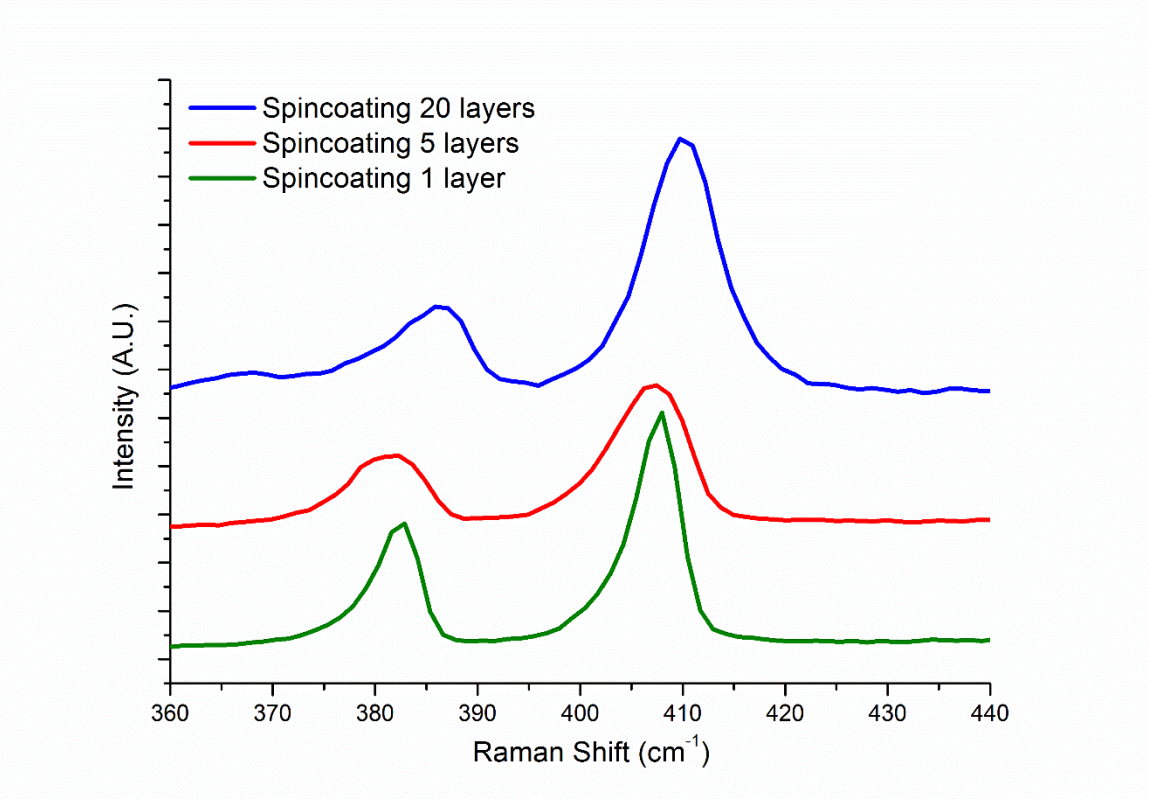

Figure 4-19 Raman peaks shift along the thickness change

4.4.5 Electronic performance of MoS_2

Hall effect measurement shows the mobility of 1-layer spin-coated MoS_2 thin film is 0.435 $cm^2V^{-1}s^{-1}$. A coplanar bottom-gate thin film transistor device had been fabricated based on this MoS_2 thin film as shown in Figure 4-20 left. The channel width is ~50 μm. The DC source-drain current-voltage behavior of the TFT was characterized using a Cascade MPS 150 probe station, the *I-V* curves were shown in Figure 4-20 right. The I_{DS} increases as V_{DS} increases at a positive V_{GS} gate bias, indicating that the semiconductor channel is n-type.

The I_{DS} could not saturate within the measured V_{DS} range, which makes the device might not be able to be accurately identified as a TFT.

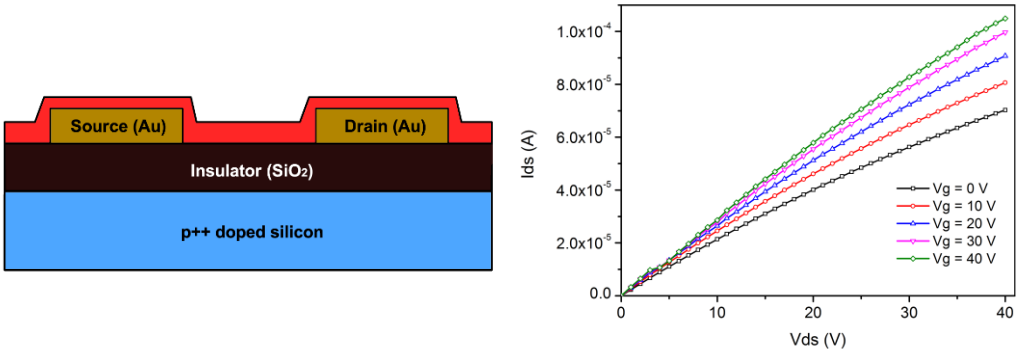

Figure 4-20 Schematic of MoS_2 TFT (left) and the I-V performance of the device (right)

4.5 Chapter summary

Dimensional reduction is a chemical route to dissolve metal chalcogenides, and the solution can be converted back to chalcogenides thin films. MoS_2 as a promising semiconductor material has been successfully dissolved in the N_2H_4, and a MoS_2 thin film is obtained after thermal treatment. To solve the dramatic exothermal problem, a microchannel-based microreactor is used. Finite element analysis shows the reactor surface temperature has a reversed relationship to the fin number of the microreactor insert plates.

CHAPTER 5 Conclusion

5.1 Review of the three routes

5.1.1 Metal oxide to metal chalcogenide

Metal oxide thin film is prepared by sol-gel process. Then the oxide thin film is chalcogenized by an annealing process with both chalcogen and hydrogen. By the same route, Wang et al. reported a CIGS device with efficiency of 8.01% with more optimization.[105] Although metal carboxylate salt is used in Chapter 2 as the precursor for sol-gel process, metal nitrate can also achieve the same metal oxide thin film after annealing. Fang reported the deposition of FeS_2 and Fe_2GeS_4 thin films for thin film transistor by sulfurization of the Fe_2O_3 and Fe_2O_3-GeO_2 thin film.[106]

Besides the low precursor cost and more air-stable, the carboxylate precursor also produces fewer cracks than alkoxide precursor. Gaucher et al. proposed that the if the reticulation of the sol occurs before the evaporation of the solvent, the shrinkage during the evaporation will cause the crack, while if the solvent evaporation is before the reticulation as in the carboxylate precursor, the cracks can be minimized.[107] Figure 5-1 shows a schematic of the sol-gel process based on these two kinds of precursors. For TFT semiconductor application, it is easy to obtain a crack-free oxide and chalcogenide film with less than 150 nm thickness from carboxylate precursor. For CIGS thin film PV device, the thickness is 1~2.5 μm, it is hard to obtain the crack-free thin film due to the accumulation of thermal expansion caused by strain or stress. From what we observed, the further selenization annealing partially helps the healing of this kind of crack.

The thin film chalcogenization occurs in a solid and gas phase reaction. It is also possible to run a similar process in solid and liquid phase to chalcogenize the metal oxide nanoparticles into metal chalcogenide nanoparticles. Pang & Zeng reported prepared CuSe nanoparticles from a well-dispersed CuO_2 nanosphere suspension by adding Se powder and sodium borohydride ($NaBH_4$).[108] $NaBH_4$ in solution is an analogy to H_2 in the gas phase.

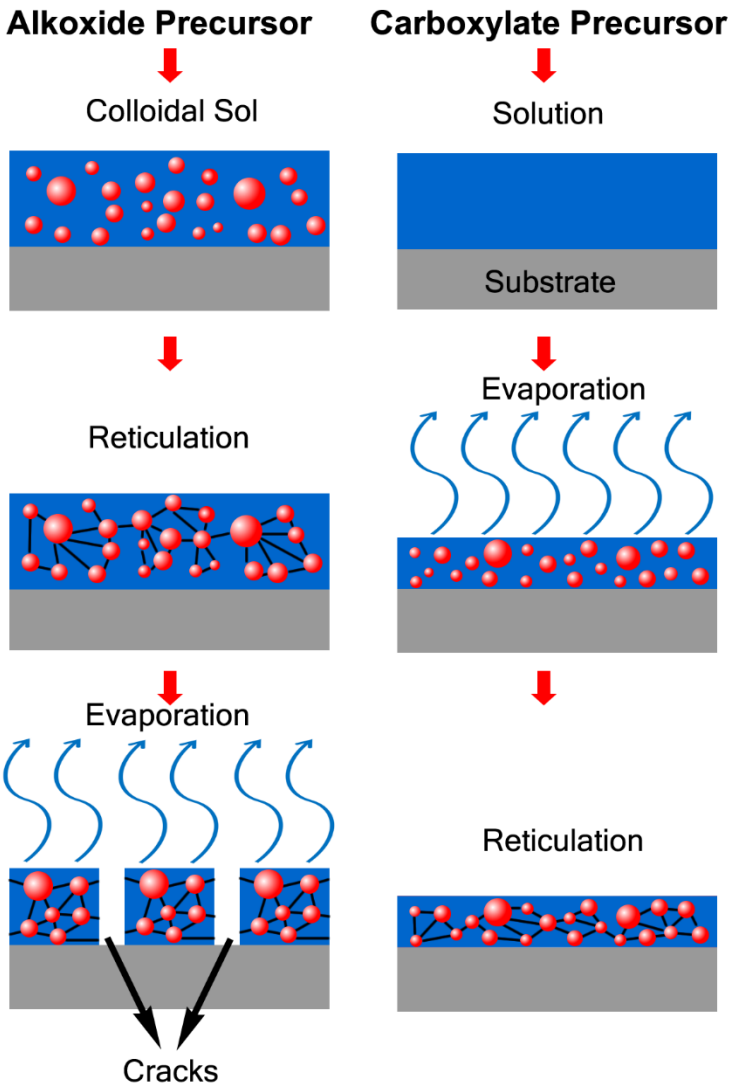

Figure 5-1 The comparison of alkoxide precursor (left) and carboxylate precursor (right) during the sol-gel process.

5.1.2 Electrodeposited metal to metal chalcogenide

Metal thin film is deposited by electroplating from bulk metal. Then the metal thin film is chalcogenized to metal chalcogenide. For ternary and quaternary chalcogenide, the layer-by-layer electroplating is a low-cost choice comparing to one-pot electroplating. Another approaching is electroless plating which also has a half-century history and can deposit both alloy and composite in a single electrolyte bath.[109] The setup cost for electroless plating is relatively lower than electroplating due to the elimination of electrical part, but the operation cost is higher since the bath is more complex and need to replace periodically while electroplating only needs to replenish the additives.

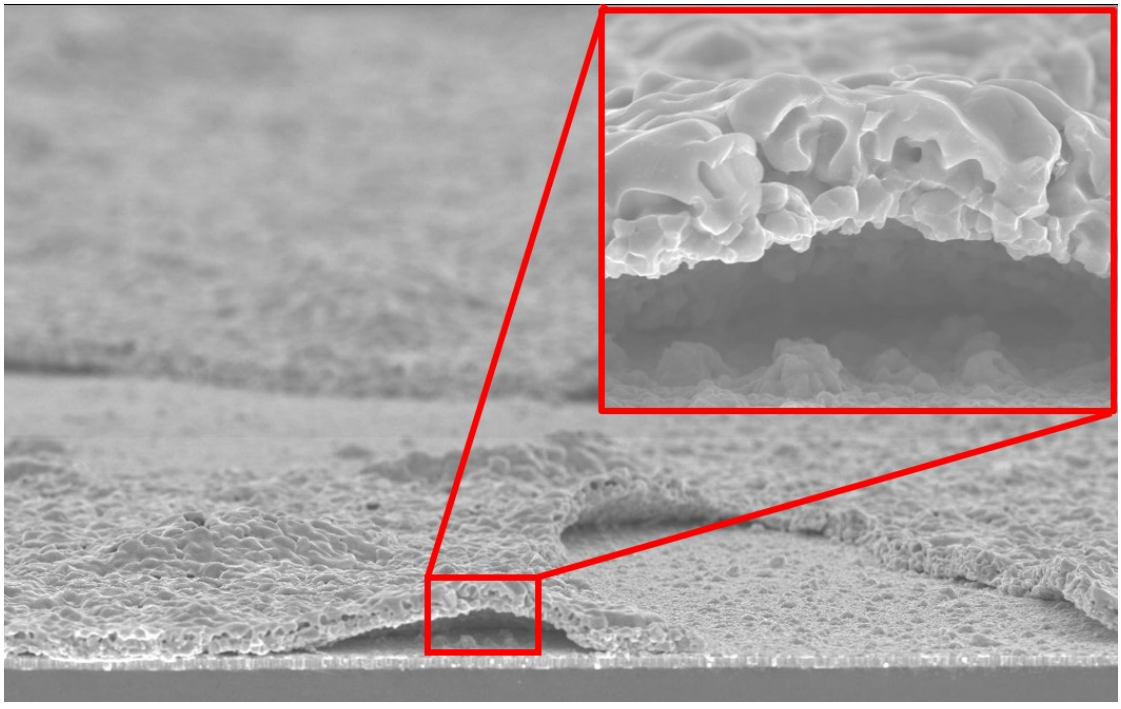

Figure 5-2 Blisters cause the peel-off on the CZTS thin film surface after sulfurization

Volume increasing is associated with the chalcogenization process from a dense metal film. Figure 5-2 shows an example of bumping after a quick ramping sulfurization of Cu-Sn-Zn

metal stack. It could be minimized by a relatively slow ramping which can give a longer time for the stress to release. At the same time, the liquid phase CuS at above 500 ºC can carry the increase perpendicular to the substrate surface.

5.1.3 Hydrazine dimensional reduction

Some powder metal chalcogenide can be dissolved into hydrazine to form an ionic solution. After the evaporation of the hydrazine solvent and further annealing, the solution wet film is transformed back to metal chalcogenide solid thin film. This process has been successfully applied to $Sn(S,Se)_2$,[99] Cu_2S, In_2Se_3, Ga_2Se_3, etc.[110] While it is reported Zn(S,Se) can only form a nanoparticle form of $Zn(S,Se)N_2H_4$.[68] Webber & Brutchey proposed a diamine-dithiol solvent mixture for V_2VI_3 chalcogenides dissolution,[111] and the diamine-dithiol solvent has been used for $Cu_2(S,Se)$, Sn(S,Se), and metallic Cu, Zn, and Sn.[112] The low solubility of Zn(S,Se) in both hydrazine and diamine-dithiol could be related to the tetrahedral structure in either zinc blende or wurtzite crystal structure.

Similar to the MOD sol-gel process, a crack-free chalcogenide thin film can be achieved by control the order and rate of the solvent evaporation and metal-chalcogen-metal reticulation.

Both hydrazine and diamine-dithiol solvents need to be processed in a confined environment due to the toxicity and potential exploding danger. Microreactor is a possible solution for minimizing the exposure to these dangerous solvents, and a switchable cartridge loaded with the chalcogenide powder could improve the efficiency of this semi-continuous flow reaction.

APPENDIX A. Instruments used in this work

TGA:	TA Instruments SDT-Q600 Simultaneous TGA/DSC
SEM:	FEI Quanta 3D dual beam SEM/FIB
	FEI Quanta 600F environmental SEM
	JEOL JSM-6500F SEM
TEM:	FEI Titan 80-200 TEM/STEM with ChemiSTEM
ICP-OES:	Perkin-Elmer Optima 3000 ICP-OES
EPMA:	Cameca SX-100 EPMA
XPS:	Thermo Scientific ESCALab 250
XRD:	Bruker D8 Discover
	PANalytical X'Pert
Raman:	WITec Alpha300RA
PV Efficiency:	Newport Oriel IV Test Station w/ Keithley 2420 SMU
QE:	Tau Science FlashQE
I-V:	Keysight E5260 Analyzer

I would like to express the acknowledgement to Ms. Teresa Sawyer, Ms. Han Ling Chan, Dr. Yi Liu and Dr. Peter A. Eschbach for their help in EM facility, Dr. Frank J. Tepley III for his help in EMPA, Dr. Stephen L. Golledge for his help in XPS analysis, as well as Dr. Jack T. Rundel and Mr. Neill Thornton for their help in numerous process facilities.

APPENDIX B. Glossary

ALD: Atomic Layer Deposition 8

AP-CVD: Atmospheric Pressure CVD 10

a-Si: Amorphous Silicon 25

AZO: Al-doped ZnO 35

CBD: Chemical Bath Deposition 8, 11, 13, 14, 34

CG: Computer Graphics 86

CSD: Chemical Solution Deposition 15, 16

c-Si: Crystalline Silicon 24, 25, 40

CVD: Chemical Vapor Deposition 8, 10, 72, 73

D.I. water: Deionized water 35

DC: Direct Current 34, 37, 47, 88

EDS: Energy-dispersive X-ray Spectroscopy 55, 57

EPMA: Electron Probe Microanalysis 32, 94

EQE: External Quantum Efficiency 38

FF: Fill-factor 37

ICP-OES: Inductively Coupled Plasma Optical Emission Spectrometry 51, 52, 94

IQE: Internal Quantum Efficiency 38

IR: Infrared 4

I-V: Current-Voltage 37

i-ZnO: Intrinsic ZnO 35

LCD: Liquid Crystal Display 22

MASD: Micro-reactor Assisted Solution Deposition 13

MBE: Molecular Beam Epitaxy 8, 9

MEE: Migration-enhanced Epitaxy 28

MOCVD: Metalorganic Chemical Vapor Deposition 8, 10

MOD: Metallo-organic Decomposition 16, 93

MPS: sodium 3-mercapto-1-propanesulfonate 52, 53

PCD: Photochemical Deposition 13

PECVD: Plasma-enhanced CVD 8

PEG: Polyethylene Glycol 47

PLD: Pulsed Laser Deposition 8, 9

PTFE: Polytetrafluoroethylene 76

PV: Photovoltaic 24, 27, 28, 33, 37, 40, 41, 42, 43, 44, 47, 64, 65, 90, 94

Reference

1. M. Fleischer, The Abundance and Distribution of the Chemical Elements in the Earth's Crust, *J. Chem. Educ.*, 1954, **31**, 446-455.

2. in *CRC Handbook of Chemistry and Physics*, ed. W. M. Haynes, CRC Press/Taylor & Francis, Boca Raton, FL, 97th Edition (Internet Version 2017) edn., 2017.

3. L. C. Allen, Electronegativity Is the Average One-Electron Energy of the Valence-Shell Electrons in Ground-State Free Atoms, *J. Am. Chem. Soc.*, 1989, **111**, 9003–9014.

4. Y. T. Oganessian, V. K. Utyonkov, Y. V. Lobanov, F. S. Abdullin, A. N. Polyakov, I. V. Shirokovsky, Y. S. Tsyganov, G. G. Gulbekian, S. L. Bogomolov, B. N. Gikal, A. N. Mezentsev, S. Iliev, V. G. Subbotin, A. M. Sukhov, O. V. Ivanov, G. V. Buklanov, K. Subotic, M. G. Itkis, K. J. Moody, J. F. Wild, N. J. Stoyer, M. A. Stoyer, R. W. Lougheed, C. A. Laue, Y. A. Karelin and A. N. Tatarinov, Observation of the Decay of ^{292}116, *Phys. Rev. C*, 2000, **63**, 011301.

5. M. Akhtar, C. K. Chiang, A. J. Heeger, J. Milliken and A. G. Macdiarmid, Synthesis of Metallic Polythiazyl Halides from Tetrasulfur Tetranitride, *Inorg. Chem.*, 1978, **17**, 1539-1542.

6. F. W. Wise, Lead Salt Quantum Dots: The Limit of Strong Quantum Confinement, *Acc. Chem. Res.*, 2000, **33**, 773-780.

7. P. Y. Feng, X. H. Bu and N. F. Zheng, The Interface Chemistry between Chalcogenide Clusters and Open Framework Chalcogenides, *Acc. Chem. Res.*, 2005, **38**, 293-303.

8. X. S. Fang, T. Y. Zhai, U. K. Gautam, L. Li, L. M. Wu, B. Yoshio and D. Golberg, ZnS Nanostructures: From Synthesis to Applications, *Prog. Mater. Sci.*, 2011, **56**, 175-287.

9. W. W. Yu and X. Peng, Formation of High-Quality CdS and Other II–VI Semiconductor Nanocrystals in Noncoordinating Solvents: Tunable Reactivity of Monomers, *Angew. Chem. Int. Ed.*, 2002, **41**, 2368-2371.

10. L. Isac, A. Duta, A. Kriza, S. Manolache and M. Nanu, Copper Sulfides Obtained by Spray Pyrolysis — Possible Absorbers in Solid-State Solar Cells, *Thin Solid Films*, 2007, **515**, 5755-5758.

11. P. K. Nair, M. T. S. Nair, A. Fernandez and M. Ocampo, Prospects of Chemically Deposited Metal Chalcogenide Thin Films for Solar Control Applications, *J. Phys. D: Appl. Phys.*, 1989, **22**, 829.

12. L. Yu, S. Lany, R. Kykyneshi, V. Jieratum, R. Ravichandran, B. Pelatt, E. Altschul, H. A. S. Platt, J. F. Wager, D. A. Keszler and A. Zunger, Iron Chalcogenide Photovoltaic Absorbers, *Adv. Energy Mater.*, 2011, **1**, 748-753.

13. T. Mang, S. Noll and T. Bartels, in *Ullmann's Encyclopedia of Industrial Chemistry*, Wiley-VCH Verlag GmbH & Co. KGaA, 2000, DOI: 10.1002/14356007.a15_423.pub2.

14. T. Heine, Transition Metal Chalcogenides: Ultrathin Inorganic Materials with Tunable Electronic Properties, *Acc. Chem. Res.*, 2015, **48**, 65-72.

15. S.-Y. Han, B. K. Paul and C.-H. Chang, Nanostructured ZnO as Biomimetic Anti-Reflective Coatings on Textured Silicon Using a Continuous Solution Process, *J. Mater. Chem.*, 2012, **22**, 22906-22912.

16. X. Wu, F. Lai, L. Lin, J. Lv, B. Zhuang, Q. Yan and Z. Huang, Optical Inhomogeneity of ZnS Films Deposited by Thermal Evaporation, *Appl. Surf. Sci.*, 2008, **254**, 6455-6460.

17. J. Britt and C. Ferekides, Thin-Film CdS/CdTe Solar-Cell with 15.8-Percent Efficiency, *Appl. Phys. Lett.*, 1993, **62**, 2851-2852.

18. J. H. Shi, Z. Q. Li, D. W. Zhang, Q. Q. Liu, Z. Sun and S. M. Huang, Fabrication of Cu(In, Ga)Se_2 Thin Films by Sputtering from a Single Quaternary Chalcogenide Target, *Prog. Photovoltaics*, 2011, **19**, 160-164.

19. L. X. Shao, K. H. Chang and H. L. Hwang, Zinc Sulfide Thin Films Deposited by RF Reactive Sputtering for Photovoltaic Applications, *Appl. Surf. Sci.*, 2003, **212**, 305-310.

20. M. McLaughlin, H. F. Sakeek, P. Maguire, W. G. Graham, J. Molloy, T. Morrow, S. Laverty and J. Anderson, Properties of ZnS Thin-Films Prepared by 248-nm Pulsed-Laser Deposition, *Appl. Phys. Lett.*, 1993, **63**, 1865-1867.

21. B. Ullrich, H. Sakai and Y. Segawa, Optoelectronic Properties of Thin Film CdS Formed by Ultraviolet and Infrared Pulsed-Laser Deposition, *Thin Solid Films*, 2001, **385**, 220-224.

22. Q. M. Yang, J. Zhao, M. Guan, C. Liu, L. J. Cui, D. J. Han and Y. P. Zeng, Growth and Annealing of Zinc-Blende CdSe Thin Films on GaAs (001) by Molecular Beam Epitaxy, *Appl. Surf. Sci.*, 2011, **257**, 9038-9043.

23. G. Zhang, H. Qin, J. Teng, J. Guo, Q. Guo, X. Dai, Z. Fang and K. Wu, Quintuple-Layer Epitaxy of Thin Films of Topological Insulator Bi2Se3, *Appl. Phys. Lett.*, 2009, **95**, 053114.

24. N. Berry, M. Cheng, C. L. Perkins, M. Limpinsel, J. C. Hemminger and M. Law, Atmospheric-Pressure Chemical Vapor Deposition of Iron Pyrite Thin Films, *Adv. Energy Mater.*, 2012, **2**, 1124-1135.

25. S. Yamaga, A. Yoshikawa and H. Kasai, Electrical and Optical-Properties of Donor Doped ZnS Films Grown by Low-Pressure MOCVD, *J. Cryst. Growth*, 1988, **86**, 252-256.

26. S. M. Pawar, B. S. Pawar, A. V. Moholkar, D. S. Choi, J. H. Yun, J. H. Moon, S. S. Kolekar and J. H. Kim, Single Step Electrosynthesis of Cu_2ZnSnS_4 (CZTS) Thin Films for Solar Cell Application, *Electrochim. Acta*, 2010, **55**, 4057-4061.

27. W. H. Brock, *Justus Von Liebig: The Chemical Gatekeeper*, Cambridge University Press, Cambridge, 2002.

28. J. Emerson-Reynolds, Xxv.-on the Synthesis of Galena by Means of Thiocarbamide, and the Deposition of Lead Sulphide as a Specular Film, *J. Chem. Soc. Trans.*, 1884, **45**, 162-165.

29. G. Hodes, *Chemical Solution Deposition of Semiconductor Films*, Marcel Dekker, Inc., New York, 2003.

30. Y. W. Su, S. Ramprasad, S. Y. Han, W. Wang, S. O. Ryu, D. R. Palo, B. K. Paul and C. H. Chang, Dense CdS Thin Films on Fluorine-Doped Tin Oxide Coated Glass by High-Rate Microreactor-Assisted Solution Deposition, *Thin Solid Films*, 2013, **532**, 16-21.

31. P. Vas-Umnuay, K. J. Kim and C. H. Chang, Growth Kinetics of Copper Sulfide Thin Films by Photochemical Deposition, *Crystengcomm*, 2016, **18**, 6748-6758.

32. D. Chiu, *Growth, Characterization and Applications of Zinc Sulfide Thin Films by Solution-Based Processes*, Thesis for Ph. D. in Chemical Engineering, Oregon State University, 2016.

33. M. Ebelmen, On the Synthesis of Silica Gels from Alkoxides, *Annales de chimie et de physique*, 1846, **16**, 129.

34. H. Dislich and E. Hussmann, Amorphous and Crystalline Dip Coatings Obtained from Organometallic Solutions: Procedures, Chemical Processes and Products, *Thin Solid Films*, 1981, **77**, 129-140.

35. S. K. Dey, K. D. Budd and D. A. Payne, Thin-Film Ferroelectrics of PZT by Sol-Gel Processing, *IEEE Trans. Ultrason. Ferroelectr. Freq. Control*, 1988, **35**, 80-81.

36. D. H. Lee, Y. J. Chang, G. S. Herman and C. H. Chang, A General Route to Printable High-Mobility Transparent Amorphous Oxide Semiconductors, *Adv. Mater.*, 2007, **19**, 843-847.

37. M. J. Alam and D. C. Cameron, Optical and Electrical Properties of Transparent Conductive ITO Thin Films Deposited by Sol-Gel Process, *Thin Solid Films*, 2000, **377**, 455-459.

38. Z. P. Shao, W. Zhou and Z. H. Zhu, Advanced Synthesis of Materials for Intermediate-Temperature Solid Oxide Fuel Cells, *Prog. Mater. Sci.*, 2012, **57**, 804-874.

39. P. Baraldi, Thermal Behavior of Metal Carboxylates: III-Metal Acetates, *Spectrochim. Acta Mol. Spectrosc.*, 1982, **38**, 51-55.

40. V. K. Kapur, A. Bansal, P. Le and O. I. Asensio, Non-Vacuum Processing of $CuIn_{1-x}Ga_xSe_2$ Solar Cells on Rigid and Flexible Substrates Using Nanoparticle Precursor Inks, *Thin Solid Films*, 2003, **431**, 53-57.

41. K. Yoshikawa, H. Kawasaki, W. Yoshida, T. Irie, K. Konishi, K. Nakano, T. Uto, D. Adachi, M. Kanematsu, H. Uzu and K. Yamamoto, Silicon Heterojunction Solar Cell with Interdigitated Back Contacts for a Photoconversion Efficiency over 26%, *Nat. Energy*, 2017, **2**, 17032.

42. A. Goetzberger and C. Hebling, Photovoltaic Materials, Past, Present, Future, *Sol. Energ. Mat. Sol. Cells*, 2000, **62**, 1-19.

43. J. Song, S. S. Li, C. H. Huang, O. D. Crisalle and T. J. Anderson, Device Modeling and Simulation of the Performance of $Cu(In_{1-X},Ga_x)Se_2$ Solar Cells, *Solid-State Electron.*, 2004, **48**, 73-79.

44. F. B. Dejene, The Structural and Material Properties of $CuInSe_2$ and $Cu(In,Ga)Se_2$ Prepared by Selenization of Stacks of Metal and Compound Precursors by Se Vapor for Solar Cell Applications, *Sol. Energ. Mat. Sol. Cells*, 2009, **93**, 577-582.

45. R. A. Mickelsen and W. S. Chen, High Photocurrent Polycrystalline Thin-Film $CdS/CuInSe_2$ Solar Cell, *Appl. Phys. Lett.*, 1980, **36**, 371-373.

46. P. Jackson, R. Wuerz, D. Hariskos, E. Lotter, W. Witte and M. Powalla, Effects of Heavy Alkali Elements in $Cu(In,Ga)Se_2$ Solar Cells with Efficiencies up to 22.6%, *Phys. Status Solidi Rapid Res. Lett.*, 2016, **10**, 583-586.

47. W. Li, Y. Sun, W. Liu and L. Zhou, Fabrication of $Cu(In,Ga)Se_2$ Thin Films Solar Cell by Selenization Process with Se Vapor, *Solar Energy*, 2006, **80**, 191-195.

48. J. A. Frantz, R. Y. Bekele, V. Q. Nguyen, J. S. Sanghera, A. Bruce, S. V. Frolov, M. Cyrus and I. D. Aggarwal, Cu(In,Ga)Se_2 Thin Films and Devices Sputtered from a Single Target without Additional Selenization, *Thin Solid Films*, 2011, **519**, 7763-7765.

49. B. J. Stanbery, S. Kincal, S. Kim, C. H. Chang, S. P. Ahrenkiel, G. Lippold, H. Neumann, T. J. Anderson and O. D. Crisalle, Epitaxial Growth and Characterization of $CuInSe_2$ Crystallographic Polytypes, *J. Appl. Phys.*, 2002, **91**, 3598-3604.

50. M. Kaelin, D. Rudmann, F. Kurdesau, T. Meyer, H. Zogg and A. N. Tiwari, CIS and CIGS Layers from Selenized Nanoparticle Precursors, *Thin Solid Films*, 2003, **431–432**, 58-62.

51. E. Lee, J. W. Cho, J. Kim, J. Yun, J. H. Kim and B. K. Min, Synthesis of CIGS Powders: Transition from Binary to Quaternary Crystalline Structure, *J. Alloy. Compd.*, 2010, **506**, 969-972.

52. Q. Guo, S. J. Kim, M. Kar, W. N. Shafarman, R. W. Birkmire, E. A. Stach, R. Agrawal and H. W. Hillhouse, Development of $CuInSe_2$ Nanocrystal and Nanoring Inks for Low-Cost Solar Cells, *Nano Lett.*, 2008, **8**, 2982-2987.

53. A. Cho, S. Ahn, J. H. Yun, J. Gwak, H. Song and K. Yoon, A Hybrid Ink of Binary Copper Sulfide Nanoparticles and Indium Precursor Solution for a Dense $CuInSe_2$ Absorber Thin Film and Its Photovoltaic Performance, *J. Mater. Chem.*, 2012, **22**, 17893-17899.

54. B. Li, Y. Xie, J. Huang and Y. Qian, Synthesis by a Solvothermal Route and Characterization of $CuInSe_2$ Nanowhiskers and Nanoparticles, *Adv. Mater.*, 1999, **11**, 1456-1459.

55. A. Cho, S. Ahn, J. H. Yun, Y. J. Eo, H. Song and K. Yoon, Carbon Layer Reduction Via a Hybrid Ink of Binary Nanoparticles in Non-Vacuum-Processed $CuInSe_2$ Thin Films, *Sol. Energ. Mat. Sol. Cells*, 2013, **110**, 126-132.

56. G. Hodes, T. Engelhard, D. Cahen, L. L. Kazmerski and C. R. Herrington, Electroplated $CuInS_2$ and $CuInSe_2$ Layers: Preparation and Physical and Photovoltaic Characterization, *Thin Solid Films*, 1985, **128**, 93-106.

57. R. N. Bhattacharya, Solution Growth and Electrodeposited $CuInSe_2$ thin Films, *J. Electrochem. Soc.*, 1983, **130**, 2040-2042.

58. D. B. Mitzi, M. Yuan, W. Liu, A. J. Kellock, S. J. Chey, L. Gignac and A. G. Schrott, Hydrazine-Based Deposition Route for Device-Quality CIGS Films, *Thin Solid Films*, 2009, **517**, 2158-2162.

59. J. H. Scofield, A. Duda, D. Albin, B. L. Ballard and P. K. Predecki, Sputtered Molybdenum Bilayer Back Contact for Copper Indium Diselenide-Based Polycrystalline Thin-Film Solar Cells, *Thin Solid Films*, 1995, **260**, 26-31.

60. T. Nakada, K. Furumi and A. Kunioka, High-Efficiency Cadmium-Free $Cu(In,Ga)Se_2$ Thin-Film Solar Cells with Chemically Deposited Zns Buffer Layers, *IEEE Trans. Electron Dev.*, 1999, **46**, 2093-2097.

61. S. Y. Han, D. H. Lee, S. O. Ryu and C. H. Chang, ZnS Thin Films Deposited by a Spin Successive Ionic Layer Adsorption and Reaction Process, *Electrochem. Solid State Lett.*, 2010, **13**, D61-D64.

62. M. Gloeckler, A. L. Fahrenbruch and J. R. Sites, Numerical Modeling of CIGS and CdTe Solar Cells: Setting the Baseline, *Proceedings of the 3rd World Conference on Photovoltaic Energy Conversion, 2003*, 2003.

63. G. Carr, Sunny Uplands, *The Economist*, 2012, Nov 21.

64. C. Martin, Cheaper Than China Again, First Solar Vindicates U.S. Investment, *Bloomberg*, 2016, April 14.

65. A. Goodrich, T. James and M. Woodhouse, *Solar PV Manufacturing Cost Analysis: U.S. Competitiveness in a Global Industry*, NREL, 2011.

66. *Mineral Commodity Summaries 2017*, U.S. Geological Survey, 2017.

67. H. Katagiri, K. Saitoh, T. Washio, H. Shinohara, T. Kurumadani and S. Miyajima, Development of Thin Film Solar Cell Based on Cu_2ZnSnS_4 Thin Films, *Sol. Energ. Mat. Sol. Cells*, 2001, **65**, 141-148.

68. T. K. Todorov, K. B. Reuter and D. B. Mitzi, High-Efficiency Solar Cell with Earth-Abundant Liquid-Processed Absorber, *Adv. Mater.*, 2010, **22**, E156-E159.

69. S. Wagner and P. M. Bridenbaugh, Multicomponent Tetrahedral Compounds for Solar Cells, *J. Cryst. Growth*, 1977, **39**, 151-159.

70. T. M. Friedlmeier, N. Wieser, T. Walter, H. Dittrich and H. W. Schock, in *Proceedings of the 14th European Photovoltaic Solar Energy Conference*, WIP, Frankfurt, 1997.

71. H. Katagiri, K. Jimbo, W. S. Maw, K. Oishi, M. Yamazaki, H. Araki and A. Takeuchi, Development of CZTS-Based Thin Film Solar Cells, *Thin Solid Films*, 2009, **517**, 2455-2460.

72. W. Wang, M. T. Winkler, O. Gunawan, T. Gokmen, T. K. Todorov, Y. Zhu and D. B. Mitzi, Device Characteristics of CZTSSe Thin-Film Solar Cells with 12.6% Efficiency, *Adv. Energy Mater.*, 2014, **4**, 1301465.

73. R. Lechner, S. Jost, J. Palm, M. Gowtham, F. Sorin, B. Louis, H. Yoo, R. A. Wibowo and R. Hock, $Cu_2ZnSn(S,Se)_4$ Solar Cells Processed by Rapid Thermal Processing of Stacked Elemental Layer Precursors, *Thin Solid Films*, 2013, **535**, 5-9.

74. J. He, L. Sun, K. Zhang, W. Wang, J. Jiang, Y. Chen, P. Yang and J. Chu, Effect of Post-Sulfurization on the Composition, Structure and Optical Properties of Cu_2ZnSnS_4 Thin Films Deposited by Sputtering from a Single Quaternary Target, *Appl. Surf. Sci.*, 2013, **264**, 133-138.

75. Q. Guo, G. M. Ford, W.-C. Yang, B. C. Walker, E. A. Stach, H. W. Hillhouse and R. Agrawal, Fabrication of 7.2% Efficient CZTSSe Solar Cells Using CZTS Nanocrystals, *J. Am. Chem. Soc.*, 2010, **132**, 17384-17386.

76. K.-J. Kim, C. Pan, S. Bansal, R. Malhotra, D.-H. Kim and C.-H. Chang, Scalably Synthesized Environmentally Benign, Aqueous-Based Binary Nanoparticle Inks for $Cu_2ZnSn(S,Se)_4$ Photovoltaic Cells Achieving over 9% Efficiency, *Sustainable Energy & Fuels*, 2017, **1**, 267-274.

77. J. J. Scragg, P. J. Dale, L. M. Peter, G. Zoppi and I. Forbes, New Routes to Sustainable Photovoltaics: Evaluation of Cu_2ZnSnS_4 as an Alternative Absorber Material, *Phys. Stat. Sol. (b)*, 2008, **245**, 1772-1778.

78. R. Schurr, A. Hölzing, S. Jost, R. Hock, T. Voβ, J. Schulze, A. Kirbs, A. Ennaoui, M. Lux-Steiner, A. Weber, I. Kötschau and H. W. Schock, The Crystallisation of Cu_2ZnSnS_4 Thin Film Solar Cell Absorbers from Co-Electroplated Cu–Zn–Sn Precursors, *Thin Solid Films*, 2009, **517**, 2465-2468.

79. E. G. Tulsky and J. R. Long, Dimensional Reduction: A Practical Formalism for Manipulating Solid Structures, *Chem. Mater.*, 2001, **13**, 1149-1166.

80. B. Eisenmann and J. Hansa, Crystal-Structure of Hexapotassium Hepta-selenodistannate, $K_6Sn_2Se_7$, *Zeitschrift Fur Kristallographie*, 1993, **203**, 303-304.

81. K. O. Klepp, Preparation and Crystal-Structure of $K_2Sn_2S_5$ and $K_2Sn_2Se_5$, *Zeitschrift Fur Naturforschung Section B-a Journal of Chemical Sciences*, 1992, **47**, 197-200.

82. T. W. Scharf and S. V. Prasad, Solid Lubricants: A Review, *J. Mater. Sci.*, 2013, **48**, 511-531.

83. K. S. Novoselov, A. K. Geim, S. V. Morozov, D. Jiang, Y. Zhang, S. V. Dubonos, I. V. Grigorieva and A. A. Firsov, Electric Field Effect in Atomically Thin Carbon Films, *Science*, 2004, **306**, 666-669.

84. A. Castellanos-Gomez, M. Barkelid, A. M. Goossens, V. E. Calado, H. S. J. van der Zant and G. A. Steele, Laser-Thinning of MoS_2: On Demand Generation of a Single-Layer Semiconductor, *Nano Lett.*, 2012, **12**, 3187-3192.

85. K.-G. Zhou, N.-N. Mao, H.-X. Wang, Y. Peng and H.-L. Zhang, A Mixed-Solvent Strategy for Efficient Exfoliation of Inorganic Graphene Analogues, *Angew. Chem. Int. Ed.*, 2011, **50**, 10839-10842.

86. Z. Zeng, Z. Yin, X. Huang, H. Li, Q. He, G. Lu, F. Boey and H. Zhang, Single-Layer Semiconducting Nanosheets: High-Yield Preparation and Device Fabrication, *Angew. Chem. Int. Ed.*, 2011, **50**, 11093-11097.

87. G. Eda, H. Yamaguchi, D. Voiry, T. Fujita, M. Chen and M. Chhowalla, Photoluminescence from Chemically Exfoliated MoS_2, *Nano Lett.*, 2011, **11**, 5111-5116.

88. S. Helveg, J. V. Lauritsen, E. Laegsgaard, I. Stensgaard, J. K. Norskov, B. S. Clausen, H. Topsoe and F. Besenbacher, Atomic-Scale Structure of Single-Layer MoS_2 Nanoclusters, *Phys. Rev. Lett.*, 2000, **84**, 951-954.

89. J. V. Lauritsen, J. Kibsgaard, S. Helveg, H. Topsoe, B. S. Clausen, E. Laegsgaard and F. Besenbacher, Size-Dependent Structure of MoS_2 Nanocrystals, *Nat. Nanotechnol.*, 2007, **2**, 53-58.

90. J.-W. Seo, Y.-W. Jun, S.-W. Park, H. Nah, T. Moon, B. Park, J.-G. Kim, Y. J. Kim and J. Cheon, Two-Dimensional Nanosheet Crystals, *Angew. Chem. Int. Ed.*, 2007, **46**, 8828-8831.

91. S. Balendhran, J. Z. Ou, M. Bhaskaran, S. Sriram, S. Ippolito, Z. Vasic, E. Kats, S. Bhargava, S. Zhuiykov and K. Kalantar-zadeh, Atomically Thin Layers of MoS_2 Via a Two Step Thermal Evaporation-Exfoliation Method, *Nanoscale*, 2012, **4**, 461-466.

92. Y.-H. Lee, X.-Q. Zhang, W. Zhang, M.-T. Chang, C.-T. Lin, K.-D. Chang, Y.-C. Yu, J. T.-W. Wang, C.-S. Chang, L.-J. Li and T.-W. Lin, Synthesis of Large-Area MoS_2 Atomic Layers with Chemical Vapor Deposition, *Adv. Mater.*, 2012, **24**, 2320-2325.

93. Y. Zhan, Z. Liu, S. Najmaei, P. M. Ajayan and J. Lou, Large-Area Vapor-Phase Growth and Characterization of MoS_2 Atomic Layers on a SiO_2 Substrate, *Small*, 2012, **8**, 966-971.

94. K.-K. Liu, W. Zhang, Y.-H. Lee, Y.-C. Lin, M.-T. Chang, C. Su, C.-S. Chang, H. Li, Y. Shi, H. Zhang, C.-S. Lai and L.-J. Li, Growth of Large-Area and Highly Crystalline MoS_2 Thin Layers on Insulating Substrates, *Nano Lett.*, 2012, **12**, 1538-1544.

95. A. M. Seayad and D. M. Antonelli, Recent Advances in Hydrogen Storage in Metal-Containing Inorganic Nanostructures and Related Materials, *Adv. Mater.*, 2004, **16**, 765-777.

96. J. Putz and M. A. Aegerter, Spin Deposition of MoS_x Thin Films, *Thin Solid Films*, 1999, **351**, 119-124.

97. J. N. Coleman, M. Lotya, A. O'Neill, S. D. Bergin, P. J. King, U. Khan, K. Young, A. Gaucher, S. De, R. J. Smith, I. V. Shvets, S. K. Arora, G. Stanton, H.-Y. Kim, K. Lee, G. T. Kim, G. S. Duesberg, T. Hallam, J. J. Boland, J. J. Wang, J. F. Donegan, J. C. Grunlan, G. Moriarty, A. Shmeliov, R. J. Nicholls, J. M. Perkins, E. M. Grieveson, K. Theuwissen, D. W. McComb, P. D. Nellist and V. Nicolosi, Two-Dimensional Nanosheets Produced by Liquid Exfoliation of Layered Materials, *Science*, 2011, **331**, 568-571.

98. D. B. Mitzi, Solution Processing of Chalcogenide Semiconductors Via Dimensional Reduction, *Adv. Mater.*, 2009, **21**, 3141-3158.

99. D. B. Mitzi, L. L. Kosbar, C. E. Murray, M. Copel and A. Afzali, High-Mobility Ultrathin Semiconducting Films Prepared by Spin Coating, *Nature*, 2004, **428**, 299-303.

100. P. Watts and C. Wiles, Recent Advances in Synthetic Micro Reaction Technology, *Chem. Commun.*, 2007, DOI: 10.1039/B609428G, 443-467.

101. in *CRC Handbook of Chemistry and Physics*, ed. W. M. Haynes, CRC Press/Taylor & Francis, Boca Raton, FL, 97th Edition (Internet Version 2017) edn., 2017.

102. M. H. Matus, A. J. Arduengo and D. A. Dixon, The Heats of Formation of Diazene, Hydrazine, $N_2H_3^+$, $N_2H_5^+$, N_2H, and N_2H_3 and the Methyl Derivatives CH_3NNH, CH_3NNCH_3, and $CH_3HNNHCH_3$, *J. Phys. Chem. A*, 2006, **110**, 10116-10121.

103. H. W. Wang, P. Skeldon and G. E. Thompson, XPS Studies of MoS_2 Formation from Ammonium Tetrathiomolybdate Solutions, *Surf. Coat. Technol.*, 1997, **91**, 200-207.

104. Y. J. Yi, C. T. Williams, M. Glascock, G. Xiong, J. Lauterbach and C. H. Liang, Transformation of Mo and W Thiosalts into Unsupported Sulfide Catalysts: A Temperature Dependent in-situ Spectroscopic Investigation, *Mater. Res. Bull.*, 2014, **56**, 54-64.

105. W. Wang, S. Y. Han, S. J. Sung, D. H. Kim and C. H. Chang, 8.01% $CuInGaSe_2$ Solar Cells Fabricated by Air-Stable Low-Cost Inks, *Phys. Chem. Chem. Phys.*, 2012, **14**, 11154-11159.

106. Z. Fang, *Iron Chalcogenide-Based Thin Films Fabricated by Inkjet Printing*, Thesis for Master of Science (M.S.) in Chemical Engineering, Oregon State University, 2016.

107. P. Gaucher, S. P. Faure and P. Barboux, Ferroelectric Thin Film Research in France, *Integrated Ferroelectrics*, 1992, **1**, 353-362.

108. M. Pang and H. C. Zeng, Highly Ordered Self-Assemblies of Submicrometer Cu_2O Spheres and Their Hollow Chalcogenide Derivatives, *Langmuir*, 2010, **26**, 5963-5970.

109. R. C. Agarwala and V. Agarwala, Electroless Alloy/Composite Coatings: A Review, *Sadhana-Acad. Proc. Eng. Sci.*, 2003, **28**, 475-493.

110. D. B. Mitzi, M. Yuan, W. Liu, A. J. Kellock, S. J. Chey, V. Deline and A. G. Schrott, A High-Efficiency Solution-Deposited Thin-Film Photovoltaic Device, *Adv. Mater.*, 2008, **20**, 3657-3662.

111. D. H. Webber and R. L. Brutchey, Alkahest for V_2VI_3 Chalcogenides: Dissolution of Nine Bulk Semiconductors in a Diamine-Dithiol Solvent Mixture, *J. Am. Chem. Soc.*, 2013, **135**, 15722-15725.

112. R. Zhang, S. Cho, D. G. Lim, X. Hu, E. A. Stach, C. A. Handwerker and R. Agrawal, Metal-Metal Chalcogenide Molecular Precursors to Binary, Ternary, and Quaternary Metal Chalcogenide Thin Films for Electronic Devices, *Chem. Commun.*, 2016, **52**, 5007-5010.